SPATIAL DISTRIBUTION OF THERMAL RADIATION AT MICROWAVE FREQUENCIES

Thesis by

Nick George

In Partial Fulfillment of the Requirements
For the Degree of
Doctor of Philosophy

California Institute of Technology
Pasadena, California

1959

ACKNOWLEDGEMENT

The author wishes to express his indebtedness to his advisor, Professor C. H. Papas, for his helpful suggestions, his stimulating criticisms, and his encouragement throughout all phases of this investigation.

The author wishes to acknowledge the following helpful discussions of specific topics.

Mr. G. D. Boyd, on gaseous discharge tubes
Mr. H. H. Kuehl, on antenna theory
Professor R. V. Langmuir, on experimental techniques
Professor T. Lauritsen, on thermal radiation
Professor H. C. Martel, on noise theory
Dr. G. F. Smith, on experimental techniques
Dr. G. J. Stanley, on radiometer design
Mr. C. H. Wilcox, on noise theory.

Thanks are also extended to a colleague, H. Feiveson, who read the manuscript; Miss Benita von Klingspor, who prepared the figures; and Mrs. Ruth Stratton, who typed the text. The author is grateful for the generous financial support afforded him under the Howard Hughes Fellowship Program of the Hughes Aircraft Company.

ABSTRACT

Theoretical and experimental radiation patterns are given in spectral form for the thermal radiation from thin slots or heated wires having dimensions of the order of the comparison wavelength. Maxwell's equations and noise theory form the basis of the analyses in which three independent methods are used to predict a spatial distribution which exhibits interference minima and maxima. In the first, the wave equation is solved for a noise-excited transmission line which is suddenly short- and open-circuited at alternate ends. By a study of the trapped noise currents, it is found that the radiation pattern has an interference structure which is smoothed as the loss is increased. Secondly, a formula is derived for the radiation pattern of a heated wire by a computation of its absorption in an isothermal enclosure and by an application of the principle of detailed balancing. Finally, the pattern of a long thin slot is computed directly using the Leontovich-Rytov distributed source generalization of Nyquist's noise formula.

Fraunhofer pattern measurements are taken for a thin slot excited by a gaseous discharge at $10{,}100 \pm 200^{\circ}$K. The pattern measuring apparatus is a Dicke radiometer having the following characteristics: frequency 9200 mc/s, bandwidth to the detector 16 mc/s, modulation frequency 1000 c/s, and residual noise level 0.3 rms$^{\circ}$K.

The theory and the experiment demonstrate an interference phenomenon even though the source excitation is spatially extended and uncorrelated in time and space. The patterns are not even approximately Lambertian, e.g., a thin slot of 9.5π radians length exhibits a pattern having nine relative maxima in 180° with the maximum emission at 63° from the normal.

TABLE OF CONTENTS

APPENDICES

I INTRODUCTION

The energy emitted by a heated body extends over an unbounded range of frequencies. The energy content per unit interval of frequency, the spectral intensity, decreases exponentially toward zero for frequencies well above Wien's frequency of maximum emission, and it decreases to a constant value, kT, for frequencies which are much less than Wien's frequency. For a body in thermal equilibrium at a temperature T, the spectral distribution of the emitted energy is given quantitatively by Planck's law. A matter which would seem to warrant comparable interest concerns the spatial distribution of the emitted energy. However, the spatial-distribution question has received much less attention than that of the spectral-distribution during the past one hundred or so years, due mainly to the fairly general applicability of a simple formula known as Lambert's law. In one form, Lambert's law states that the intensity of the emitted radiation from a blackbody surface is proportional to the solid angle subtended by the body at the point of observation. It is well known that Lambert's law is approximate, but from the literature one gains the impression that the approximation is due solely to the departure of the bulk properties of actual materials from the idealizations hypothesized for a blackbody surface. However, it is pointed out in a recent work of Rytov that geometric optics is used in deriving Lambert's law. Therefore, it is reasoned that a significant departure from this law may exist for radiation from bodies of dimensions which are comparable with a wavelength. The nature of this departure is fundamentally different from that treated heretofore in that the radiator shape and size become important in determining the relative spatial intensity. It is the purpose of this paper to study the spatial distribution of the radiant energy, with special emphasis on those cases for which the body dimensions are expected to exert a pronounced influence on this distribution.

A problem in heat radiation is a problem which requires the application of Maxwell's electromagnetic theory, except in instances where the conditions of the problem justify the approximate methods of geometric optics. In the problems of interest to us, the solution of Maxwell's equations is required. Since there is a vast literature on radiation problems for cases in which the radiator dimension and the wavelength are comparable, one might wonder, at first, whether or not any of these are useful in their entirety. The answer is found to be negative, and the essential reason lies in the marked difference between the source currents and voltages for the case of the heat problem and for that of the traditional electromagnetic radiation problem. In the former, the source is spatially distributed and essentially uncorrelated both in time and in position. In the latter, the source is usually concentrated and correlated. Thus, logically, the first step in the solution of the heat radiation problem is the determination of a quantitative source description in terms of the electromagnetic source parameters, such as the charge density and the current density. Finally, having obtained the source description, one must determine the appropriate solution of Maxwell's equations. The remaining paragraphs of this introduction survey the pertinent results in the literature and introduce the topics covered in this paper.

In general, the chaotic motion of the particles, e.g., conduction electrons in a metal, atoms in a gas, and particles in suspension, gives rise to thermal radiation or electrical noise. The early work in the theory of fluctuations was done by Einstein (1905), Langevin (1908), deHaas and Lorentz (1913), and Schottky (1918). For our purposes, however, the theoretical result by Nyquist (1) (1927) for the spectral distribution of the terminal noise voltage is the most useful starting point for a source description. Nyquist's results were experimentally confirmed by Johnson (2) (1927) who studied a heated wire and by Mumford (3) (1949) who studied the gaseous discharge. Nyquist solved the general problem using thermodynamic arguments, while Bell (1938) solved the problem for the special case of metallic conduction and Parzen and Goldstein (4) (1950) treated the case of the gaseous discharge.

While the distributed character of random noise was recognized from the time of the earliest work in the theory of fluctuations, it received only scant attention from before 1927 until 1952. This long period of comparative inactivity was due mainly to the lack of experimental impetus; for while the terminal manifestations of thermal noise became so frequent in practical applications that, as an example, the noise figure problem in radio engineering was reduced to a routine design procedure, no provocative experimental dilemma appeared to draw attention to the distributed character of random noise. This inactivity was disturbed by Dicke's microwave receiver (5) (1946), and thereafter, by the rapid emergence of the new science of radio-astronomy. Then, in 1952, Leontovich and Rytov (6) derived an expression for the distributed random electric field, i.e., the distributed noise source. Rytov generalized and applied the theory in a monograph (7) (1953). Levin and Rytov (8) (1955) derived an expression for the spatial distribution of the thermal radiation from a linear antenna. However, no accounts have been found of experimental verification of the Leontovich-Rytov formula for the thermal electric field (1959).

In this paper the treatment of the thermal radiator is divided into four parts. First, the theory is presented for the determination of the classical radiation pattern. The exceptions to Lambert's law are introduced in a natural way, by a method apparently first suggested by Drude. Then, an interesting computation is given which serves to explain a discrepancy observed by Spiller (9) in 1931 for the radiation from incandescent tungsten. For the example considered, the deviation from Lambert's law, arising from the non-blackbody nature of a metallic surface, is only a modest 15%.

The noise theory of Nyquist and Leontovich-Rytov, is presented in the second part. A simple derivation is given for the Leontovich-Rytov formula (Sec. 3.4). Then, from an analysis of the standing noise waves on a non-radiating, open-circuited transmission line, the inference is drawn that the thermal radiation pattern of a heated wire will exhibit pronounced maxima and minima, when its length and the wavelength are of the same order (Sec. 3.5).

In the third part a study is made of the level of the radiation from various noise sources. A comparative analysis is given for the radiation levels obtained from a gaseous discharge source and from a heated wire. It is shown that a measurement of the microwave radiation pattern from a gaseous discharge is practical; while for a heated wire it is not (Secs. 4.1 and 4.3). In the course of this study, an analysis is presented for the thermal radiation pattern of a heated wire which makes use of the principle of detailed balancing of radiation but which does not require the Leontovich-Rytov distributed source formulation (Sec. 4.1).

A comprehensive analysis of the thin slot is given in the fourth part. An expression is derived for the thermal radiation pattern in terms of an arbitrary source correlation function (Sec. 5.3). Then, three separate correlation functions are assumed, and their corresponding radiation pattern formulas are derived and plotted. The cases treated are the delta-correlated source, the exponentially-correlated source and the spatially-coherent source. Finally, experimental data are presented for the thermal radiation patterns of various thin slots. These data are compared with the theory and good agreement is obtained.

II CLASSICAL THERMAL RADIATION PATTERNS

2.1 Introduction

The term "classical thermal radiation pattern", as used here, denotes the spatial distribution of radiant energy from a given source that is obtained by analyses which are based on a combination of Planck's law and Lambert's law. Also included in this terminology are those distributions obtained using refinements of Lambert's law to include effects such as the variation of the emissivity with temperature, angle, etc. It is emphasized that the nomenclature (in particular the "classical") does not imply that this analytical technique is either outdated or incorrect, but rather it implies a restriction to the range of applicability of this particular formulation. Specifically, this formulation gives accurate results when the wavelength is very small in comparison to the source dimensions and the distance to the observer. It is not applicable, however, when the source dimensions and the wavelength are of the same order of magnitude. The reason for this limitation, as is described in detail below, is that Lambert's law, including refinements, is based on the principles of geometric optics which are clearly not valid when the wavelength and the source dimensions are comparable. A more general analysis can be formulated based mainly on a combination of Planck's law and Maxwell's equations. At least in principle, this formulation enables one to determine the exact thermal radiation pattern for a blackbody source of dimensions comparable with a wavelength. However, before turning to this analysis, it is worth while to present the fundamentals of the pattern determination for the classical thermal radiator.

2.2 Planck's Radiation Law (10)

In an isothermal enclosure at a temperature, T, the energy density in the frequency interval from f to f + df is denoted by ψ_f df and is given by Planck's formula as

$$\psi_f \, df = \frac{8\pi f^2}{c^3} \frac{hf}{e^{hf/kT} - 1} \, df \quad . \tag{2.1}$$

The average energy per degree of freedom, $\bar{\epsilon}$, is given by Eq. 2.2 below.

$$\bar{\epsilon} = \frac{hf}{e^{hf/kT} - 1} \quad . \tag{2.2}$$

2.3 Lambert's Cosine Law (10),(11),(12)

A simple consideration of an isothermal enclosure, based on the isotropy of the radiation stream and also based on geometric optics shows that the intensity of the radiation energy emitted by an infinitesimal planar blackbody surface for (arbitrary) frequency interval varies as the cosine of the angle between the normal to the surface and the direction of the emitted ray, i.e., Lambert's law.

From the above, it can be shown that the power incident in a frequency interval df, on a surface which subtends a solid angle $d\Omega$, at a distance R from the blackbody radiator, is given by $dP_{f\Omega}\, df\, d\Omega$ in Eq. 2.3.

$$dP_{f\Omega}\, df d\Omega = \frac{c}{4\pi} \psi_f \, df \, R^2 d\Omega' \, d\Omega \, . \tag{2.3}$$

The solid angles, $d\Omega$ and $d\Omega'$, are those subtended by the receiving area and the emitting area as measured at the emitter and receiver points respectively. Equations 2.1, 2.2, and 2.3 are combined to give the following form of $dP_{f\Omega}$,

$$dP_{f\Omega} df\, d\Omega = \frac{2f^2 df}{c^2}\, \bar{\epsilon}\, R^2 d\Omega d\Omega' \quad . \tag{2.4}$$

2.4 Radiation Patterns

The radiation from a non-blackbody surface departs from Eq. 2.4 above. Kirchhoff's law, equating the fractional emissivity to the fractional absorptivity at each frequency f, leads to the following generalization of Eq. 2.4.

$$dP_{f\Omega} df\, d\Omega = \frac{2f^2 df}{c^2}\, \alpha_f\, \bar{\epsilon}\, R^2 d\Omega d\Omega' \quad . \tag{2.5}$$

In the equation above, the absorptivity, α_f, is the selective fractional absorption when the body is in thermal equilibrium with its surroundings. In general, for a given material α_f is a function of the temperature, the frequency, and the angle of emission.

From Eq. 2.5, the classical thermal radiation pattern of an arbitrary source distribution can be calculated. The pattern for the frequency interval from f to f + df is simply the integral of $dP_{f\Omega} df$ over the source, i.e., $P_{f\Omega} df = \int_s dP_{f\Omega} df$, and the total radiation pattern includes, as well, an integration over frequency, i.e., $P_\Omega = \int_0^\infty \int_s dP_{f\Omega} df$. Two cases of particular interest are treated in the following paragraphs.

<u>2.4.1 Constant Absorptivity.</u> Let C describe an arbitrary simple closed perimeter in the x-y plane, the interior temperature is T, the

exterior temperature is zero. The wavelength, $\lambda = c/f$, is very small compared to a typical dimension, e.g., a diameter of the heated interior if the curve C is circular. Also, the absorptivity, α_f, is independent of angle. Equation 2.5 is applicable and the radiation pattern is given by integration of Eq. 2.5 over the heated interior. The result is

$$P_{f\Omega} df\, d\Omega = \frac{2f^2 df}{c^2} \alpha_f \bar{\epsilon} A d\Omega \cos \theta \tag{2.6}$$

in which A is the interior surface area and θ is the polar angle. Thus, in this idealized example, the radiation pattern follows Lambert's law (curve 1 in Fig. 2.1).

2.4.2 Variable Absorptivity. Let the interior surface A, again at a temperature T, be metallic. In this case the absorptivity is a function of the polar angle θ. This function, $\alpha_f(\theta)$, is obtained from a straightforward analysis of plane-wave reflection at an air-metal interface. The absorption coefficient when the incident electric field is in the plane of incidence, α_{f_1}, is given by Eq. 2.7, and for the case when the electric field is normal, by α_{f_2} in Eq. 2.8 (13),(14).

$$\alpha_{f_1} = \frac{4n \cos \theta}{(n^2 + k^2)\cos^2\theta + 2n \cos \theta + 1} \tag{2.7}$$

$$\alpha_{f_2} = \frac{4n \cos \theta}{(n^2 + k^2) + 2n \cos \theta + \cos^2\theta} \tag{2.8}$$

Equations 2.7 and 2.8 assume that $(n^2 + k^2) \gg 1$. θ is the angle of incidence, and n,k are the real and imaginary parts, respectively of the complex index of refraction, $n_c = [\mu(\epsilon - i\sigma/\omega)/\mu_o\epsilon_o]^{1/2}$. Separated into real and imaginary parts, this index, n_c, is given by 58.2 of

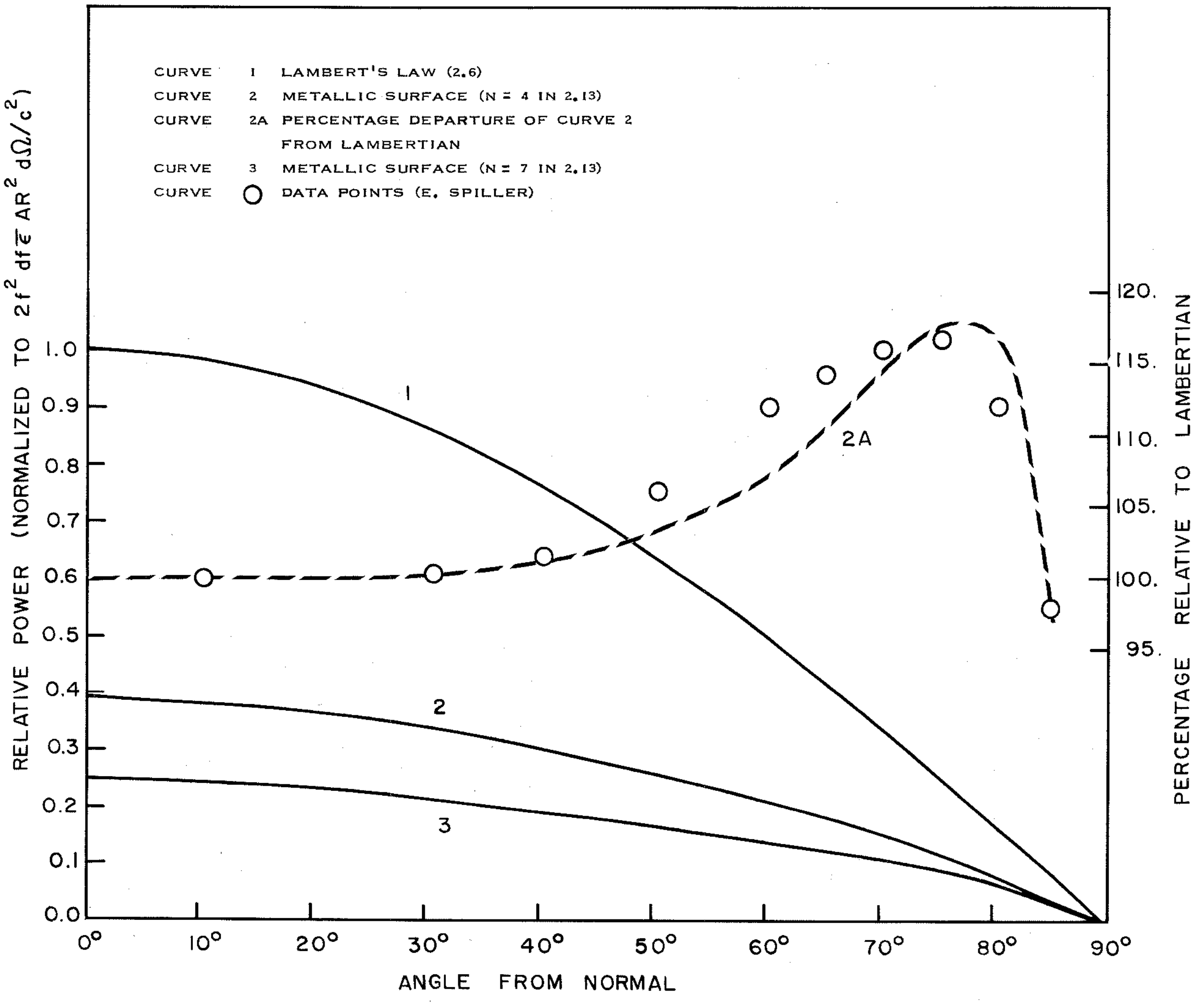

Fig. 2.1. Classical thermal radiation patterns

Dwight (15) as follows:

$$\begin{aligned} n_c &= n + jk \\ n &= \left\{ \frac{\mu\epsilon}{2\mu_o\epsilon_o} \left[\left(1 + \frac{\sigma^2}{\omega^2\epsilon^2}\right)^{1/2} + 1 \right] \right\}^{1/2} \\ k &= -\left\{ \frac{\mu\epsilon}{2\mu_o\epsilon_o} \left[\left(1 + \frac{\sigma^2}{\omega^2\epsilon^2}\right)^{1/2} - 1 \right] \right\}^{1/2} . \end{aligned} \qquad (2.9)$$

The absorption coefficient required in our computation is the one that is applicable when blackbody radiation is incident, i.e., the absorption coefficient for randomly polarized radiation. This absorption coefficient, α_f, is the mean of α_{f_1} and α_{f_2}.

$$\alpha_f = \frac{1}{2} (\alpha_{f_1} + \alpha_{f_2}) \qquad (2.10)$$

The above formulation for the absorption coefficient, apparently first suggested by Drude, is accurate to within a few percent for wavelengths longer than $2\text{x}10^{-6}$ m. However, even at this wavelength, the conductivity of metals is sufficiently high so that $\sigma/\omega\epsilon \gg 1$, and therefore Eq. 2.9 can be rewritten approximately as follows:

$$\begin{aligned} n &\doteq \left(\frac{\sigma}{2\omega\epsilon}\right)^{1/2} \\ k &\doteq \left(\frac{\sigma}{2\omega\epsilon}\right)^{1/2} . \end{aligned} \qquad (2.11)$$

Now, combining Eqs. 2.7, 2.8, 2.10, and 2.11, one obtains the following relatively simple formula for the absorption coefficient of a metallic surface when randomly polarized radiation is incident

$$\alpha_f = \frac{2n \cos \Theta}{2(n \cos \Theta)^2 + 2n \cos \Theta + 1} + \frac{2n \cos \Theta}{(\cos \Theta)^2 + 2n \cos \Theta + 2n^2} . \qquad (2.12)$$

Substitution of Eq. 2.12 into Eq. 2.5 gives the following result for the classical radiation pattern of the planar metallic surface.

$$P_{f\Omega} = \frac{2f^2}{c^2} \bar{\epsilon} AR^2 \left\{ \frac{2n \cos^2\theta}{2(n \cos \theta)^2 + 2n \cos \theta + 1} + \frac{2n \cos^2\theta}{(\cos \theta)^2 + 2n \cos \theta + 2n^2} \right\} . \tag{2.13}$$

Equation 2.13 is plotted for $n = 4$ and for $n = 7$ in Fig. 2.1. These radiation patterns differ from that of a blackbody source in two essential ways. First, the absolute power level is lower. This is evident by a comparison of curves 1, 2, and 3 which are drawn with a common normalization factor. Secondly, the form of the curve departs from a cosine law. This is evident from curve 2A which is a normalization of curve 2 to a gray (Lambertian) source having the same intensity in the $\theta = 0$ direction.

The data points in Fig. 2.1 are taken from an experimental paper by E. Spiller (9). Spiller's experimental results were apparently definitive enough to settle a then-raging controversy over whether any departure from Lambert's law occurs for metallic radiators. The data are fit only approximately by Eq. 2.13 for the following reasons. First, for the wavelength used, $\lambda = 6560$ Å, there is some uncertainty as to the value of ϵ to use in Eq. 2.11; and secondly, there is some question about using the value of conductivity which is obtained at a much longer wavelength. With these factors in mind, the fit is surprisingly good.

2.4.3 Gaseous Discharge Pattern Experiment. While the central topic of this paper is the thermal radiation pattern at microwave frequencies, it is desirable for completeness to include an experimental pattern for the "very short" wavelength range using a gaseous discharge source and essentially the same experimental arrangement which is used for the microwave measurements (Fig. 5.12P). A description of this optical experiment follows (see inset in Fig. 2.2). A commercially available 15w fluorescent source, containing 2 mm. of argon and 6 to 10 μ of mercury gas and having an effective microwave noise temperature of 11,400°K at 30°C (3), illuminates a sensitive cadmium-sulphide photocell, which is placed in the Fraunhofer region at a range of 1.500 m. The radiating aperture is a thin slot 0.1419 m. by 4.0×10^{-3} m. in a large sheet of polished aluminum. This slot is approximately $5.5\pi \times 10^5$ by $1.5\pi \times 10^4$ radians at the peak of the spectral response of the photocell, i.e., at 5150 Å.* In order to correct for the slight departures from a square law response, the particular photocell used was first calibrated using a 3 m. optical bench. The experimental radiation pattern is shown in Fig. 2.2, normalized to a measured intensity of 1.60 lumens/m^2 at normal incidence. It is concluded that the radiation pattern at optical frequencies follows Lambert's law at least in an approximate fashion.

---

*This slot is 8.70π by 0.24π radians at 9200 mc/s. The corresponding microwave radiation pattern is shown in Fig. 5.15.

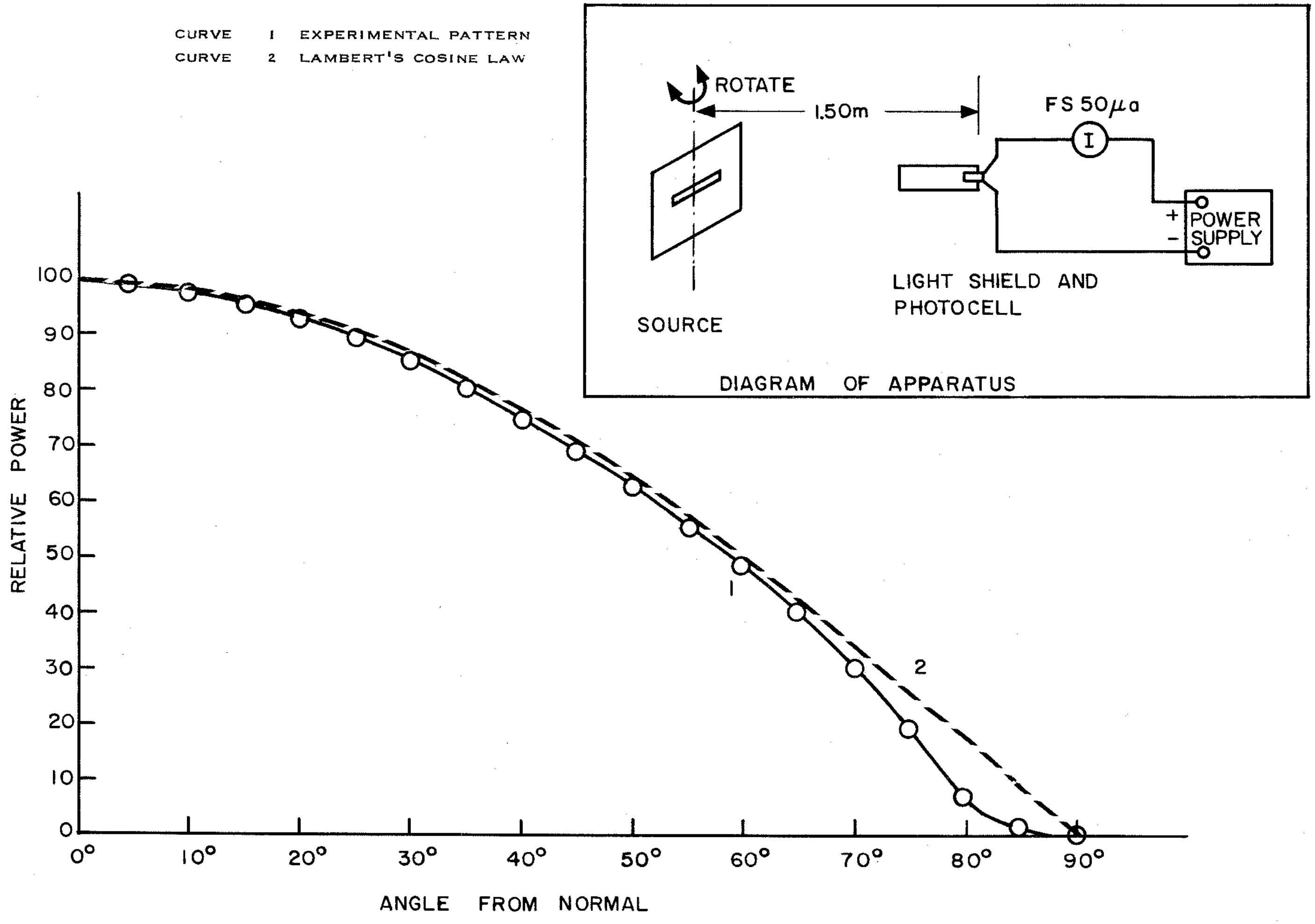

Fig. 2.2. Radiation pattern of gaseous discharge at optical frequencies

III NYQUIST-LEONTOVICH-RYTOV RANDOM NOISE THEORY

3.1 Fourier Integral Form of Maxwell's Equations

Maxwell's equations, including time dependence, are written

$$\begin{aligned} \nabla \times \underline{E}_1(\underline{r},t) &= -\frac{\partial \underline{B}_1(\underline{r},t)}{\partial t} \\ \nabla \times \frac{\underline{B}_1(\underline{r},t)}{\mu} &= \underline{j}(\underline{r},t) + \frac{\partial \underline{D}_1(\underline{r},t)}{\partial t} \quad . \end{aligned} \tag{3.1}$$

Taking the Fourier transform with respect to the time variable and neglecting "end" values gives

$$\begin{aligned} \nabla \times \underline{E}(\underline{r},\omega) &= -i\omega\, \underline{B}(\underline{r},\omega) \\ \nabla \times \frac{\underline{B}(\underline{r},\omega)}{\mu} &= \underline{j}(\underline{r},\omega) + i\omega\, \underline{D}(\underline{r},\omega) \end{aligned} \tag{3.2}$$

in which, as a typical example, $\underline{E}(\underline{r},\omega)$ is related to the electric field intensity $\underline{E}_1(\underline{r},t)$ as follows:

$$\begin{aligned} \underline{E}(\underline{r},\omega) &= \int_{-\infty}^{\infty} \underline{E}_1(\underline{r},t)e^{-i\omega t}dt \\ \underline{E}_1(\underline{r},t) &= \frac{1}{2\pi}\int_{-\infty}^{\infty} \underline{E}(\underline{r},\omega)e^{i\omega t}d\omega \quad . \end{aligned} \tag{3.3}$$

It is convenient throughout this paper to adopt the convention that $\underline{E}$, $\underline{B}$, $\underline{D}$, etc. denote the Fourier transforms of their corresponding field variables, and the usual tilde notation will not be employed. Direct time dependence will be indicated explicitly in order to avoid confusion, e.g., Eq. 3.1. This has the added feature of making many of the equations which arise in the solution of Maxwell's equations formally the same as those which occur under the assumption of harmonic time dependence (the $e^{i\omega t}$ factor must be suppressed). This follows directly from a comparison of Eqs. 3.2, rewritten below, to Eqs. 3.1 when they are rewritten for an $e^{i\omega t}$ time dependence.

$$\nabla \times \underline{E} = - i\omega \underline{B} \tag{3.4a}$$

$$\nabla \times \frac{\underline{B}}{\mu} = \underline{j} + i\omega \underline{D} \quad . \tag{3.4b}$$

3.2 Spectral Density and Correlation Function

The source field for radiation from a hot body is a random function of position and time. The radiation from such a body is most concisely expressed in terms of the power/area or the power/solid angle in a given direction. Although it is convenient to analyze this problem in terms of $\underline{E}$ and $\underline{B}$, these field vectors are sample functions of a stationary random process, and it is only their statistical characterizations, such as the rms value, spectral density, etc., for which there exist non-statistical functional forms. Certain of these forms and some of the standard relations between them, are summarized in this paragraph (16). Consider a stationary random process which is characterized by an ensemble of sample functions, $f_i(t)$. The autocorrelation function of this random process, $R(\tau)$, is defined as the value of the product $f_i(t)\, f_i^*(t-\tau)$ averaged over the ensemble, i.e.,

$$R(\tau) = \frac{1}{n} \sum_{i=1}^{n} f_i(t)\, f_i^*(t-\tau) \quad .$$

It is convenient to denote an ensemble average by the following bra-ket notation: $\langle\ \rangle$ or $\langle\ \rangle_f$. Then, the autocorrelation function is written

$$R(\tau) = \left\langle f(t)\ f^*(t-\tau)\right\rangle \quad . \tag{3.5}$$

The spectral density, $S(\omega)$, is defined as the Fourier transform of the autocorrelation function

$$S(\omega) = \int_{-\infty}^{\infty} R(\tau)\ e^{-i\omega\tau} d\tau \quad . \tag{3.6a}$$

Of course, taking the inverse transform returns the autocorrelation function

$$R(\tau) = \frac{1}{2\pi} \int_{-\infty}^{\infty} S(\omega)\ e^{i\omega\tau} d\omega \tag{3.6b}$$

and setting $\tau = 0$ gives the following useful expression relating the spectral intensity to the mean square value of the sample function.

$$\left\langle f(t)\ f^*(t)\right\rangle = \frac{1}{2\pi} \int_{-\infty}^{\infty} S(\omega)\ d\omega \tag{3.7}$$

The time-limited sample function, $f_T(t)$, is defined by

$$\begin{aligned} f_T(t) &= f(t) \qquad \text{for} \quad |t| \leq T \\ f_T(t) &= 0 \qquad\quad \text{for} \quad |t| > T \end{aligned} \tag{3.8}$$

and the corresponding Fourier transform becomes

$$F_T(\omega) = \int_{-\infty}^{\infty} f_T(t)\ e^{-i\omega t} dt$$

$$F_T(\omega) = \int_{-T}^{T} f(t)\ e^{-i\omega t} dt \quad .$$

Now, a useful result which relates the spectral density to the time-limited Fourier transform is quoted (16):

$$S(\omega) = \lim_{T \to \infty} \left\langle \frac{F_T(\omega)\ F_T^*(\omega)}{2T} \right\rangle_f \quad . \tag{3.9}$$

The results of the above paragraph are generalized for the two-dimensional case. Consider the sample function, $f(z,t)$, of a stationary random process. The time-limited Fourier transform, F_T, is given by

$$F_T \doteq \int_{-\infty}^{\infty} f_T(z,t) e^{-i\omega t} d\omega$$

$$F_T = \int_{-T}^{T} f(z,t) e^{-i\omega t} dt \quad . \tag{3.10}$$

The two-dimensional correlation function, $RR_f(\rho,\tau)$, is defined as the following ensemble average

$$RR_f(\rho,\tau) = \left\langle f(z,t)\ f^*(z-\rho,t-\tau) \right\rangle_f \quad . \tag{3.11}$$

The two-dimensional spectral density, $SS_f(\eta,\omega)$, is defined as follows

$$SS_f(\eta,\omega) = \int_{-\infty}^{\infty} \int_{-\infty}^{\infty} RR_f(\rho,\tau) e^{-i\eta\rho - i\omega\tau} d\rho\ d\tau \quad . \tag{3.12}$$

Mixed correlation-spectral density functions can also occur, e.g., $RS_f(\rho,\omega)$ given by the following one-dimensional Fourier transform of RR_f

$$RS_f(\rho,\omega) = \int_{-\infty}^{\infty} RR_f(\rho,\tau) e^{-i\omega\tau} d\tau \quad . \tag{3.13}$$

The two-dimensional analogue of Eq. 3.9 is derived below. The ensemble average, $\left\langle F_{TL}(\eta,\omega)\ F^*_{TL}(\eta,\omega)\right\rangle_f$, can be written in terms of f(z,t) as follows

$$\left\langle F_{TL}(\eta,\omega)F^*_{TL}(\eta,\omega)\right\rangle_f = \left\langle \int_{-T}^{T}\int_{-T}^{T}\int_{-L}^{L}\int_{-L}^{L} f(z_1,t_1)f^*(z_2,t_2) \right.$$

$$\left. \times\ e^{-i\eta(z_1-z_2)-i\omega(t_1-t_2)}\, dz_1dz_2dt_1dt_2 \right\rangle_f . \tag{3.14}$$

The ensemble average and the integration are commutative; and the exponential term can be factored out of the ensemble-averaging brackets; hence Eq. 3.14 is rewritten

$$\left\langle F_{TL}(\eta,\omega)F^*_{TL}(\eta,\omega)\right\rangle_f = \int_{-T}^{T}\int_{-T}^{T}\int_{-L}^{L}\int_{-L}^{L} \left\langle f(z_1,t_1)f^*(z_2,t_2)\right\rangle_f$$

$$\times\ e^{-i\eta(z_1-z_2)-i\omega(t_1-t_2)}\, dz_1dz_2dt_1dt_2 . \tag{3.15}$$

Making a change of variables from (z_1,z_2,t_1,t_2) to (z_1,ρ,t_1,τ) where ρ and τ are defined by

$$\rho = z_1 - z_2$$

$$\tau = t_1 - t_2$$

and substituting Eq. 3.11 into Eq. 3.15, it follows that

$$\left\langle F_{TL}F^*_{TL}\right\rangle_f = \iint d\tau\ dt_1 \left\{ \int_{-2L}^{0} d\rho\ \phi(\rho,\tau) \int_{-L}^{L+\rho} dx_1 + \int_{0}^{2L} d\rho\ \phi(\rho,\tau) \int_{-L+\rho}^{L} dx_1 \right\} \tag{3.16}$$

in which $\phi(\rho,\tau)$ is given by

$$\phi(\rho,\tau) = RR_f(\rho,\tau)e^{-i\eta\rho-i\omega\tau} \quad . \tag{3.17}$$

Integrating Eq. 3.16 with respect to the variable x_1 and writing in the limits on the τ, t_1 integration lead to Eq. 3.18

$$\left\langle F_{TL}F^*_{TL}\right\rangle_f = 2L\int_{-2L}^{2L} d\rho\left(1 - \frac{|\rho|}{2L}\right)\left\{\int_{-2T}^{0} d\tau\ \phi(\rho,\tau)\int_{-T}^{T+\tau} dt_1 + \int_{0}^{2T} d\tau\phi(\rho,\tau)\int_{-T}^{T+\tau} dt_1\right\} \tag{3.18}$$

Integrating again, with respect to t_1, and rearranging slightly give the following expression.

$$\left\langle \frac{F_{TL}F^*_{TL}}{(2L)(2T)}\right\rangle_f = \int_{-2L}^{2L}\int_{-2T}^{2T} \left(1 - \frac{|\rho|}{2L}\right)\left(1 - \frac{|\tau|}{2T}\right)RR_f(\rho,\tau)e^{-i\eta\rho-i\omega\tau} d\tau d\rho \ . \tag{3.19}$$

In the limit as L,T → ∞, Eq. 3.19 becomes

$$\lim_{T,L \to \infty} \left\langle \frac{F_{TL}\ F^*_{TL}}{(2L)(2T)}\right\rangle_f = \int_{-\infty}^{\infty}\int_{-\infty}^{\infty} RR_f(\rho,\tau)e^{-i\eta\rho-i\omega\tau} d\tau d\rho$$

and substitution of Eq. 3.12 gives the final form

$$SS_f\ (\eta,\omega) = \lim_{T,L\to \infty} \left\langle \frac{F_{TL}\ F^*_{TL}}{(2L)(2T)}\right\rangle_f \quad . \tag{3.20}$$

Since in the noise problem to be analyzed, the source terms have a finite non-zero rms value, i.e., the source can supply finite energy in any finite interval, then

$$0 < \frac{1}{2T}\int_{-T}^{T} f(t)\ f^*(t)\ dt < \infty \quad .$$

Hence, $f(t)$ is not usually a function of integrable square; Plancherel's theorem is not applicable; and thus, there is no assurance that the Fourier transform, $F(\omega)$, exists. In a strict notation then, the various source and field terms which arise later should be dimension limited, e.g., as the $f_T(z)$ in Eq. 3.8; and the Fourier transforms in Eqs. 3.2, 3.3, and 3.4 should be given "T" subscripts as the F_T in Eq. 3.10. From our point of view, however, this would unduly complicate the notation since our only interest is to compute spectral densities from Eq. 3.20 and subtleties of existence and convergence, in which case the notation may be useful, do not arise.

3.3 Nyquist's Formula for Random EMF

In 1927, Johnson (2) performed the first quantitative experiments relating the statistical fluctuations of electrons in a conductive medium to the random variation of potential between two electrodes in the medium, and in that same year Nyquist (1) derived a formula for this EMF. The derivation, based on thermodynamics and statistical mechanics, is briefly outlined below.

Consider a system composed of two resistors, R, connected by a lossless non-radiative transmission line of length ℓ and of characteristic impedance R, with the entire system in thermodynamic equilibrium at a temperature T . The amount of power which each resistor can deliver under these matched conditions is deduced by the following thought experiment. The line is suddenly short-circuited at both ends; thereafter the energy trapped on the lines is confined to modes for which the terminal voltage is zero, i.e., to eigenfrequencies, f_n, given by

$$f_n = \frac{nc}{2\ell} \qquad n = 1,2,3,\cdots \ . \tag{3.21}$$

Now, by Planck's modification of the classical law of equipartition, the average total energy per degree of freedom, denoted by $\overline{\epsilon}$, is given by

$$\overline{\epsilon} = \frac{hf}{e^{hf/kT} - 1} \tag{3.22a}$$

or if $hf/kT \ll 1$, then $\overline{\epsilon}$ is approximately given by

$$\overline{\epsilon} \doteq kT \ . \tag{3.22b}$$

Hence, in the frequency interval f_n to $f_n + \Delta f$, the total energy on the line, supplied equally by both resistors at a rate $P_f \Delta f$ for a period ℓ/c before shorting, is given by

$$2P_f \ \Delta f \frac{\ell}{c} = 2 \ \overline{\epsilon} \ \Delta f \frac{\ell}{c} \ \cdot \tag{3.23}$$

Thus, by Eq. 3.23, Nyquist's well-known result for the spectral intensity of the available power is

$$P_f = \overline{\epsilon} \ . \tag{3.24}$$

The total power is given by the integral of P_f over the real frequencies from 0 to ∞, i.e., $\int_0^\infty P_f \, df$. P_f is called a one-sided spectral density to distinguish it from the spectral density S_p which is defined as the even continuation of $P_f/2$ into the negative frequencies. Then, the total power is given by $\int_{-\infty}^{\infty} S_p \, df$, and this latter density is of the form implicit in Eq. 3.7. Now, S_p can be expressed in terms of the ensemble average of the terminal noise voltage as follows

$$\int_{-\infty}^{\infty} S_p \, df = \frac{\langle v(t) \; v^*(t) \rangle}{4R}$$

$$\int_{-\infty}^{\infty} S_p \, df = \frac{1}{4R} \int_{-\infty}^{\infty} S_v \, df \quad . \qquad (3.25)$$

Thus, by Eqs. 3.24 and 3.25, the spectral intensity of the open-circuited voltage across the resistor terminals is given by

$$S_v(\omega) = 2\bar{\epsilon} R \qquad (3.26a)$$

and the corresponding autocorrelation function is

$$R_v(\tau) = 2\bar{\epsilon} R \, \delta(\tau) \quad . \qquad (3.26b)$$

3.4 Leontovich-Rytov Random Electric Field

Early research workers in the field of thermal electric noise clearly recognized the distributed nature of the source of this noise, i.e., distributed as it arises from the chaotic motions of free electrons within a conductor, but due to the then singular application of noise theory to lumped circuits, the major interest centered on the formulation of expressions for total or terminal noise voltages and currents. It remained for Leontovich and Rytov to derive an expression for the distributed random electric field (6). Their work is further generalized in a monograph by Rytov in which Maxwell's equations for material media are augmented by the introduction of noise source field terms, both electric and magnetic (7). In a later report, this theory is interestingly outlined, together with selected applications to noise problems in a waveguide (17).

The formula for the thermal electric field in a conductive medium follows in a straightforward fashion from Nyquist's spectral intensity formula, Eq. 3.25*. Consider a thin cylindrical filament of cross-section dA and length ℓ in a medium of conductivity σ. Orient a cartesian coordinate system so that the axis of the filament is z-directed and the cross-section, dA, is in the x-y plane. The terminal voltage $V(x,y,t)$ is given by the following sum:

$$V(x,y,t) = \sum_{r=1}^{n} E_z(x,y,z_r,t)\, dz_r \tag{3.27}$$

in which the n subdivisions of ℓ, dz_r, are chosen small enough so that the electric field is correlated along this length, presumably some fraction of a mean free path. From Eq. 3.27, the mean square voltage, $\langle V(x,y,t)\, V^*(x,y,t)\rangle$ is expressed as follows:

$$\langle V(x,y,t)V^*(x,y,t)\rangle = \sum_{r=1}^{n} \sum_{s=1}^{n} \langle E_z(x,y,z_r,t)E_z^*(x,y,z_s,t)\rangle\, dz_r dz_s \, . \tag{3.28}$$

It is assumed that the electric field is uncorrelated for lengths in excess of the subdivision length, dz_r. Thus in the ensemble average, terms for which $r \neq s$ are zero and Eq. 3.28 reduces to Eq. 3.29.

$$\langle V(x,y,t)V^*(x,y,t)\rangle = \sum_{r=1}^{n} \langle E_z(x,y,z_r,t)E_z^*(x,y,z_r,t)\rangle\, dz_r dz_r \, . \tag{3.29}$$

The mean square value of the electric field is independent of z ;

---

*The derivation given here departs from that of the above-cited reference, but the underlying philosophy and the result are due to Leontovich and Rytov.

hence the right member of Eq. 3.29 can be simplified. Making this simplification, substituting for $\langle VV^* \rangle$ from Eq. 3.26, and rearranging slightly, one obtains Eq. 3.30

$$\left\langle E_z(x,y,z,t)\ E_z^*(x,y,z,t) \right\rangle = \left(\frac{2\overline{\epsilon}}{\sigma}\right) \frac{\delta(\tau = 0)}{dz\ dA} \quad . \tag{3.30}$$

With the aid of the Dirac-delta notation to incorporate the prior assumption that the electric field is uncorrelated for separations greater than (dx,dy,dz), Eq. 3.30 leads to the desired result

$$\left\langle E_z(x,y,z,t) E_z^*(x-\xi,y-\eta,z-\rho,t-\tau) \right\rangle = \left(\frac{2\overline{\epsilon}}{\sigma}\right) \delta(\xi)\delta(\eta)\delta(\rho)\delta(\tau)$$

$$RR_e(\xi,\eta,\rho,\tau) = \frac{2\overline{\epsilon}}{\sigma}\ \delta(\xi)\delta(\eta)\delta(\rho)\delta(\tau) \quad . \tag{3.31}$$

Reduction of Eq. 3.30 to the one-dimensional case, i.e., a line source, gives the following result for the distributed noise field

$$\left\langle E_z(z,t) E_z^*(z-\rho,t-\tau) \right\rangle = \frac{2\overline{\epsilon}}{\sigma_1}\ \delta(\rho)\delta(\tau)$$

$$RR_e(\rho,\tau) = \frac{2\overline{\epsilon}}{\sigma_1}\ \delta(\rho)\ \delta(\tau) \quad . \tag{3.32}$$

The factor σ_1 is the conductivity per unit length, σdA. This derivation for the distributed noise field is based on Nyquist's fundamental result and the assertion that the distributed source field is spatially completely uncorrelated. The resulting formula encompasses a far greater range of problems than does Nyquist's formula.

3.5 Induced Correlation in a Random Signal

In this section the primary purpose is to demonstrate analytically that some common radiator configurations can induce spatial correlation in their surface currents even though the source of these currents is a random generator. Toward this end, an equation is derived for the correlation function of the distributed current along a transmission line. Two cases are treated. In the first, the transmission line is terminated in its characteristic impedance. The noise currents generated by the terminal impedances travel along the transmission line and are completely absorbed at the alternate ends. It is of interest to have the correlation function for this case because the current distribution for the nonradiating matched transmission line serves as a first approximation to the current distribution for an important class of antennas, i.e., the Beverage or the wave antenna. In the second, the same transmission line is abruptly short-circuited at one end and open-circuited at the other. The noise energy which was traveling along the line is now trapped, and a standing wave is set up. In this case, the correlation function shows that the energy is confined to discrete eigenfrequencies and that the standing wave of noise current is fully correlated. The configuration in which the transmission line is short- and open-circuited at alternate ends is of interest because this current distribution serves as a first approximation for the current on another important type of antenna, i.e., the long thin wire.

3.5.1 Transmission Line Equations.

Consider a lossless nonradiating transmission line of characteristic impedance R and length ℓ.

This line is oriented along the z-axis with a terminal pair or port at $z = 0$ and at $z = \ell$. Assume that only the principal or TEM-mode propagates. Then, the potential difference between corresponding points of the line is uniquely defined and the telegrapher's equations are applicable. Briefly, for an inductance per unit length of L and a capacitance per unit length of C , the current and the voltage along the line, denoted by $I(z,t)$ and $V(z,t)$ respectively, are solutions of the following differential equations

$$\frac{\partial V(z,t)}{\partial z} = - L \frac{\partial I(z,t)}{\partial t} \tag{3.33}$$

$$\frac{\partial I(z,t)}{\partial z} = - C \frac{\partial V(z,t)}{\partial t} \quad . \tag{3.34}$$

Combining $\partial/\partial t$ of Eq. 3.33 and $\partial/\partial z$ of Eq. 3.34 leads to the wave equation in $I(z,t)$, Eq. 3.35; and combining $\partial/\partial t$ of Eq. 3.34 and $\partial/\partial z$ of Eq. 3.33 leads to Eq. 3.36.

$$\frac{\partial^2 I(z,t)}{\partial z^2} - \frac{1}{v^2} \frac{\partial^2 I(z,t)}{\partial t^2} = 0 \tag{3.35}$$

$$\frac{\partial^2 V(z,t)}{\partial z^2} - \frac{1}{v^2} \frac{\partial^2 V(z,t)}{\partial t^2} = 0 \quad . \tag{3.36}$$

The speed of propagation v is related to L,C by

$$v^2 = \frac{1}{LC} \tag{3.37}$$

and the characteristic impedance R is given by

$$R = \left(\frac{L}{C}\right)^{1/2} \quad . \tag{3.38}$$

3.5.2 Traveling Waves on a Matched Transmission Line. Let the transmission line of the preceding section be terminated in its characteristic impedance by resistors at a temperature T. These resistors at $z = 0$, $z = \ell$ generate noise voltages given by the functions $2V_1(t)$ and $2V_2(t)$, respectively, and by Eq. 3.26, the autocorrelation function of these sample functions is given by

$$R_{2v_1}(\tau) = R_{2v_2}(\tau) = 2\overline{\epsilon}R\ \delta(\tau) \quad . \tag{3.39}$$

Now, in this case, it can be shown that the solutions of Eqs. 3.35 and 3.36 are given by

$$V(z,t) = V_1(t - \frac{z}{v}) + V_2(t - \frac{\ell - z}{v}) \tag{3.40}$$

$$I(z,t) = \frac{1}{R}\left[V_1(t - \frac{z}{v}) - V_2(t - \frac{\ell - z}{v})\right] . \tag{3.41}$$

Substituting Eq. 3.40 into the defining equation, Eq. 3.11, and assuming that $V_1(t)$ and $V_2(t)$ are statistically independent, one can readily compute the two-dimensional correlation function. The result follows.

$$RR_v(\rho,\tau) = \left\langle V(z,t)\ V^*(z-\rho,t-\tau)\right\rangle_v$$

$$\begin{aligned} RR_v(\rho,\tau) &= \left\langle V_1(t - \frac{z}{v})V_1(t - \frac{z}{v} - \tau + \frac{\rho}{v}\right\rangle_{v_1} \\ &+ \left\langle V_2(t - \frac{\ell - z}{v})\ V_2(t - \frac{\ell - z}{v} - \tau - \frac{\rho}{v})\right\rangle_{v_2} \quad . \end{aligned} \tag{3.42}$$

The explicit values for these correlation functions are given by Eq. 3.39, and by substituting into Eq. 3.42, one obtains the following result

$$RR_v(\rho,\tau) = \frac{\overline{\epsilon}R}{2}\left[\delta(\tau - \frac{\rho}{v}) + \delta(\tau + \frac{\rho}{v})\right] \quad . \tag{3.43}$$

Thus, the mixed correlation-spectral density function for the voltage along the transmission line is given by Eq. 3.44 below.

$$RS_v(z_o-z_1,\omega) = \int_{-\infty}^{\infty} RR_v(z_o-z_1,\tau)e^{-i\omega\tau}d\tau$$

$$RS_v(z_o-z_1,\omega) = \overline{\epsilon}R \cos \beta(z_o-z_1) \quad . \tag{3.44}$$

By an analogous computation, the mixed correlation-spectral density function for the current along the transmission line is determined, and the result is

$$RS_i(z_o-z_1,\omega) = \frac{\overline{\epsilon}}{R} \cos \beta\ (z_o-z_1) \quad . \tag{3.45}$$

From Eq. 3.45, one concludes that the noise currents are correlated spatially. For a long-wire antenna having this correlation function of its current, it can easily be shown that this leads to a spatial distribution of the radiation which exhibits pronounced interference minima and maxima. This general type of computation is treated in Sec. 5.3.

3.5.3 Standing Waves on a Transmission Line. Let the transmission line of Sec. 3.5.2 suddenly be short-circuited at one end and open-circuited at the other. This leads to a mode confinement which is similar in its essential details to that which occurs in the model which Nyquist used to derive the formula for the random EMF (Sec. 3.3). Here, however, the short-circuit at one end is preferred in order to emphasize the close relationship between the currents on a transmission line and those on a long thin wire antenna, e.g., compare Figs.

4.1 and 4.2. In any event, the current, $I(z,t)$, and the voltage, $V(z,t)$, are determined as solutions of Eqs. 3.33 and 3.34 subject to the boundary conditions that for $t > 0$,

$$I(\ell,t) = 0 \qquad \text{(open-circuit)} \tag{3.46}$$

$$V(0,t) = 0 \qquad \text{(short-circuit)} \tag{3.47}$$

and subject to the initial conditions obtained from setting $t = 0$ in Eqs. 3.40 and 3.41, i.e.,

$$I_o = I(z,0) = \frac{1}{R}\left[V_1(-\frac{z}{v}) - V_2(\frac{z-\ell}{v})\right] \tag{3.48}$$

$$V_o = V(z,0) = V_1(-\frac{z}{v}) + V_2(\frac{z-\ell}{v}) \quad . \tag{3.49}$$

Solving Eq. 3.35 by the separation of variables and imposing the condition in Eq. 3.46, one obtains

$$I(z,t) = \sum_{n=0}^{\infty} (C_n \sin k_n vt + D_n \cos k_n vt) \cos k_n z$$

and likewise from Eqs. 3.36 and 3.47

$$V(z,t) = \sum_{n=0}^{\infty} (A_n \cos k_n vt + B_n \sin k_n vt) \sin k_n z$$

in which

$$k_n = \frac{2n+1}{2} \frac{\pi}{\ell} \quad , \quad n = 0,1,2,\cdots \quad . \tag{3.50}$$

Either by Eq. 3.33 or by Eq. 3.34, the constants above can be related. Then using the initial conditions, Eqs. 3.48 and 3.49, one obtains the following result for the current and the voltage along the line.

$$I(z,t) = \frac{1}{R}\sum_{n=0}^{\infty} (-A_n \sin k_n vt + B_n \cos k_n vt)\cos k_n z \tag{3.51}$$

$$V(z,t) = \sum_{n=0}^{\infty} (A_n \cos k_n vt + B_n \sin k_n vt)\sin k_n z \tag{3.52}$$

where the constants are given by

$$R = (L/C)^{1/2} \tag{3.53}$$

$$A_n = \frac{2}{\ell}\int_0^{\ell} V_o(z_1)\sin k_n z_1 dz_1 \tag{3.54}$$

$$B_n = \frac{2}{\ell}\int_0^{\ell} I_o(z_1)R \cos k_n z_1 dz_1 \quad . \tag{3.55}$$

For arbitrary sample functions V_o, I_o, the solutions in Eqs. 3.51 and 3.52 are periodic in time. The fundamental period of the solution is readily found to be the two-way transit time along the line, and therefore the corresponding fundamental frequency is given by

$$f_o = \frac{v}{2\ell} \quad . \tag{3.56}$$

Now, the correlation function for $V(z,t)$ can be computed. Substituting Eq. 3.52 into the defining equation gives

$$RR_v(\rho,\tau) = \left\langle V(z,t)\ V(z-\rho,t-\tau)\right\rangle$$

$$RR_v(\rho,\tau) = \frac{v}{2\ell^2}\int_0^{\ell}\int_0^{2\ell/v} \left\langle V(z,t)\ V(z-\rho,t-\tau)\right\rangle_{v_o,i_o} dz\ dt \tag{3.57}$$

Three subordinate determinations are required in carrying out the indicated integrations and the ensemble average in Eq. 3.57. After integration with respect to t, the following intermediate form is obtained.

$$RR_v(\rho,\tau)= \frac{1}{2\ell} \sum_{n=0}^{\infty} \left\langle A_n^2 + B_n^2 \right\rangle_{v_o,i_o} \cos k_n v\tau \int_0^{\ell} \sin k_n z \sin k_n(z-\rho)\, dz \quad . \qquad (3.58)$$

The integration with respect to z is more direct and the result is

$$RR_v(\rho,\tau)= \frac{1}{4} \sum_{n=0}^{\infty} \left\langle A_n^2 + B_n^2 \right\rangle_{v_o,i_o} \cos k_n v\tau \cos k_n\rho \;. \qquad (3.59)$$

Now, from Eqs. 3.39, 3.49, and 3.54, one can relate $\left\langle A_n^2 \right\rangle$ to the fundamental source variables, $\overline{\epsilon}$ and R. The essential details of the computation are as follows.

$$\left\langle A_n^2 \right\rangle = \left(\frac{2}{\ell}\right)^2 \int_0^{\ell}\int_0^{\ell} \left\langle V_o(z_o)V_o(z_1) \right\rangle \sin k_n z_o \sin k_n z_1 dz_o dz_1$$

$$\left\langle A_n^2 \right\rangle = \frac{4\overline{\epsilon}Rv}{\ell^2} \int_0^{\ell}\int_0^{\ell} \delta\left(\frac{z_o - z_1}{v}\right) \sin k_n z_o \sin k_n z_1 dz_o dz_1$$

$$\left\langle A_n^2 \right\rangle = \frac{v}{\ell}\,(2\overline{\epsilon}R) \quad . \qquad (3.60)$$

Similarly, from Eqs. 3.39, 3.48, and 3.55, it follows that

$$\left\langle B_n^2 \right\rangle = \frac{v}{\ell}\,(2\overline{\epsilon}R) \quad . \qquad (3.61)$$

Hence, by Eqs. 3.56, 3.59, 3.60, and 3.61, the correlation function for V(z,t) is given by

$$RR_v(z_o - z_1, \tau) = 2\overline{\epsilon} f_o R \sum_{n=0}^{\infty} \cos k_n(z_o - z_1) \cos k_n v\tau \quad . \qquad (3.62)$$

By Eqs. 3.13 and 3.50, the corresponding mixed correlation-spectral density function is

$$RS_v(z_o-z_1,\omega) = \bar{\epsilon} f_o R \sum_{n=0}^{\infty} \cos k_n(z_o-z_1)\left[\delta(f-\frac{2n+1}{2}f_o)+\delta(f+\frac{2n+1}{2}f_o)\right] . \tag{3.63}$$

To obtain the analogous formulas for $I(z,t)$ it is only necessary to notice that in the computation for RR_v the sign of A_n drops out in the integration with respect to t and the subsequent manipulation in going from Eq. 3.57 to Eq. 3.58. Hence, comparing Eqs. 3.51 and 3.52, one can write the following correlation function for $I(z,t)$ by direct analogy to Eq. 3.62.

$$RR_i(z_o-z_1,\tau) = \frac{2\bar{\epsilon} f_o}{R} \sum_{n=0}^{\infty} \cos k_n(z_o-z_1)\cos k_n v\tau \quad . \tag{3.64}$$

Similarly, by Eq. 3.63, the mixed correlation-spectral density function is

$$RS_i(z_o-z_1,\omega) = \frac{\bar{\epsilon} f_o}{R} \sum_{n=0}^{\infty} \cos k_n(z_o-z_1)\left[\delta(f-\frac{2n+1}{2}f_o)+\delta(f+\frac{2n+1}{2}f_o)\right] . \tag{3.65}$$

The above result shows that the trapped noise currents have a discrete frequency spectrum as well as having spatial correlation. Using a voltmeter probe with a bandpass filter tuned to $f = \frac{2n+1}{2} f_o$ and with a bandwidth which is less than f_o, the readings of the voltmeter are identical to those which would be obtained from a single-frequency source.

Since for an antenna the loss per cycle by radiation is very much less than the total stored energy, it is permissible to extend the above analysis, qualitatively, to the case of a thermally excited thin wire antenna. Consider what happens to a small amount of thermal energy which is delivered to the wire by some lossy element of the system. Apparently, this energy oscillates between $-\ell$ and $+\ell$, slowly decreasing in quantity due to the losses by radiation. However, the multiple traverses are periodic; and by analogy to the preceding analysis, the thermal currents tend to become correlated. Since the radiation field is dependent upon the total thermal current, the radiation field, itself, can be expected to show traces of the interference phenomenon which is associated with fully correlated source currents. Since by Eq. 3.65, the frequencies which are present in the non-radiating case are given by $\frac{1}{2} f_o, \frac{3}{2} f_o, \frac{5}{2} f_o, \cdots$, it is expected that the thermal radiation pattern, say, at a frequency near $\frac{3}{2} f_o$ will bear a strong resemblance to that for the same antenna element when driven by a coherent source at the $\frac{3}{2} f_o$ frequency.

IV NOISE SOURCES

In this section two sources of thermal noise are considered for radiation measurements. These are the heated wire and the glow discharge. Although these two are macroscopically quite dissimilar, it is well known that in each of them the same phenomenon, the chaotic motion of electrons, gives rise to a noise spectrum which is essentially flat in the radio-frequency band.* Hence, either of these two types of noise source is potentially useful in experimental investigations which are designed to demonstrate the validity of the spatially distributed model of thermal-electric noise described in Sec. 3. However, the computations presented in this section indicate an appreciable advantage in signal strength for the glow discharge source due to the considerably higher average temperature of the plasma electrons as compared to that of the conduction electrons in a metal. A third type of source, which could be very useful in this work, but which is not considered further here, is a simulated distributed noise source, e.g., an array of infinitesimal radiators each driven by the amplified output of a temperature-limited vacuum tube. With this method, the effective noise temperature could be made extremely high.

4.1 Microwave Emissivity of Heated Wires

The emissivity of a metallic surface at a temperature T is readily computed for the optical frequencies from Fresnel's reflection formulas and Kirchhoff's radiation law (see Sec. 2.4.2). A similar approach at microwave frequencies would seem to suggest a consideration

---

*An account of the major contributions in this field is given in Sec. 1.

based on the analyses in the literature for the scattering cross-section of wires, plates and other objects. This is not a fruitful avenue of approach, however; for these analyses usually treat only the perfect conductor case, and absorption, if it occurs, is due to a lumped terminating impedance rather than to distributed wire losses.

In this section a formulation is presented for computing the microwave emissivity of an antenna. It is based upon the thermodynamic principle of detailed balancing of radiation and upon antenna theory. Although presented by an example (for the case of a long thin wire) which involves computational approximations, the method itself appears to be exact and readily applicable, at least in principle, to an arbitrary radiator configuration. The analysis demonstrates in a direct way that a multi-lobe thermal radiation pattern is to be expected whenever a characteristic radiator dimension and the wavelength under observation are of the same order of magnitude. Also, the equations enable one to make, simply, a numerical estimate of the thermal signal level in the radiation field.

4.1.1 Incident Poynting Vector in Isothermal Enclosure. Consider a lossy wire in thermal equilibrium with the walls of a large isothermal enclosure (Fig. 4.1). From Eq. 2.4, the spectral intensity of the incident power per unit of receiver area which is incident on the origin from a portion of the enclosure which subtends a solid angle $d\Omega$ is

$$dP_{fA}df = \frac{2f^2 df}{c^2} \bar{\epsilon}\, d\Omega \quad . \tag{4.1}$$

For a sufficiently large enclosure the electromagnetic energy, incident from this portion of the wall, is a randomly polarized plane wave, with its components in the $\underline{u}_1 - \underline{u}_2$ plane. The spectral intensity of the

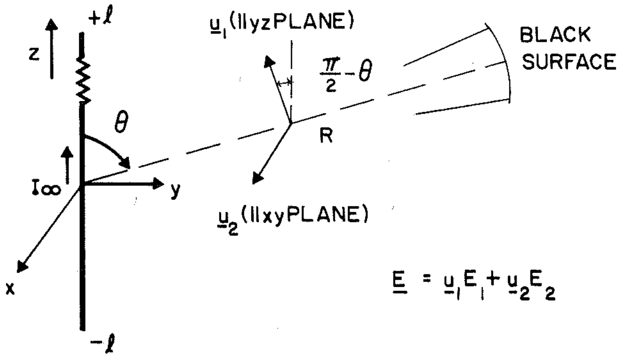

Fig. 4.1. Lossy wire in thermal equilibrium

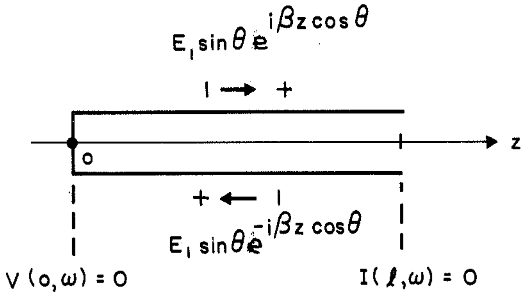

Fig. 4.2. Induced current model

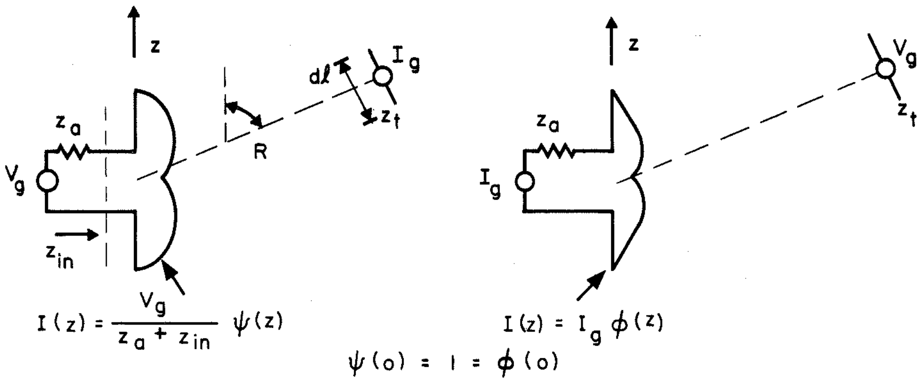

Fig. 4.3. Reciprocity relationships

electric field has components S_{e1} and S_{e2} corresponding to the electric field components along $\underline{u}_1$ and $\underline{u}_2$ respectively. They are defined by

$$S_{e1,2} = \lim_{T \to \infty} \left\langle \frac{E_{T1,2}(\omega)\ E^{*}_{T1,2}(\omega)}{2T} \right\rangle_e \quad . \tag{4.2}$$

In the time domain, Poynting's theorem applied to this case states that the power per unit area is the following sum

$$p_a(t) = \frac{1}{\eta_o} \left[e_1^2(t) + e_2^2(t) \right] \quad . \tag{4.3}$$

In Eq. 4.3, the lower case letters are used in order to emphasize the time dependence. From this, the spectral form, Eq. 4.4, follows

$$P_{fA} df = \frac{2}{\eta_o} \left[S_{e1} + S_{e2} \right] df \quad . \tag{4.4}$$

The multiplier "2" is introduced because of our convention that P_{fA} is a one-sided spectral intensity and S_e is two-sided. Equations 4.1 and 4.4 are combined noting that for random polarization $S_{e1} = S_{e2}$, and the following expression for the spectral intensity of the electric field from $d\Omega$ results.

$$S_{e1\Omega} df = S_{e2\Omega} df = \frac{\eta_o f^2 df}{2c^2} \bar{\epsilon}\, d\Omega \ . \tag{4.5}$$

<u>4.1.2 Induced Current Distribution.</u> The currents induced in the wire by the incident radiation are calculated in an approximate fashion using the transmission line model of Schelkunoff (Fig. 4.2) (18),(19). Expressed in Fourier transform notation, the transmission line equations are

$$\frac{\partial V}{\partial z} = -ZI + E_1(\omega)\sin\Theta e^{-i\beta R}\left[e^{i\beta z\cos\Theta} + e^{-i\beta z\cos\Theta}\right] \qquad (4.6)$$

$$\frac{\partial I}{\partial z} = -YV \qquad (4.7)$$

where the distributed nature of the inducing field accounts for the form of the right member of Eq. 4.6, with the $\sin\Theta$ appearing because only the z-component of the electric field induces currents. Z and Y are the series impedance/length and the shunt admittance/length, respectively; and their product satisfies the relation $ZY = -\beta^2$. Equations 4.6 and 4.7 give

$$\frac{\partial^2 I}{\partial z^2} + \beta^2 I = -2YE_1(\omega)\, e^{-i\beta R}\cos(\beta z\cos\Theta) \qquad (4.8)$$

which must be solved subject to the boundary conditions:

$$\begin{aligned} I(\ell,\omega) &= 0 \\ V(0,\omega) &= 0 \quad . \end{aligned} \qquad (4.9)$$

The following solution for the induced current is readily obtained

$$I(z,\omega) = AE_1(\omega)[\cos\beta z\cos(\beta\ell\cos\Theta) - \cos\beta\ell\cos(\beta z\cos\Theta)] \qquad (4.10)$$

in which the constant A is given by

$$A = \frac{2Ye^{-i\beta R}}{\beta^2\sin\Theta\cos\beta\ell} \quad . \qquad (4.11)$$

In the final form, an expression containing Y is not convenient. This is due to the fact that this parameter is only an intermediate variable which enters into some analyses for the input impedance of a linear antenna, z_{in} ; and although the literature contains extensive references to z_{in} there is a little about Y. An alternate z_{in}-dependent form of this constant, A in Eq. 4.11, is derived following Schelkunoff (18) and Weber (19).

From Eq. 4.10, the current at $z = 0$, I_{oo} in Fig. 4.1, is given by

$$I_{oo} = AE_1(\omega)\ [\cos(\beta \ell \cos \Theta) - \cos \beta \ell)] \quad . \tag{4.12}$$

This current can be related to z_{in} by the reciprocity theorem (Fig. 4.3). Consider transmission from the antenna, effective height h, to an infinitesimal test dipole of length $d\ell$. The test dipole current is

$$I_g = \frac{E_o d\ell}{z_t}$$

where E_o is the far-zone field of the transmitting antenna and z_t is the total impedance of the test dipole. Now, expressing E_o in terms of the transmitter current, one obtains the following equation.

$$I_g = \frac{i\omega\mu \sin \Theta\ e^{-i\beta R}}{4\pi R} \frac{V_g}{z_{in} + z_a} \left[\int_{-\ell}^{\ell} \psi(z)\ e^{i\beta z \cos \Theta}\ dz \right] \frac{d\ell}{z_t} \quad . \tag{4.13}$$

$\psi(z)$ is the normalized current distribution for the long antenna during transmission, V_g is the generator voltage, and $z_{in} + z_a$ is the total impedance. Now, interchange the generator and ammeter. From the reciprocity theorem, the $z = 0$ current is exactly I_g. No other definitive statement is made, however, relating the current distribution during reception, $\phi(z)$, to that during transmission $\psi(z)$. Define the effective height h as follows:

$$I_g = \frac{E_z h}{z_{in} + z_a} \quad . \tag{4.14}$$

The electric field in the far-zone of the test dipole is

$$E_1 = \frac{i\omega\mu \;\; e^{-i\beta R}}{4\pi R} \;\; \frac{V_g d\ell}{z_t} \quad . \tag{4.15}$$

Since $E_z = E_1 \sin \Theta$, Eq. 4.14 can be rewritten as

$$I_g = \frac{i\omega\mu \sin \Theta \; e^{-i\beta R}}{4\pi R} \; \frac{V_g d\ell}{z_t(z_{in} + z_a)} \; h \quad . \tag{4.16}$$

Equating Eqs. 4.13 and 4.16 for I_g one obtains

$$h = \int_{-\ell}^{\ell} \psi(z) \; e^{i\beta z \cos \Theta} \; dz \quad . \tag{4.17}$$

This is substituted into Eq. 4.14, giving the following relationship between the induced load current, I_g, the z-component of the incident electric field, E_z, and the normalized current distribution during transmission, $\psi(z)$,

$$I_g = \frac{E_z}{z_{in} + z_a} \int_{-\ell}^{\ell} \psi(z) \; e^{-\beta z \cos \Theta} dz \tag{4.18}$$

and therefore the following exact relationship is obtained for the case in which $z_a = 0$.

$$I_{\infty} = \frac{E_z}{z_{in}} \int_{-\ell}^{\ell} \psi(z) \; e^{i\beta z \cos \Theta} dz \quad . \tag{4.19}$$

Using the transmission line analogy again, Eqs. 4.6 and 4.7 are solved for the case of a concentrated source at $z = 0$, i.e., the generator, and the following approximate equation is obtained for $\psi(z)$.

$$\psi(z) = \frac{\sin\beta(\ell - |z|)}{\sin\beta\ell} \quad . \tag{4.20}$$

Substituting Eq. 4.20 into Eq. 4.19 and integrating, one obtains

$$I_{oo} = \frac{2E_g}{\beta z_{in}} \left(\frac{\cos(\beta\ell\cos\Theta) - \cos\beta\ell}{\sin^2\Theta\sin\beta\ell}\right) \quad . \tag{4.21}$$

The alternate expression for A is found by comparing Eqs. 4.12 and 4.21; the final result is

$$A = \frac{2}{\beta z_{in}\sin\Theta\sin\beta\ell} \quad . \tag{4.22}$$

4.1.3 Absorption and Radiation of Thin Wire in Isothermal Enclosure. In the general case, there is absorption both in the terminating impedance, z_a, and in the wire losses. Since in the case under consideration $z_a = 0$, the total dissipation is given by the following integration for the wire loss

$$p_t(t) = \int_{-\ell}^{\ell} i^2(z,t) R_s \, dz \quad . \tag{4.23}$$

The current $i(z,t)$ contains an induced term due to the incident field and an internal term due to thermal agitation. In Eq. 4.23 the resistance /length, R_s, is given from eddy current considerations as

$$R_s = \frac{1}{2\pi a\,\sigma\delta}$$

or by

$$R_s = \frac{\omega\mu\,\delta}{4\pi a} \tag{4.24}$$

where $\delta = (2/\omega\mu\sigma)^{1/2}$. Equation 4.24 assumes that the skin depth satisfies the following inequality, $\delta \ll a$. It is assumed, for the sake of simplicity, that the induced and the internal components of $i(z,t)$ are uncorrelated. Then, in taking the average of Eq. 4.23, one can separate out the term which represents absorption of the incident radiant energy. The spectral intensity of this absorption is given by

$$S_p = \int_{-\ell}^{\ell} S_i(z,\omega)\, R_s dz \tag{4.25}$$

in which $S_i(z,\omega)$ is the spectral intensity of the induced current alone. Therefore, computing $S_i(z,\omega)$ from Eq. 4.10 and substituting in Eq. 4.25, it follows that

$$S_p df = AA^* R_s S_{el\Omega} df \int_{-\ell}^{\ell} \left[\cos \beta z \cos(\beta\ell \cos\Theta) - \cos \beta\ell \cos(\beta z \cos\Theta)\right]^2 dz \tag{4.26}$$

Equation 4.26 is integrated and rearranged, substituting from Eqs. 4.5 and 4.22 for S_{el} and AA^*, respectively. The resulting one-sided expression for the power absorbed, in df, incident from $d\Omega$, is given by equation 4.27 below.

$$P_{f\Omega} df\, d\Omega = 2S_p\, df\, d\Omega$$

$$P_{f\Omega} df\, d\Omega = \frac{2\eta_0^2\, \delta\, \bar{\epsilon}}{(2\pi)^3 a \left|z_{in}\right|^2 \sin^2 \beta\ell}\, \phi(\Theta,\beta\ell) df\, d\Omega \tag{4.27}$$

in which $\phi(\Theta,\beta\ell)$ is defined by

$$\phi(\Theta,\beta\ell) = \frac{1}{\sin^2\Theta}\Bigg\{\beta\ell\left[\cos^2\beta\ell + \cos^2(\beta\ell\cos\Theta)\right]$$

$$+ \sin\beta\ell\cos\beta\ell\cos^2(\beta\ell\cos\Theta)\left[1 - \frac{4}{\sin^2\Theta}\right]$$

$$+ \cos^2\beta\ell\sin(\beta\ell\cos\Theta)\cos(\beta\ell\cos\Theta)\left[\frac{1}{\cos\Theta} + \frac{4}{\sin^2\Theta}\right]\Bigg\} \ . \quad (4.28)$$

By the principle of detailed balancing of radiation (20) which states that in thermodynamic equilibrium for any space-frequency interval, $d\Omega$-df, the power absorbed by a body is equal to the power radiated by that body, it follows that the power radiated by the lossy wire into the solid angle $d\Omega$ is also given by Eqs. 4.27 and 4.28. Furthermore, since the radiant energy emitted by the wire is not related to the temperature of the surroundings, it follows that the thermal radiation pattern of the long wire at a temperature T is likewise given by Eqs. 4.27 and 4.28.

An asymptotic form of Eq. 4.27 is considered in this paragraph. A computational comparison in Appendix VI shows that an order of magnitude agreement exists between $|z_{in}|$ and $|z_r|$, the simple reactive approximation to the input impedance given by Eq. A-6.9. Hence, the following approximation to z_{in} is made provided $\beta\ell \gg 1$ and provided $\beta\ell$ is not in the range of values which gives a zero of impedance. The approximation is

$$z_{in} \doteq z_r = -iz_o \cot\beta\ell \quad (4.29)$$

in which by Eq. A-6.8, z_o is given as

$$z_o = 120 \left[\ell n \frac{1}{\beta a} + 0.116 + \frac{\sin \beta \ell}{\beta \ell} \right]$$

which is roughly,

$$z_o = 120 \ \ell n \frac{1}{\beta a} \quad . \tag{4.30}$$

Substitution of Eqs. 4.29 and 4.30 into Eq. 4.27 leads to the following approximate form for the radiation intensity.

$$P_{f\Omega} df \, d\Omega = \frac{\delta \, \overline{\epsilon}}{4\pi a \left[\cos \beta \ell \ \ell n(1/\beta a) \right]^2} \phi(\theta, \beta \ell) df \, d\Omega \tag{4.31}$$

$\phi(\theta,\beta\ell)$ is given by Eq. 4.28. The reason for the above-stated restriction on the range of $\beta\ell$, so as to avoid the zero of impedance, is clear from Eq. 4.31. These zeros occur for $\cos \beta\ell = 0$, i.e., $2\ell/\lambda = (2n+1)/2$ where $n = 0,1,2,3,\cdots$; and they introduce a singularity in $P_{f\Omega}$. This singularity is a peculiarity of the approximation; and it is not encountered if an accurate formulation is used for z_{in}. This asymptotic form for the radiation intensity is of particular interest, because the coefficient, $\delta\overline{\epsilon}/(4\pi a[\cos \beta\ell \ \ell n(1/\beta a)]^2)$, is essentially the same as that in the formula for the radiation from a thin wire which is derived by Levin and Rytov on an entirely different basis (8). Thus, it is probable that Eq. 4.27 gives a more accurate approximation than either Eq. 4.31 or the result in the above-cited reference.

<u>4.1.4 Experimental Aspects of the Detection Problem.</u> The spatial distribution of thermal energy for a heated wire is given by Eqs. 4.27 and 4.28. The numerical determination of z_{in} is presented in detail

in Appendix VI. Hence, for arbitrary T, β, ℓ, a and σ , the absolute level of the radiant energy can be computed. It is shown below, that the levels of radiation are quite low; and in general, to measure these low-level patterns one should use the maximum coupling to the receiving apparatus that is consistent with the following restrictions:

(1) The solid angle subtended by the receiving apparatus at the source must be limited in order to prevent undue smoothing of the radiation pattern.

(2) The receiving antenna should be in the Fraunhofer region of the radiator.

The determination of the quantitative limits imposed by the above restrictions is described in detail in Appendix IV. The results are summarized in Eqs. 4.32 and 4.33. The controlling range requirement is

$$R = \frac{4\ell\, L_a}{\lambda} \qquad \text{(based on smoothing)} \qquad (4.32)$$

in which ℓ is the half-dimension of the radiator and L_a is the full-dimension of the receiving aperture. The maximum effective solid angle subtended by a microwave horn of optimum dimensions is given by

$$\Omega = \frac{\alpha_e L_a L_b}{R^2}$$

$$\Omega = \frac{(0.50)(0.81)\, L_a^2}{R^2} \qquad (4.33)$$

$$\Omega = 2.53 \times 10^{-2}\, (\lambda/\ell)^2 \quad .$$

Computation for a representative case, i.e., $2\beta\ell = 9\pi$ gives a propagation loss of 1/1040 (Appendix IV). From Eq. 4.33, the maximum solid angle is $2.53 \times 10^{-2}/(2.25)^2$ or 5.0×10^{-3} steradians. Using a sophisticated horn-lens system, a maximum increase by tenfold is envisaged.

The signal level at the input to the receiver is conveniently characterized by an effective Nyquist temperature, $\overline{\epsilon}_a$, defined in accord with Eq. 3.25 by

$$\int_{\Omega} P_{f\Omega}\, df\, d\Omega = \overline{\epsilon}_a\, df \qquad (4.34)$$

where the integration is over the receiving aperture.

A numerical example provides a convenient method of summarizing the difficulties inherent in the experimental detection of thermal radiation patterns at microwave frequencies. Consider the normal or broadside direction, $\Theta = \pi/2$, and assume $\beta\ell \gg 1$. Then, combining Eqs. 4.27, 4.28, and 4.34, and solving for the ratio $\overline{\epsilon}_a/\overline{\epsilon}$, one obtains the equation

$$\frac{\overline{\epsilon}_a}{\overline{\epsilon}} = \frac{6\beta\ell\, \delta\, \eta_o^2 \Omega}{(2\pi)^3 a |z_{in}|^2} \qquad (4.35)$$

Then, eliminating δ by Eq. 4.24 and substituting the following numerical values:

$2\beta\ell = 9.5\pi$
$f = 9200$ mc/s
$\Omega = 2.70 \times 10^{-3}$ steradian (by Eq. A-5.1)

one obtains the following equation for the ratio of the apparent received temperature to the source temperature.

$$\frac{\overline{\epsilon}_a}{\overline{\epsilon}} = \frac{7.28 \times 10^{-2}}{a|z_{in}|^2 \sigma^{1/2}} \qquad (4.36)$$

In Fig. 4.4, this ratio is plotted as a function of the conductivity for three values of the parameter λ/a, specifically $\lambda/a = 10$, 100, and 1000. The appropriate values of $|z_{in}|^2$ are computed in Appendix VI. At points (a) and (b) the skin depth is one-tenth of the radius, i.e., $\delta \doteq a/10$, for the $\lambda/a = 100$ and $\lambda/a = 1000$ curves, respectively; and the analysis becomes less accurate as σ decreases from these points. Also shown in this figure are the conductivities for two materials capable of operation at elevated temperatures. The value of using a "lossy" conductor is evident. Even so, using a rod of silicon carbide with an operating temperature of 1800°K, the apparent received temperature is approximately $T_a = (\overline{\epsilon}_a/\overline{\epsilon})1800 \doteq 0.18^{\circ}$K. Present-day wideband radiometer receivers can be designed to detect signals at this level and, in fact, far enough below this level so that a radiation pattern could be measured. Unfortunately, however, the use of a wideband receiver is precluded, since it smooths out some of the interesting pattern variations. On the other hand, present-day narrow-band radiometers (up to about 50 mc/s) can detect this signal level; but it is not a practical level for measuring radiation patterns (see Appendices I,II,III). Without some technique for increasing the source temperature well above 2000°K, the measurement of microwave, thermal-radiation patterns from metallic rods will have to wait for the development of a narrow-band receiver with an effective noise level of about 0.01 rms$^{\circ}$ K.

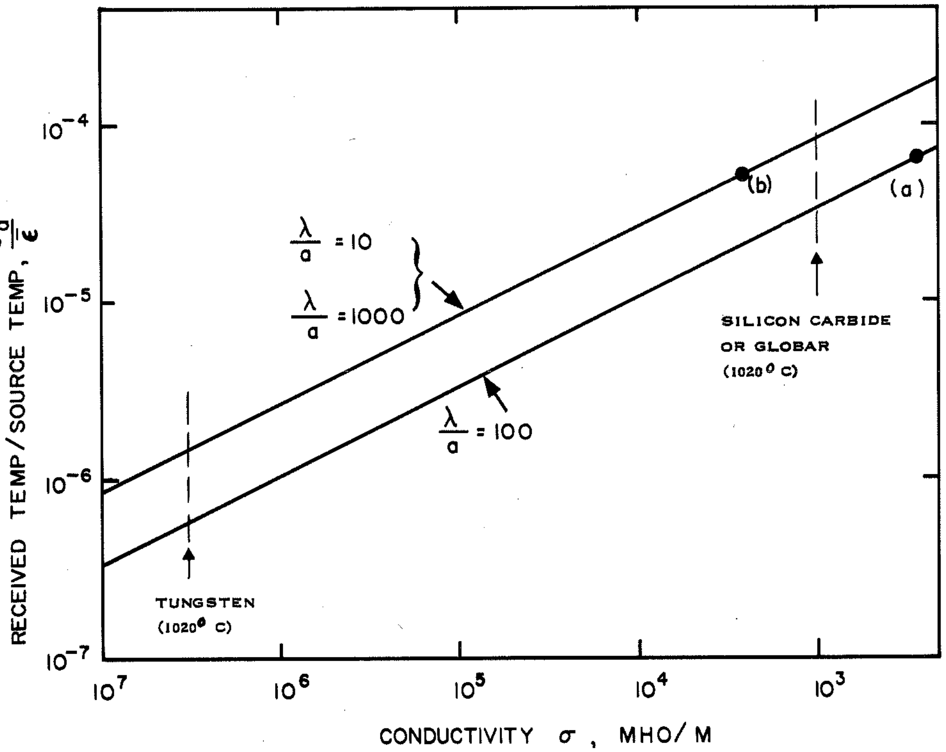

Fig. 4. 4. Receiver temperature/source temperature vs. conductivity ($f = 9200$ Mc/s, $2\beta\ell = 9.5\pi$, $R = 2(2\ell)^2/\lambda$, $\Omega = 2.70 \times 10^{-3}$ rad.^{2})

4.2 Radiation Temperature of a Gaseous Discharge

The noise properties of a gaseous discharge have been studied experimentally and theoretically from a terminal point of view. In a series of experiments with d-c discharges in mixtures of mercury vapor and argon, Mumford (3) and later Easly and Mumford (21) report a very close agreement between the kinetic temperature of the plasma electrons and the effective Nyquist's temperature of the source. The agreement reported is, typically, within 3%. Parzen and Goldstein (4) have derived an expression for the spectral intensity of the total electron current in a d-c discharge. For the one-sided spectral intensity of available power, P_f, their final result is given, within a few percent, by

$$P_f = kT_e \qquad (4.37)$$

in which T_e is the temperature of the plasma electrons. In the type of low pressure, low current discharge under consideration, the kinetic temperatures of the other plasma constituents are much lower than T_e and their effect may be neglected. Thus, the above result is also expected from Nyquist's general derivation, i.e., Eqs. 4.37 and 3.24 are expected to agree. Since from the terminal point of view, the expected close agreement between the electron temperature and the noise temperature has been experimentally verified, one can infer that the electron temperature is also appropriate for the noise temperature in the Leontovich-Rytov distributed random electric field, i.e., the $\overline{\epsilon}$ in Sec. 3.4 .

The electron temperature in the positive column of a d-c discharge can be computed from a theoretical result derived by Schottky (1924) and later refined by Tonks and Langmuir and others (22). Consider a tube which has the following characteristics*: argon filled, pressure 30.0 ± 0.3 mm Hg, diameter 0.765 cm ID and 0.953 cm OD, length 21.2 cm, current 200 ma, and voltage drop 71 v. Equation 8.36 of von Engel is

$$\frac{e^x}{x^{1/2}} = 1.2 \times 10^7 \, (cpr)^2 \tag{4.38}$$

where $x = eV_i/kT$, c is 4×10^{-2} for argon, p is mm Hg pressure, r is cm radius, and V_i is the ionization potential. Substituting the values $V_i = 15.7$v and $cpr = 0.459$ into Eq. 4.38, one obtains an electron temperature given by $T = 11{,}300^\circ K$. This is in comparison to the measured noise temperature of $T = 10{,}072^\circ K$. The computed value and the measured value show fair agreement, and for our purposes, sufficient accuracy is obtained with the assumption that the effective source temperature is given by

$$T = 10{,}100^\circ K \, . \tag{4.39}$$

From Eq. 4.38, it follows also that the kinetic temperature of the plasma electrons is constant over a wide range in the discharge current.

Now, it is clear that the gaseous discharge is potentially a better source of thermal radiation than the heated wire. There are two reasons for this. First, the plasma electrons have a kinetic

---

*These values are selected from the manufacturer's data for the Bendix Tube No. 6357/TD-11. The commercial use of this tube is as a random-noise generator. The manufacturer's specification on the noise temperature is that $10 \log (T/290 - 1) = 15.28 \pm 0.1$ db which corresponds to a temperature given by $T = 10{,}072 \pm 200^\circ K$.

temperature which is considerably higher than it is practical to heat the conduction electrons. Secondly, the lower conductivity of the plasma means a higher emissivity. A very simple, approximate computation serves to stress these advantages of the gaseous discharge. Consider an aperture of dimensions a by b in a metal plane, i.e., the slotted plane of Fig. 5.1. The aperture is illuminated by an argon source for which $T = 10{,}100^{o}K$. If one neglects subtleties of aperture size, slot impedance, and plasma conductivity, then by Eq. 2.4, the spectral intensity of power intercepted by a receiver of solid angle Ω is given by

$$P_{f\Omega}\Omega = \frac{2ab\,\overline{\epsilon}}{\lambda^2}\Omega \qquad (4.40)$$

Since only one polarization is absorbed, the spectral intensity of received power, P_f, is given by

$$P_f = \frac{1}{2} P_{f\Omega}\Omega$$

and the effective Nyquist temperature, $\overline{\epsilon}_a$, defined by analogy to Eq. 4.34, is given by

$$\frac{\overline{\epsilon}_a}{\overline{\epsilon}} = \frac{ab\,\Omega}{\lambda^2} \quad . \qquad (4.41)$$

The effective Nyquist temperature is computed for two cases of interest. First, for the case of maximum coupling, by Eq. 4.33, the solid angle subtended by the receiver is

$$\Omega \doteq 5\text{x}10^{-3} \text{ sterad} \quad \text{for} \quad \beta a = 9.5\pi$$

and if $b/\lambda = 0.1$, then $T_a = 24^{o}K$. (4.42)

Secondly, for the pattern recorder which is described in the Appendices by Eq. A-5.1, the actual solid angle, Ω, and the typical slot dimensions are as follows:

$$\Omega \doteq 2.7 \times 10^{-3} \text{ sterad}, \quad \beta a = 9.5\pi, \quad b/\lambda = 0.12$$

and thus

$$T_a = 16^{\circ}\mathrm{K} \quad . \tag{4.43}$$

Due to the approximate nature of the above computation, these values must be regarded as order of magnitude determinations only. In any event, with a radiometer receiver, these temperature increments are easily measured, and a comparison to the Fig. 4.4 values clearly shows the advantage of the gaseous discharge over the heated wire.

4.3 Radiation Characteristics of an Argon Discharge

In this section there is a description of a measurement of the level of radiation received from a thin slot which is excited by a gaseous discharge. This experiment is a preliminary to the measurement of the complete radiation pattern of a noise-excited thin slot (see Sec. 5.7). It is presented at this point in order to focus attention on an important observed characteristic of the noise source, namely, that the level of the radiation is nearly independent of the d-c discharge current. The experiment is described in more detail in the next paragraph.

In the experiment a thin slot which is 9.5π by 0.24π radians length at 9200 mc/s is excited by the radiation from a d-c discharge in an argon column*. The radiation is recorded using a Dicke

---

* The noise source is described in Sec. 4.2.

radiometer*. The receiving aperture is positioned in the Fraunhofer region of the slot at a range of 1.50 m, and it subtends an effective solid angle of 2.70×10^{-3} steradians. The received signal is measured as a function of the d-c current in the argon discharge. Figure 4.5 shows the variation in the received signal versus the discharge current for two different angles of emission and for three tubes which represent two separate lots. From this data the following observations are made. For an increase of 3.3 to 1 in the discharge current, the increase in the signal level averaged over both angles of emission is 1.25 to 1. The ratio of the emission at an angle of $\theta - \pi/2 = 0$ to that at 63° shows a small decrease over this same range of current. The absolute level is approximately 5°K, which is in good agreement with the order of magnitude computation of 16°K in Eq. 4.43.

From this experiment it is concluded that the coupling of energy from the plasma column to the aperture takes place predominantly as radiation radially outward from the plasma column. It appears that there is negligible slot excitation resulting from noise energy which after emission propagates as a guided mode remaining closely-coupled to the plasma column. The above conclusion is based on the following reasoning. For the characteristic parameters of the discharge used, the attenuation constant for the propagation of the principal mode is high and furthermore it is proportional (approximately) to the square of the plasma frequency, ω_p^2, which is in turn proportional to the electron concentration and hence to the discharge current. Therefore, for the principal mode, a 3 to 1 increase in the discharge current causes approximately a 3 to 1 increase in the exponent of a term of

---

*The pattern recording apparatus is described in Sec.5.7 and Appendices I, II, and III.

the form $e^{-\alpha z}$. It is assumed that there is a corresponding significant change in the loss factor for any of the closely-coupled dielectric modes. Then, from the observed near constancy of the radiated energy as the discharge current is varied, the above-stated conclusion is drawn.

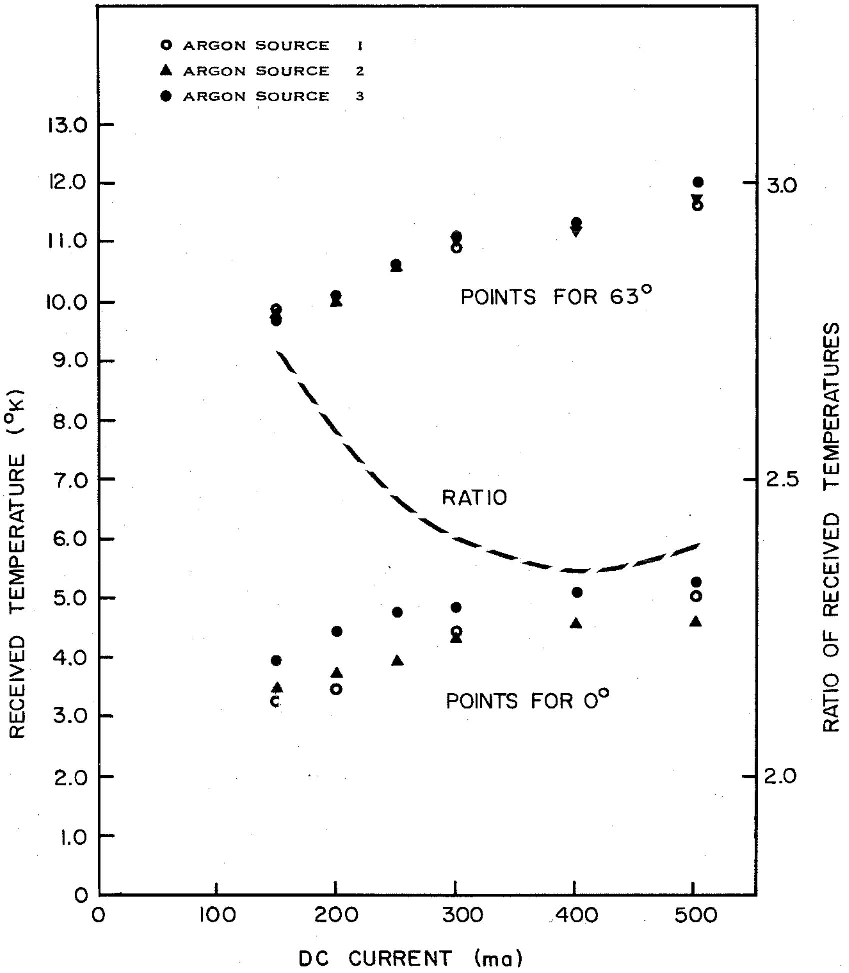

Fig. 4.5. Variation in radiation level with discharge current for 3 argon tubes

V THERMAL RADIATION PATTERNS AT MICROWAVE FREQUENCIES

5.1 Introduction

In this chapter a study is made of the thermal radiation pattern of a long thin aperture-excited slot. The principal reason for directing our attention to the problem of the thin-slot is that the experimental measurements are practical, while for the thin heated wire, they are not. In the experiments described in the concluding portions of this chapter, a glow discharge tube is mounted adjacent to a large metal plate. There is a long thin slot in the plate which runs along the axis of the discharge column. The spatial distribution of the radiation from this aperture is measured as a function of the slot length. This configuration serves as a practical approximation to the following idealization; a rectangular aperture of dimensions a by b in one planar metallic side of a large isothermal enclosure. The length "a" and the wavelength are of the same order of magnitude, and the length "b" is much smaller. Radiation incident on the aperture from within the isothermal enclosure is essentially totally reflected if the polarization of the electric field is in the "a" direction. However, for polarization in the "b" direction, there is radiation. Due to the relatively small size of the aperture, the boundary exerts a considerable influence on the radiation. The effect of the boundary in correlating the resultant aperture illumination is readily anticipated by analogy to the transmission line analysis for the trapped-noise currents (Sec. 3.5). The principal departures caused by the proximity of the plasma column to the slot are the addition of a small loss factor as well as a slight change in the phase velocity for the waves which propagate along this slot. These effects are taken into account in an approximate fashion in the analysis in Sec. 5.4 by the assumption of a complex propagation factor, β_c. In the remaining paragraphs of this introduction, the presentation of Chapter V is outlined.

In Sec. 5.2, the wave equation is solved for the aperture electric field which results from the superposition of an arbitrary distribution of induced currents, j_x or $\sigma^* E_s$, in Fig. 5.1. This induced source current distribution is a sample function of a random process. The spectral intensity of this function is of the form given by the Leontovich-Rytov formula in Sec. 3.4.

In Sec. 5.3, a general expression is derived for the radiation in the Fraunhofer region. Equations 5.27, 28, 30 represent a general formulation into which any assumed source correlation function may be substituted.

In Sec. 5.4, a delta-correlated source, Eq. 5.31, is assumed and a formula is derived for the resulting spectral intensity of the radiated power, Eq. 5.35. Special cases of this formula are considered in detail. First, the free space phase velocity is assumed for propagation along the slot; a formula for $P_{f\Omega}$ is derived, Eq. 5.36; and graphs are shown for several slot lengths and various attenuation constants, Figs. 5.3 through 5.6. Secondly, an attenuation constant of zero is assumed; $P_{f\Omega}$ is derived, Eq. 5.37, and plotted, Fig. 5.7. The spatial distribution of the radiation is in agreement with the expression of Levin and Rytov for the the thin wire (8). The approximate nature of the constant multiplier in the expressions for $P_{f\Omega}$ is stressed. Then, an asymptotic form is derived for $P_{f\Omega}$ as the angle θ goes to zero, Eq. 5.38.

In Sec. 5.5, a partially-correlated source, Eqs. 5.46 and 5.47, is assumed. The resulting radiated power, $P_{f\Omega}$, is given by Eqs. 5.52 and 5.53 and a convenient approximate formula is given in Eq. 5.55. The results are plotted in Figs. 5.8 through 5.11.

In Sec. 5.6, a fully-correlated or spatially-coherent source is assumed. An expression for $P_{f\Omega}$ is derived, Eq. 5.65, and plotted, Fig. 5.12.

In Sec. 5.7, several experimental radiation patterns are shown, Figs. 5.13 through 5.16. The patterns are seen to be in good agreement with those patterns which result from the analytical model assumed in Sec. 5.4.

5.2 Approximate Aperture Illumination for the Thin Slot

Consider a metallic plate in the $y = 0$ plane having a long thin z-oriented aperture of dimensions a,b where $a \gg b$ (Fig. 5.1). The aperture is illuminated or excited by a distributed noise source which is incoherent spatially and timewise, e.g., a closely-spaced hot wire or a plasma column. An approximate analysis for the resultant aperture distribution of the electric field is made in the following paragraphs. The effects of radiation losses are neglected; and furthermore, aside from the generation of the noise, the influence of this noise medium of contrasting ϵ,μ,σ , is assumed calculable by allowing for a perturbation in the propagation constant for the region surrounding the slot.

The vector wave equation for the electric field is obtained by taking the curl of Eq. 3.4a and substituting for $\nabla \times \underline{B}$ from Eq. 3.4b. For $\rho = 0$, $\nabla \cdot \underline{E}$ is equal to zero and Eq. 5.1 follows:

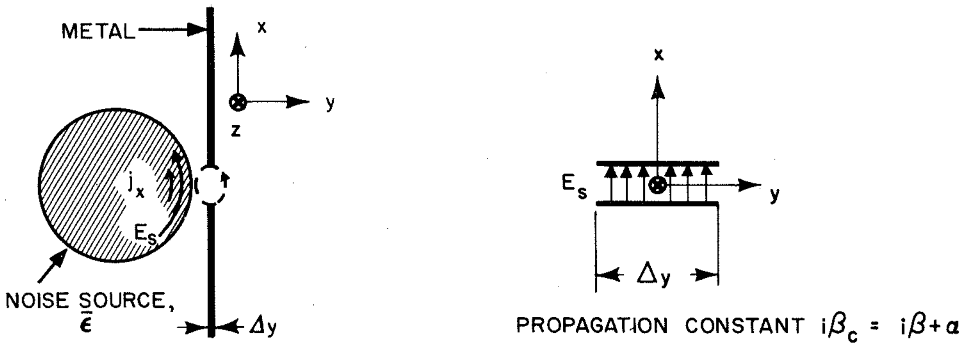

Fig. 5.1. Excitation of thin slot (left);
Principal mode approximation (right)

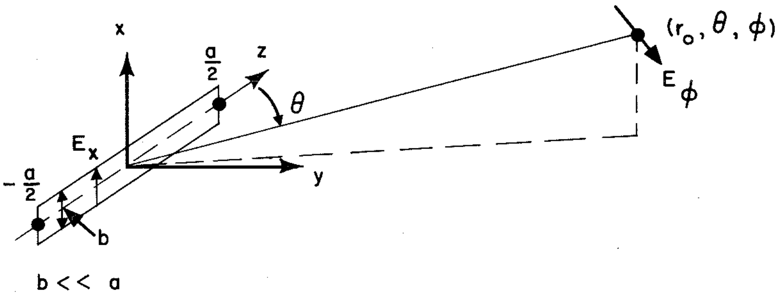

Fig. 5.2. Radiation pattern coordinates

$$\nabla^2 \underline{E} + \omega^2 \mu \epsilon \underline{E} = i\omega\mu \, \underline{j} \quad . \tag{5.1}$$

The source current, $\underline{j}$, is retained to account for the thermal noise generated in the noise source (Fig. 5.1). These source currents are related to the excitation field, E_s, by the generalized Ohm's law, which is usually written as

$$\underline{j} = \sigma^* \underline{E}_s$$

where σ^* is the complex conductivity. This relationship can also be expressed in terms of the complex dielectric constant, ϵ_p, as

$$\underline{j} = i\omega\epsilon_p \underline{E}_s$$

and therefore

$$\begin{aligned} i\omega\mu \, \underline{j} &= -\omega^2 \mu \epsilon_p \underline{E}_s \\ i\omega\mu \, \underline{j} &= -\beta_p^2 \, \underline{E}_s \end{aligned} \tag{5.2}$$

where β_p is the complex propagation factor in the noise medium. For a highly-conductive region β_p satisfies the approximate relation: $-\beta_p^2 = i\omega\mu\,\sigma$.

Now the influence of the source field E_s in the region from z to $z + dz$ is felt everywhere along the gap, since the circulating induced currents establish a displacement-current field when they re-encounter the gap discontinuity. An equivalent viewpoint is to regard the source field as propagating, mainly along the gap with a standing wave being established by the reflections at $z = \pm a/2$. Consider the one-dimensional problem in which Δy is regarded as a short section of a parallel-plane transmission line, $\underline{E}_s = \underline{e}_x E_s$, and the propagation constant, β_c, is complex. Equations 5.1 and 5.2 reduce to

$$\frac{d^2E_x}{dz^2} + \beta_c^2 E_x = -\beta_p^2 E_s(z,\omega) \tag{5.3}$$

in which the β_c is given by

$$i\beta_c = \alpha + i\beta \tag{5.4}$$

$$\beta_c^2 = \omega^2\mu\epsilon_c \quad . \tag{5.5}$$

The free space propagation factor is identified in this analysis by a subscript zero, i.e., β_o, and it is given by

$$\beta_o^2 = \omega^2\mu_o\epsilon_o \quad . \tag{5.6}$$

Since the source distribution, E_s, is a sample function of a random process, it is necessary to solve Eq. 5.3 for an arbitrary function $E_s(z,\omega)$. Also, this solution must satisfy the boundary condition of zero electric field at the short-circuited ends, i.e., $E_x(\pm a/2,\omega) = 0$. This solution is conveniently formulated in terms of the characteristic function $G(z,z_o)$ as follows. The final aperture distribution is given by

$$E_x(z,\omega) = \int_{-a/2}^{a/2} \beta_p^2 E_s(z_o,\omega)\, G(z,z_o)\, dz_o \quad , \tag{5.7}$$

in which the characteristic function is specified as the solution of the following related problem. $G(z,z_o)$ is the solution of the wave equation with a Dirac δ-function source, i.e., the solution of

$$\frac{d^2G}{dz^2} + \beta_c^2\, G = -\delta(z - z_o) \tag{5.8}$$

subject to the following boundary, slope, and continuity conditions

$$G(\pm \tfrac{a}{2}, z_o) = 0 \tag{5.9}$$

$$\underset{z_o}{\Big[} \frac{dG}{dz} = -1 \tag{5.10}$$

$$\underset{z_o}{\Big[} G = 0 \quad . \tag{5.11}$$

The general solution of Eqs. 5.8 and 5.9 is given by

$$\begin{aligned} G(z,z_o) &= A_1 \sin \beta_c(\tfrac{a}{2} + z) \,, \quad z < z_o \\ G(z,z_o) &= A_2 \sin \beta_c(\tfrac{a}{2} - z) \,, \quad z > z_o \quad . \end{aligned} \tag{5.12}$$

Substitution of Eq. 5.12 into Eqs. 5.10 and 5.11 leads to the following conditions on A_1, A_2 :

$$\begin{aligned} -A_2 \cos \beta_c(\tfrac{a}{2} - z_o) - A_1 \cos \beta_c\, (\tfrac{a}{2} + z_o) &= -\frac{1}{\beta_c} \\ A_2 \sin \beta_c(\tfrac{a}{2} - z_o) - A_1 \sin \beta_c\, (\tfrac{a}{2} + z_o) &= 0 \quad . \end{aligned} \tag{5.13}$$

Solving for A_1, A_2

$$A_1 = \frac{\sin \beta_c(\frac{a}{2} - z_o)}{\beta_c \sin \beta_c a} \,, \quad A_2 = \frac{\sin \beta_c(\frac{a}{2} + z_o)}{\beta_c \sin \beta_c a} \,, \tag{5.14}$$

substituting into Eq. 5.12, and rearranging slightly, one obtains

$$G(z,z_o) = \frac{\cos \beta_c[z+z_o] - \cos \beta_c[a-(z_o-z)]}{2\beta_c \sin \beta_c a}, \quad z < z_o$$

$$G(z,z_o) = \frac{\cos \beta_c[z+z_o] - \cos \beta_c[a-(z-z_o)]}{2\beta_c \sin \beta_c a}, \quad z > z_o . \tag{5.15}$$

Hence, from Eq. 5.15, the characteristic function for the entire interval can be written as

$$G(z,z_o) = \frac{\cos \beta_c[z+z_o] - \cos \beta_c[a-|z-z_o|]}{2\beta_c \sin \beta_c a}, \quad |z| \leq \frac{a}{2} . \tag{5.16}$$

Thus, by Eqs. 5.7 and 5.16, an arbitrary source excitation, $E_s(z_o,\omega)$ leads to an aperture distribution $E_x(z,\omega)$ given by

$$E_x(z,\omega) = \int_{-a/2}^{a/2} \beta_p^2 E_s(z_o,\omega)\, G(z,z_o) dz_o$$

$$E_x(z,\omega) = \int_{-a/2}^{a/2} \beta_p^2 E_s(z_o,\omega) \frac{1}{2\beta_c} \left\{ \frac{\cos \beta_c[z+z_o] - \cos \beta_c[a-|z-z_o|]}{\sin \beta_c a} \right\} dz_o . \tag{5.17}$$

5.3 Radiation in the Fraunhofer Region

The (approximate) tangential electric field over the $y = 0$ plane is now determined, i.e., $E_x(x,z,\omega) = E_x(z,\omega)$ of Eq. 5.17 for $|x| \leq b/2$ and $|z| \leq a/2$ and $E_x(x,z,\omega) = 0$ otherwise. The specification of the tangential electric field over the plane $y = 0$, together with the radiation condition for the field as $r_o \to \infty$ are sufficient to uniquely determine the radiation field.* The radiation

---

*Section 14.11 of Smythe or Section 9.2 of Stratton contain more complete statements of this well-known uniqueness theorem.

field is conveniently expressed in terms of the Fourier integral analog of Eq. 1-14.19 in Smythe (23). This formula gives the exact diffracted vector potential in terms of the aperture distribution for a general aperture shape. Differentiating, since $\underline{E} = -\partial \underline{A} / \partial t$, and suppressing the $e^{i\omega t}$ factor, one obtains Eq. 5.18 for the diffracted electric field vector.

$$\underline{E}(r_o,\theta,\phi,\omega) = \frac{1}{2\pi} \int_S \frac{1 + i\beta_o r}{r^2} (\underline{n} \times \underline{E}) \times \underline{e}_r e^{-i\beta_o r} dS . \qquad (5.18)$$

The notation is defined as follows:

S = surface of integration

$\underline{n}$ = unit inward normal to S

r = distance from dS to (r_o,θ,ϕ)

$\underline{e}_r$ = unit vector along r

$\underline{E}$ = Fourier integral of the electric field at dS

$\beta_o = \omega \sqrt{\mu_o \epsilon_o}$

In the Fraunhofer region, i.e., for $r_o > L_1^2/4\lambda$ where L_1 is a characteristic length of the aperture, the $1/r^2$ component is negligible and Eq. 5.18 reduces to

$$\underline{E} = \frac{1}{2\pi} \int_S \frac{i\beta_o}{r} (\underline{n} \times \underline{E}) \times \underline{e}_r e^{-i\beta_o r} dS \qquad . \qquad (5.19)$$

The angle between the radius vectors to the point $(\sqrt{x_1^2 + z_1^2}, \theta_o, 0)$ in the aperture region and the point (r_o,θ,ϕ) in the far-zone, ψ in Fig. 5.2, is given by

$$\cos \psi = \sin \theta_o \sin \theta \cos \phi + \cos \theta_o \cos \theta \qquad .$$

For the thin slot $\Theta_o \doteq 0$ and therefore $\cos \psi$ reduces, approximately, to

$$\cos \psi \doteq \cos \Theta \quad .$$

Making the usual far-zone approximation for r in phase terms, i.e.,

$$r \doteq r_o - \sqrt{x_1^2 + z_1^2} \cos \psi$$

and since $\beta_o x_1 \ll 2\pi$, taking

$$r \doteq r_o - z_1 \cos \Theta \tag{5.20}$$

and noting that the tangential electric field is x-oriented and thus that $(\underline{n} \times \underline{e}_x) \times \underline{e}_r = -\underline{e}_\phi \sin \Theta$, one can rewrite Eq. 5.19 as follows

$$E_\phi(r_o,\Theta,\phi,\omega) = \frac{-i\beta_o \sin \Theta \, e^{-i\beta_o r_o}}{2\pi \, r_o} \int_{-b/2}^{b/2} \int_{-a/2}^{a/2} E_x(x,z,\omega) e^{i\beta_o z \cos \Theta} \, dx dz \ . \tag{5.21}$$

From Eq. 5.17 for E_x, the above equation can be expressed in terms of the source excitation. The result is

$$E_\phi(r_o,\Theta,\phi,\omega) = \frac{-i\beta_o \sin \Theta \, e^{-i\beta r_o}}{2\pi \, r_o} \int_{-a/2}^{a/2} \int_{-a/2}^{a/2} \int_{-b/2}^{b/2} E_s(x_o,z_o,\omega) \beta_p^2 G(z_1,z_o)$$

$$\times \, e^{i\beta_o z_1 \cos \Theta} \, dx_o dz_o dz_1 \tag{5.22}$$

in which $G(z_1,z_o)$ is given by Eq. 5.16.

Since $E_s(x,z,\omega)$ is a sample function of a random process, Eq. 5.22 cannot be integrated explicitly, and it is necessary to formulate the radiation pattern in terms of an average power flow per unit of space and frequency intervals. In the far-zone, the power radiated through a solid angle $d\Omega$ is given by Poynting's theorem as

$$p_{\Omega}(\theta,t)\,d\Omega = e_{\phi}(t)\; h_{\theta}(t)\; r_o^2\; d\Omega$$

$$p_{\Omega}(\theta,t)\,d\Omega = e_{\phi}^2(t)\; \frac{r_o^2\; d\Omega}{\eta_o} \tag{5.23}$$

where real variables are assumed for the electric field, e_{ϕ}, and the magnetic field, h_{θ}. Recast in the notation of spectral analysis, by analogy to Eqs. 4.3 and 4.4, Eq. 5.23 establishes the relationship, given below, between the spectral distribution of the radiated power and the spectral intensity of the electric field. Denote the average power radiated into the space-frequency interval $df\, d\Omega$ by $P_{f\Omega}\, d\Omega\, df$, then by Eq. 5.23, the relationship is

$$P_{f\Omega}\, df\; d\Omega = \frac{2r_o^2}{\eta_o}\, S_e\; df\; d\Omega \quad . \tag{5.24}$$

S_e is the two-sided spectral intensity of the electric field, and according to the convention used throughout, $P_{f\Omega}$ is a one-sided spectral distribution, i.e., the average radiated power, $\langle p_{\Omega}(\theta,t)\rangle$, is given by the following one-sided integration.

$$\langle p_{\Omega}(\theta,t)\rangle = \int_0^{\infty} P_{f\Omega}\, df \quad . \tag{5.25}$$

Now, S_e is formed from the expression for the radiation field, Eq. 5.22, and the resulting formula is substituted into Eq. 5.24 in order to obtain $P_{f\Omega}$. In computing S_e, the bra-ket average is taken with respect to the ensemble of sample functions E_s, hence it commutes with the integration taken over the aperture, and the following expression results for the average power flow/solid angle/frequency interval.

$$P_{f\Omega} = \frac{\beta_o^2 \sin^2\theta}{2\pi^2 \eta_o} \left\{ \int\!\!\int_{-a/2}^{a/2} \int\!\!\int_{-b/2}^{b/2} \left\langle \frac{E_s(x_o,z_o,\omega)E_s^*(x_1,z_1,\omega)}{2T} \right\rangle_{e_s} \right. \tag{5.26}$$

$$\left. \times \left[\int\!\!\int_{-a/2}^{a/2} \beta_p^2 G(z_2,z_o)\beta_p^{*2} G^*(z_3,z_1) e^{i\beta_o(z_2-z_3)\cos\theta} dz_2 dz_3 \right] dx_o dx_1 dz_o dz_1 \right\} .$$

In the notation of Sec. 3.2, the mixed correlation-function, spectral-density term appearing in Eq. 5.26 is symbolized by $RS_e(x_o-x_1,z_o-z_1,\omega)$ and the full definition is

$$RS_e(x_o-x_1,z_o-z_1,\omega) = \lim_{T\to\infty} \left\langle \frac{E_s(x_o,z_o,\omega)E_s^*(x_1,z_1,\omega)}{2T} \right\rangle_{e_s} . \tag{5.27}$$

And for convenience, the function $\Phi(z_o,\theta)$ is introduced by the following definition

$$\Phi(z_o,\theta) = \int_{-a/2}^{a/2} \beta_p^2 \, G(z_2,z_o) e^{i\beta_o z_2 \cos\theta} dz_2 \tag{5.28}$$

in which $G(z_2,z_o)$ is the characteristic function for the aperture. For the case at hand, this expression can be integrated directly. Substituting from Eq. 5.16, one obtains the following equation

$$\Phi(z_o,\theta) = \int_{-a/2}^{a/2} \frac{\beta_p^2}{2\beta_c} \left\{ \frac{\cos\beta_c(z_2+z_o) - \cos\beta_c(a-|z_2-z_o|)}{\sin\beta_c a} \right\} e^{i\beta_o z_2 \cos\theta} dz_2 .$$

This expression is integrated, and after considerable manipulation, the following form results

$$\Phi(z_o,\theta) = \frac{2\beta_p^2}{\sin \beta_c a\left[\beta_c^2 - (\beta_o \cos \theta)^2\right]}$$

$$\times \left\{ \sin \beta_c \frac{a}{2}\left[\cos\left(\beta_o \frac{a}{2} \cos \theta\right)\cos \beta_c z_o - \cos(\beta_o \cos \theta)\cos \beta_c \frac{a}{2}\right] \right.$$

$$\left. + i \cos \beta_c \frac{a}{2} \left[\sin\left(\beta_o \frac{a}{2} \cos \theta\right)\sin \beta_c z_o - \sin(\beta_o z_o \cos \theta)\sin \beta_c \frac{a}{2}\right] \right\} . \tag{5.29}$$

Now, Eq. 5.26 for the spectral intensity of power, $P_{f\Omega}$, is rewritten below using the shorter notation.

$$P_{f\Omega} = \frac{\beta_o^2 \sin^2\theta}{2\pi^2 \eta_o} \left\{ \int_{-a/2}^{a/2}\!\!\int \int_{-b/2}^{b/2}\!\!\int RS_e(x_o - x_1, z_o - z_1, \omega)\, \Phi(z_o,\theta)\Phi^*(z_1,\theta)\, dx_o\, dx_1\, dz_o\, dz_1 \right\} \tag{5.30}$$

The functions RS_e and Φ are given by Eqs. 5.27 and 5.29, respectively. From this form, the notational generalization to the case of an arbitrary aperture having a random source polarization is quite apparent. However, the explicit determination of the functions involved may become very difficult.

5.4 Radiation Pattern for the Delta-Correlated Source

The radiation pattern can now be computed for any case which is of interest, simply by the specification of the correlation function for the source, substitution into Eq. 5.30, and finally, integration. In this section, the delta-correlated source of Leontovich and Rytov is used (see Sec. 3.4).

It is assumed that the loss characteristics of the noise medium are such that only a thin outer layer contributes to the external noise field.

For a metal, this is an excellent approximation, and the reduction of Eq. 3.31 to the two-dimensional case gives Eq. 5.31 for the correlation function of the tangential noise field at the exterior surface of the noise source. (E_s in Fig. 5.1).

$$
\begin{aligned}
RR_e(x_o-x_1,z_o-z_1,\tau) &= \left\langle E_s(x_o,z_o,t)E_s^*(x_1,z_1,t-\tau)\right\rangle_{e_s} \\
RR_e(x_o-x_1,z_o-z_1,\tau) &= \frac{2\overline{\epsilon}}{\sigma\delta}\,\delta(x_o-x_1)\;\delta(z_o-z_1)\;\delta(\tau) \quad .
\end{aligned}
\tag{5.31}
$$

The characteristic equivalent depth associated with complete absorption of electromagnetic waves, i.e., the skin depth δ, appears in Eq. 5.31 consistent with the derivation in Sec. 3.4 in which the area, dA in Eq. 3.30, is interpreted as the effective conduction area. Likewise, for the case of a wire of radius "a" at high frequencies, the conductivity per unit length, σ_1 in Eq. 3.32 is given by $\sigma_1 = \sigma dA = \sigma\delta(2\pi a)$. For a plasma of high conductivity, an analogous absorption phenomenon takes place; and in this case too, the parameter δ is the characteristic absorption depth. Taking the Fourier transform of Eq. 5.31, by Eq. 3.13, leads to the mixed correlation-spectral density function given below.

$$
\begin{aligned}
RS_e(x_o-x_1,z_o-z_1,\omega) &= \int_{-\infty}^{\infty} RR_e\, e^{-i\omega\tau} d\tau \\
RS_e(x_o-x_1,z_o-z_1,\omega) &= \frac{2\overline{\epsilon}}{\sigma\delta}\,\delta(x_o-x_1)\;\delta(z_o-z_1) \quad .
\end{aligned}
\tag{5.32}
$$

Substitution of Eq. 5.32 into Eq. 5.30 and integration with respect to x_o, x_1, and z_1 give

$$P_{f\Omega} = \frac{\beta_o^2\,\bar{\epsilon}\,b\sin^2\theta}{\pi^2\,\eta_o\,\sigma\delta}\int_{-a/2}^{a/2}\Phi(z_o,\theta)\,\Phi^*(z_o,\theta)\,dz_o \quad . \qquad (5.33)$$

Equation 5.29 gives the function $\Phi(z_o,\theta)$, which results from the integration of the characteristic function weighted by the phase factor $e^{i\beta_o z\cos\theta}$. Substitution of this value into Eq. 5.33 and integration lead in a tedious, but straightforward, way to the intermediate form given in Eq. 5.34 below.

$$\begin{aligned}P_{f\Omega} = {} & \frac{\beta_o^2\,\bar{\epsilon}\,b}{\pi^2\,\eta_o\,\sigma\delta}\,\frac{4|\beta_p|^4\sin^2\theta}{|\sin\beta_c a|^2\,|\beta_c^2-(\beta_o\cos\theta)^2|^2}\Bigg\{a\left|\sin\beta_c\frac{a}{2}\cos\beta_c\frac{a}{2}\right|^2 \\ & + \frac{\sinh\alpha a}{2\alpha}\left[\left|\sin\beta_c\frac{a}{2}\right|^2\cos^2\!\left(\beta_o\frac{a}{2}\cos\theta\right)+\left|\cos\beta_c\frac{a}{2}\right|^2\sin^2\!\left(\beta_o\frac{a}{2}\cos\theta\right)\right] \\ & + \frac{\sinh\beta a}{2\beta}\left[\left|\sin\beta_c\frac{a}{2}\right|^2\cos^2\!\left(\beta_o\frac{a}{2}\cos\theta\right)-\left|\cos\beta_c\frac{a}{2}\right|^2\sin^2\!\left(\beta_o\frac{a}{2}\cos\theta\right)\right] \\ & + \mathrm{Re}\,\frac{\beta_c^*\sin\beta_c a}{\beta_c^{*2}-(\beta_o\cos\theta)^2}\left[\cos\beta_c^* a-\cos(\beta_o a\cos\theta)\right]\Bigg\} \quad . \qquad (5.34)\end{aligned}$$

The defining equations for the wave numbers, Eqs. 5.3, 5.4, and 5.5 are rewritten below,

$$i\beta_c = \alpha + i\beta = i\omega\sqrt{\mu\epsilon_c} \qquad \text{(complex)}$$

$$i\beta_p = \alpha_1 + i\beta_1 \qquad \text{(noise medium)}$$

$$\beta_o^2 = \omega^2\mu_o\,\epsilon_o \qquad \text{(free space)}$$

and it is restated that β_c is associated with lossy propagation along the thin slot (Fig. 5.1), β_o is the free-space wave number arising from Eq. 5.18, and β_p is the propagation factor in the noise medium defined in Eq. 5.2.

Equation 5.34 is not in a convenient form for computation. A more convenient form is found by introducing a $(4\beta_o)$ portion of the coefficient into the central bracket, replacing β_o/η_o by $\omega\epsilon_o$, eliminating β_c in favor of α, β, and β_p by α_1, β_1. Finally, after considerable manipulation, the following expression is obtained for the one-sided spectral intensity of power which is radiated by the thin incoherently illuminated aperture.

$$P_{f\Omega} = \frac{\omega\epsilon_o \bar{\epsilon}\, b}{\pi^2 \sigma \delta} \; \frac{2(\alpha_1^2+\beta_1^2)^2 \sin^2\theta}{\left[\cosh 2\alpha a - \cos 2\beta a\right]\left[(\beta^2-\beta_o^2\cos^2\theta-\alpha^2)^2+4\alpha^2\beta^2\right]}\, K$$

where K is defined by

$$\begin{aligned} K = \Bigg\{ & \beta_o a \left[\frac{\sinh \alpha a}{\alpha a}\left[\cosh \alpha a - \cos(\beta_o a \cos\theta)\cos \beta a\right] + \frac{1}{2}\cosh 2\alpha a - \frac{1}{2}\cos 2\beta a\right] \\ & + \frac{\beta_o \sin \beta a}{\beta}\left[-\cos \beta a + \cos(\beta_o a \cos\theta)\cosh \alpha a\right] \\ & + \frac{4\beta_o}{(\beta^2-\beta_o^2\cos^2\theta-\alpha^2)^2+4\alpha^2\beta^2}\Big[(\beta^3-\beta\beta_o^2\cos^2\theta+\alpha^2\beta)\sin \beta a\big[\cos \beta a \\ & \qquad - \cos(\beta_o a \cos\theta)\cosh \alpha a\big] \\ & -\alpha(\beta^2+\beta_o^2\cos^2\theta+\alpha^2)\sinh \alpha a \left[\cosh \alpha a - \cos(\beta_o a \cos\theta)\cos \beta a\right]\Big]\Bigg\} \; . \qquad (5.35) \end{aligned}$$

The above equation represents a first-order approximation to the radiation pattern for a thin slot which is excited incoherently both spatially and timewise. In the preceding analysis, the major approximation occurs in the determination of the aperture illumination by means of the principal-mode analysis, Sec. 5.2. This approximation is analogous to the traditional assumption of sinusoidal current distribution in the thin wire antenna. In the latter case, higher order approximations have been made;

and in isolated cases, exact solutions have been obtained; and there is extensive coverage in the literature concerning the amount of error which is introduced by the sinusoidal approximation. In general, it is found that the higher-order solutions are a necessity for an accurate determination of the input impedance; however, quite a good representation of the far-zone radiation pattern is obtained from the sinusoidal current distribution for conductor diameters less than $\lambda/10$ to $\lambda/100$. Extrapolating on these results, it is probable that Eq. 5.35 adequately represents the far-zone pattern when a comparable limit is placed on b, say, $b < \lambda/10$ to $\lambda/100$.

5.4.1 Radiation Pattern Examples for the Delta-Correlated Source.

The form of the radiation pattern is fixed if one specifies the slot length, the free-space wave number, and the complex wave number, i.e., the parameters a, β_o, and $\alpha + i\beta$ in Eq. 5.35. To establish the absolute level of the radiation, it is necessary to specify also the source temperature, the conductivity-skin depth product, and the slot width, i.e., the parameters $\overline{\epsilon}$, $\sigma\delta$, and b respectively. In this section selected examples are chosen in order to illustrate the effect of the various parameters. First, an expression is derived for the radiation pattern when the wave numbers are equal, i.e., $\beta = \beta_o$. Graphs are presented for later comparison to experimental data in Sec. 5.7. Secondly, an expression is derived for the case $\beta = \beta_o$ with $\alpha = 0$ too. This is compared to the result of Levin and Rytov for a thin wire. Finally, the indeterminate form of Eq. 5.35 as $\Theta \to 0$ is examined; and an asymptotic form, applicable when $\alpha = 0$, $\beta = \beta_o$, and $\sin\Theta \doteq \Theta$, is derived.

Case I. Equal Wave Numbers with Attenuation ($\beta = \beta_o$, $\alpha \neq 0$).

In Eq. 5.35, set $\beta = \beta_o$ and rearrange slightly. The following result, Eq. 5.36, is a simpler form for the thermal radiation pattern under the assumption that the phase velocity along the thin slot is equal to the phase velocity in free space.

$$P_{f\Omega} = \frac{\omega\epsilon_o \bar{\epsilon} b\,(\alpha_1^2 + \beta_1^2)^2}{\pi^2\ \sigma\delta\ \beta_o^4}\ \frac{2\sin^2\theta}{[\cosh 2\alpha a - \cos 2\beta_o a][(\sin^2\theta - \Delta^2)^2 + 4\Delta^2]}\ K_o \tag{5.36}$$

where K_o is defined by

$$\begin{aligned} K_o = \Bigg\{ & \beta_o a\left[\frac{\sinh\alpha a}{\alpha a}[\cosh\alpha a - \cos(\beta_o a\cos\theta)\cos\beta_o a] + \tfrac{1}{2}\cosh 2\alpha a - \tfrac{1}{2}\cos 2\beta_o a\right] \\ & + \sin\beta_o a\,[-\cos\beta_o a + \cos(\beta_o a\cos\theta)\cosh\alpha a] \quad + \\ & \frac{4}{(\sin^2\theta - \Delta^2)^2 + 4\Delta^2}\Big[\sin^2\theta + \Delta^2)\sin\beta_o a[\cos\beta_o a - \cos(\beta_o a\cos\theta)\cosh\alpha a] \\ & - \Delta(1 + \cos^2\theta + \Delta^2)\sinh\alpha a[\cosh\alpha a - \cos(\beta_o a\cos\theta)\cos\beta_o a]\Big]\Bigg\} \end{aligned}$$

and Δ is defined by $\Delta = \alpha/\beta$.

Thermal radiation patterns for several different cases are plotted in Figs. 5.3 through 5.6. In each graph $P_{f\Omega}$, from Eq. 5.36, is plotted versus the angle from the normal, $\pi/2 - \theta$, for values of the loss factor Δ which represent attenuations of 1, 3, 5, and 20 db/wavelength. In these graphs, the ordinate is normalized to $[\omega\epsilon_o\bar{\epsilon}b(\alpha_1^2 + \beta_1^2)^2/\pi^2\sigma\delta\beta_o^4]$. Figs. 5.3, 5.4, 5.5, and 5.6 correspond to $\beta a/\pi$ = 7.3, 7.5, 9.3, and 9.5, respectively. The appropriate values of Δ, see Table 5.1, are determined as follows. For propagation along the z-axis the field

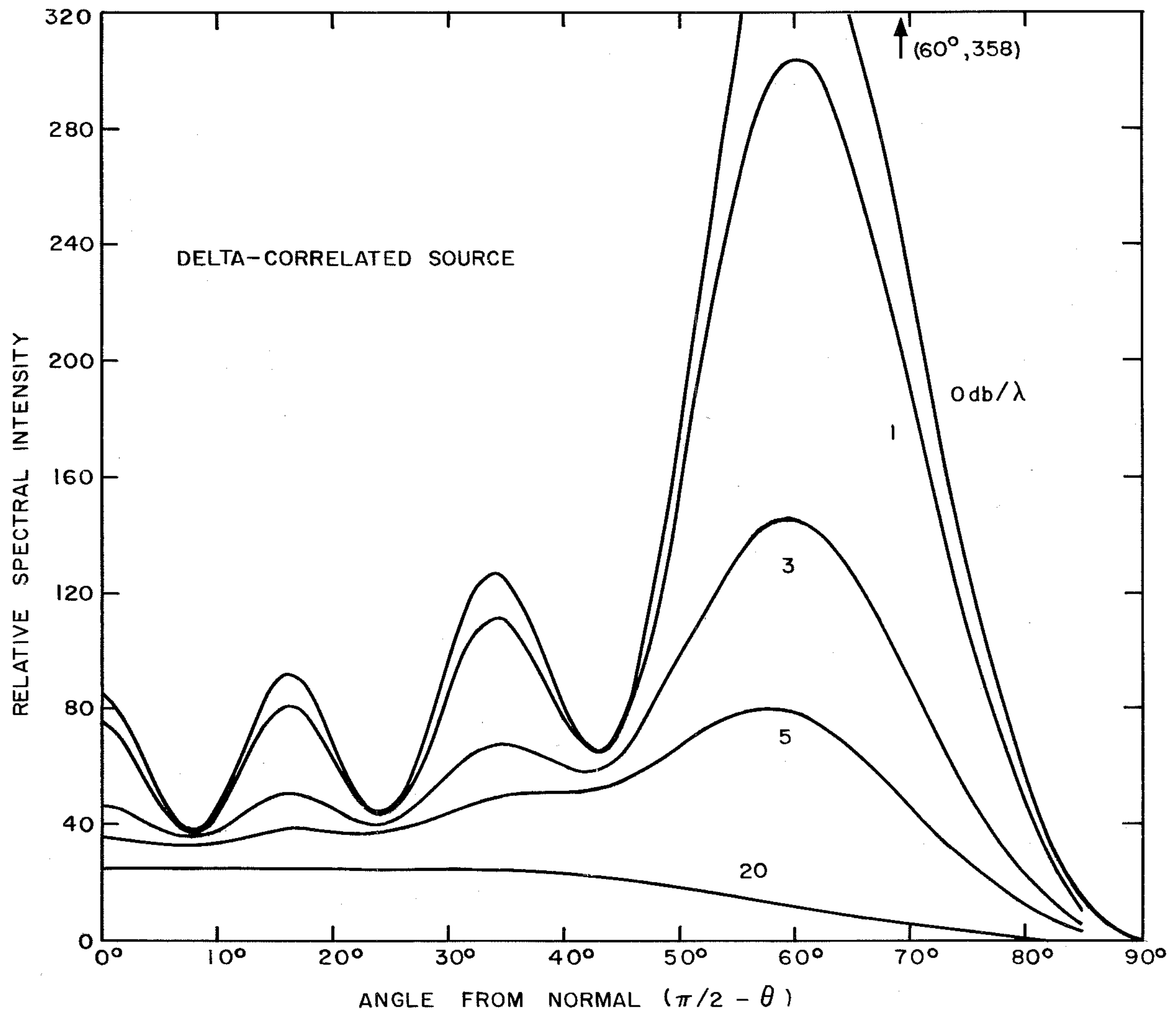

Fig. 5.3. Thermal radiation pattern of thin slot
(Plot of Eq. 5.36 with $\beta_o a = 7.3\pi$)

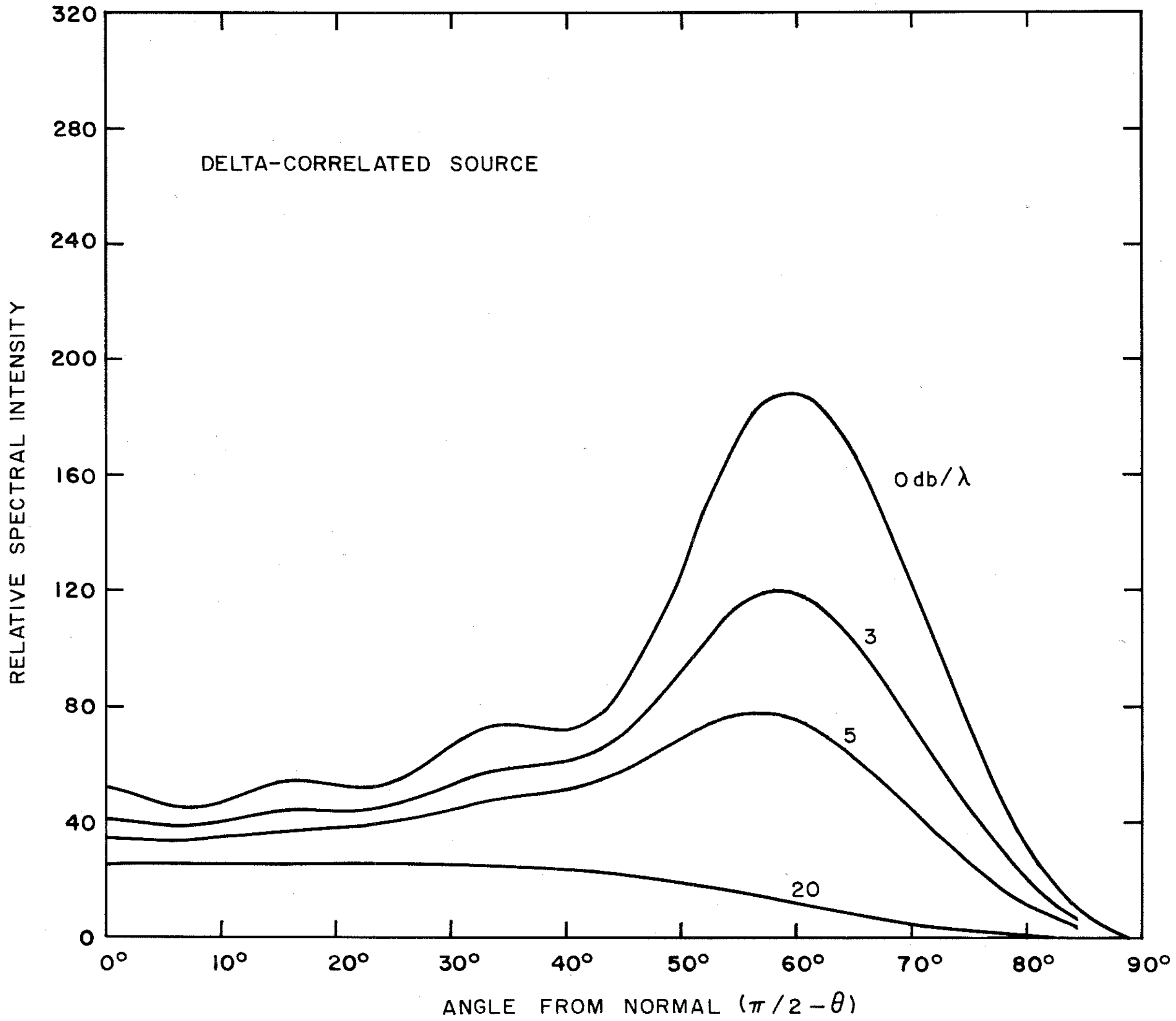

Fig. 5.4. Thermal radiation pattern of thin slot (Plot of Eq. 5.36 with $\beta_o a = 7.5\pi$)

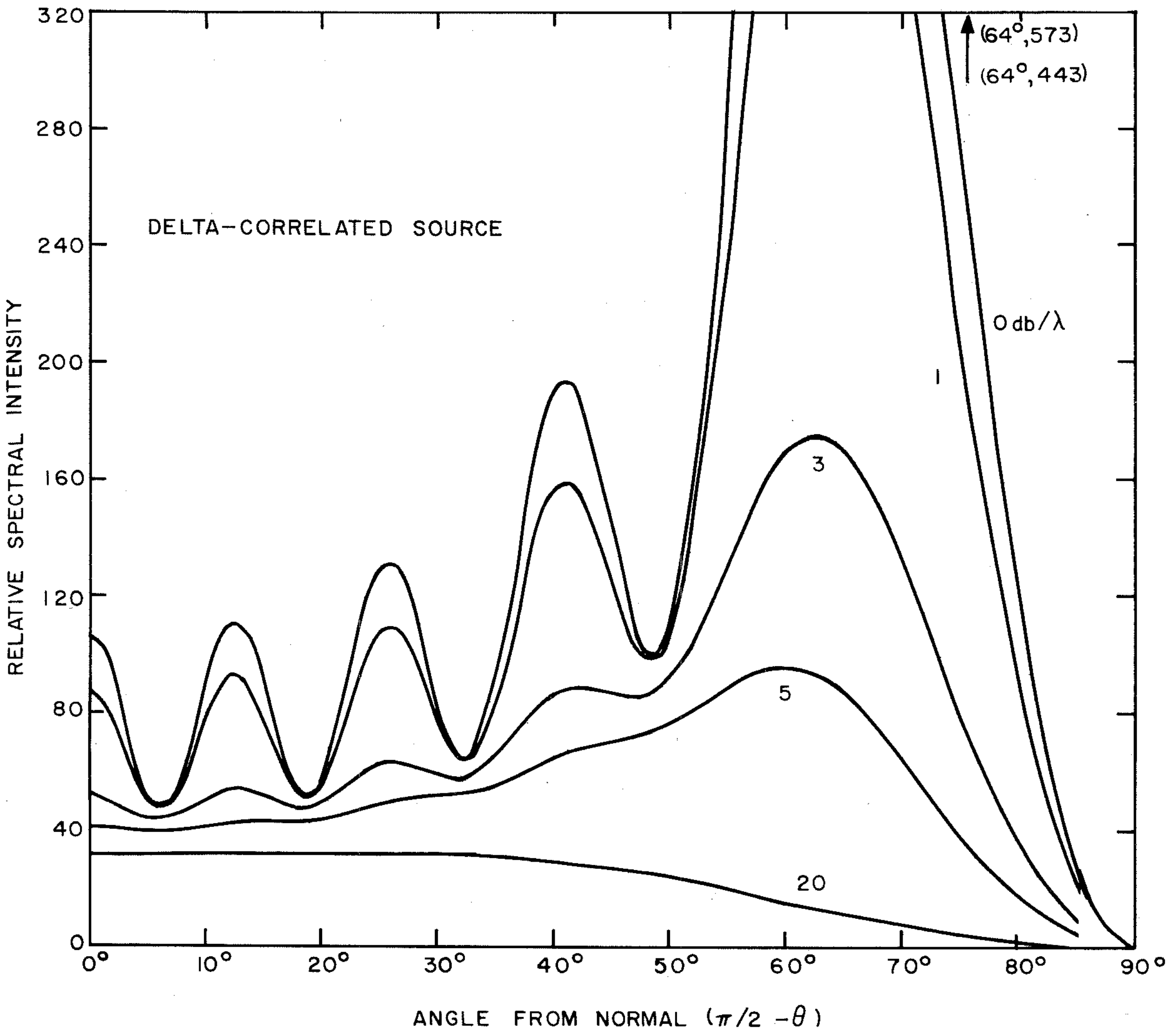

Fig. 5.5. Thermal radiation pattern of thin slot (Plot of Eq. 5.36 with $\beta_o a = 9.30\pi$)

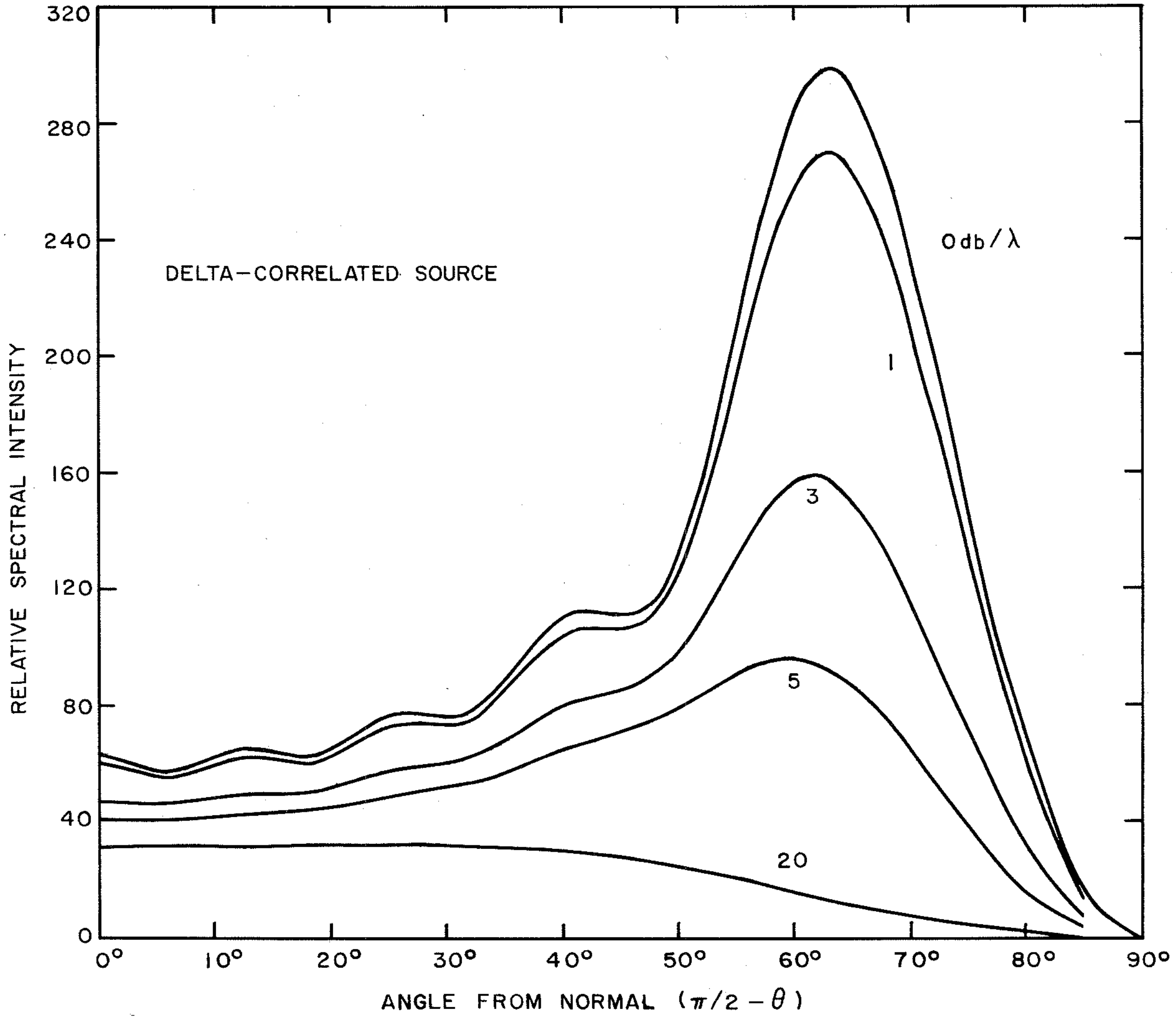

Fig. 5.6. Thermal radiation pattern of thin slot (Plot of Eq. 5.36 with $\beta_o a = 9.50\pi$)

vectors attenuate as $e^{-\alpha z}$; hence, in one wavelength the fractional attenuation is $e^{-2\pi\Delta}$; and, therefore, the attenuation in decibels per wavelength, $|db|_\lambda$, defined by $|db|_\lambda = 20 \log |E(z)/E(z+\lambda)|$, is related to Δ by the equation

$$\Delta = \frac{|db|_\lambda}{40\pi} \ln 10 \quad .$$

Table 5.1

VALUES OF LOSS FACTOR, Δ

ATTENUATION (decibels/wavelength)	1	3	5	20
LOSS FACTOR ($\Delta = \alpha/\beta$)	0.01832	0.05497	0.09162	0.3665

Two interesting features of these graphs are noted in this paragraph. First, the spatial distribution of radiant energy is distinctly non-Lambertian, with a pronounced maxima in the radiated power at angles which are quite far from the $\theta = \pi/2$ direction. Secondly, the form of the radiation pattern changes considerably as the loss factor increases. It is particularly interesting to note that the direction of the change is such that the relative spatial ripple decreases as the attenuation is increased. This is in accord with the physical argument presented in Sec. 3.5, where it is reasoned that the degree of correlation in the antenna currents, hence the amount of ripple in the radiation pattern, should decrease as the resistivity of the conductor is increased.

Case 2. Equal Wave Numbers. Loss Free. $(\beta = \beta_0, \alpha = 0)$.

For the equal phase velocity case in which there is no propagation loss along the slot, the thermal radiation pattern is obtained by placing

$\beta = \beta_o$ and $\alpha = 0$ in Eq. 5.35 or equivalently by setting $\alpha = \Delta = 0$ in Eq. 5.36. Evaluating the indeterminate form and making trigonometric simplifications, one obtains the following result.

$$P_{f\Omega} = \frac{\omega\epsilon_o\bar{\epsilon}\, b(\alpha_1^2 + \beta_1^2)^2}{\pi^2\ \sigma\delta\ \beta_o^4}\ \frac{K_{oo}}{\left[\sin\beta_o a \sin\theta\right]^2} \tag{5.37}$$

where K_{oo} is defined by

$$K_{oo} = \beta_o a\left[1 + \sin^2\beta_o a - \cos\beta_o a \cos(\beta_o a \cos\theta)\right]$$
$$+ \sin\beta_o a\left[\frac{4}{\sin^2\theta} - 1\right]\left[\cos\beta_o a - \cos(\beta_o a\cos\theta)\right] \quad .$$

Thermal radiation patterns are plotted for Eq. 5.37, too. These are curves labeled 0.0 db/λ and plotted for $\beta_o a/\pi = 7.3$, 7.5, 9.3, and 9.5 in Figs. 5.3, 5.4, 5.5, and 5.6 respectively. The maximum values for the cases $\beta_o a/\pi = 7.3$ and 9.3 are finite although they are outside of the range of the graphs shown. Additional patterns for $\beta_o a/\pi = 2.5$, 4.5, 6.5 and 8.5 are plotted in Fig. 5.7.

In terms of the spectral intensity or the Poynting's vector, it can be demonstrated by an application of Babinet's principle that the radiation pattern for the thin slot and the thin linear antenna are the same (24). Thus, it is to be expected that the spatial variation in Eq. 5.37 for the thin slot agrees with that in the formula derived by Levin and Rytov for the thin wire (8). Indeed, a comparison shows that they are in agreement, if allowance is made for a typographical error which has crept into the final expression for the radiation pattern in the paper of Levin and Rytov. At this point, it is pertinent to note that while the spatial variations are in agreement, no

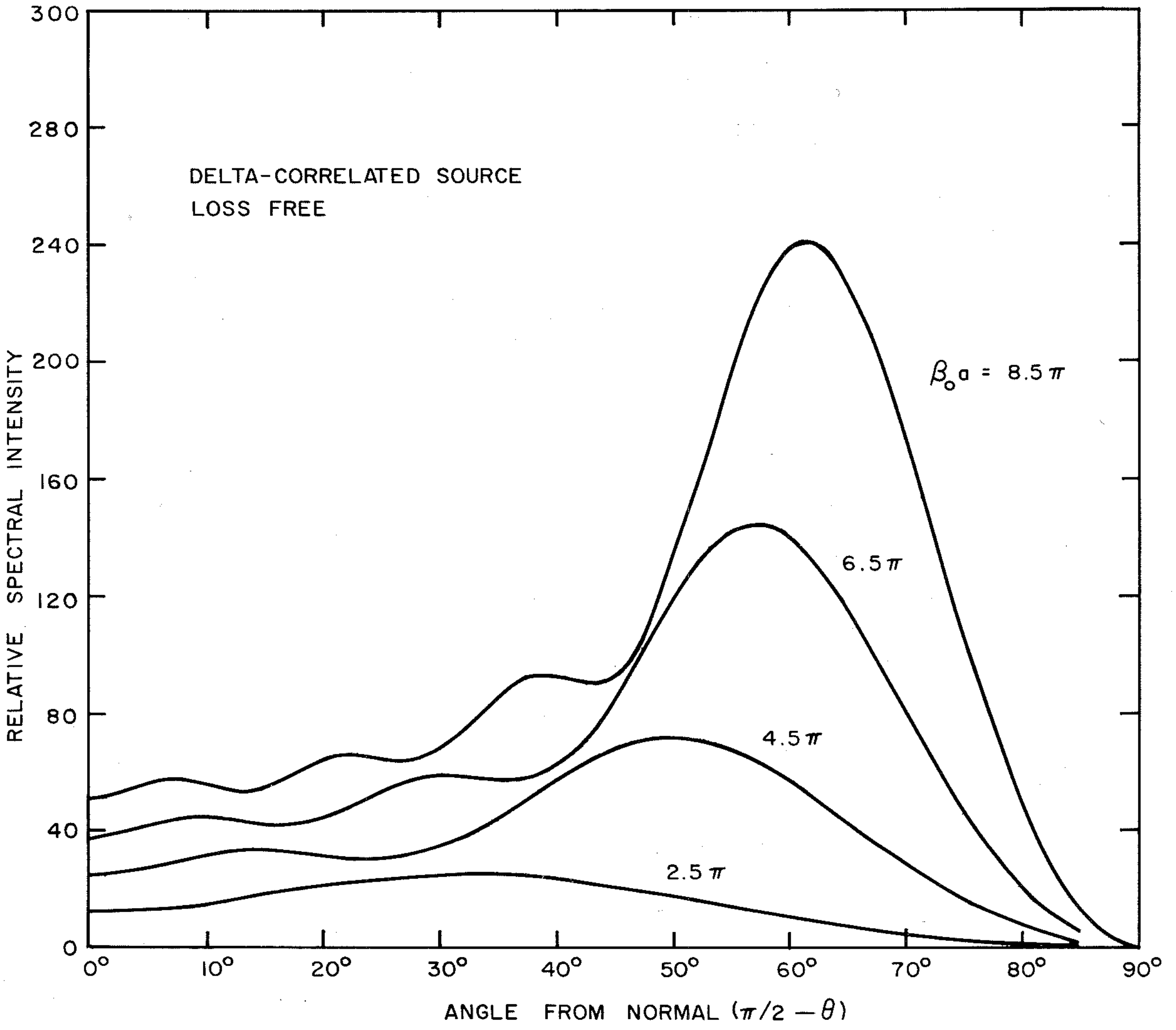

Fig. 5.7 Thermal radiation pattern of thin slot (Plot of Eq. 5.37)

attempt is made to compare coefficients. The reason for this is that in the approximate analysis in Sec. 5.2, it is assumed that the entire slot width is uniformly excited (along Δy in Fig. 5.2). This is not the case, and hence the coefficient in the thin slot analysis is probably not quantitatively accurate.

Case III. Asymptotic Form for Small Angles.

Consider Eq. 5.37 for the loss-free case as the angle θ goes to zero. From first principles, it is known that the intensity of the radiation must go to zero, too. However, a direct substitution of the $\theta = 0$ value leads to an indeterminate form; and, furthermore, computations of $P_{f\Omega}$ for small values of θ lead to the inaccuracies which are usually associated with numerical answers which result as small differences between large numbers. From Eq. 5.37, the angular variation, $K_{oo}/\sin^2\theta$, is given by

$$\frac{K_{oo}}{\sin^2\theta} = \frac{1}{\sin^4\theta}\left\{\beta_o a \sin^2\theta \left[1 + \sin^2\beta_o a - \cos\beta_o a \cos(\beta_o a \cos\theta)\right] + \sin\beta_o a \left[4 - \sin^2\theta\right]\left[\cos\beta_o a - \cos(\beta_o a\cos\theta)\right]\right\} . \qquad (5.38)$$

A convenient form for small values of θ is obtained by separately expanding the numerator and the denominator as power series in θ. Terms of order θ^6 and θ^4 must be carried in the numerator and denominator, respectively. In this manner, Eq. 5.38 can be reduced to

$$\frac{K_{oo}}{\sin^2\theta} \doteq \theta^2\left[(\beta_o a)^3\left(\frac{\cos^2\beta_o a}{8} + \frac{\sin^2\beta_o a}{12}\right) - \frac{23}{120}(\beta_o a)\sin^2\beta_o a\right]$$

and substituting into Eq. 5.37, one obtains the following expression for the thermal radiation pattern at small values of θ.

$$P_{f\Omega} = \frac{\omega \epsilon_o \bar{\epsilon} b\, (\alpha_1^2 + \beta_1^2)^2}{\pi^2\, \sigma\delta\, \beta_o^4} \left[(\beta_o a)^3 \left(\frac{\cot^2 \beta_o a}{8} + \frac{1}{12}\right) - \frac{23}{120}(\beta_o a) \right] \theta^2 \quad . \qquad (5.39)$$

5.5 Radiation Pattern for the Partially-Correlated Source

In this section the thermal radiation pattern is computed for the partially-correlated source. In general, if the slot, Fig. 5.1, is illuminated remotely, i.e., the noise source is a few wavelengths from the aperture rather than directly adjacent, then, the source excitation field, $E_s(x,z,\omega)$, will be partially correlated. The degree of correlation will be dependent on the geometry and the propagation characteristics in the intervening medium. Rather than delving into special cases, it is more convenient for our purposes to generalize the concept of a random noise source. Consider a hypothetical noise medium which has the following properties. First, the terminal characteristics of this medium are those specified by Nyquist's theorem (see Sec. 3.3). Secondly, the distributed noise field is exponentially-correlated spatially, and delta-correlated timewise. Thus analytically, the correlation function assumed for this generalized noise medium is given by

$$RR_e(x_o - x_1, z_o - z_1, \tau) = \frac{2\bar{\epsilon}}{\sigma\delta} N_1 N_2 \delta(\tau)\, e^{-|x_o - x_1|/u_o}\, e^{-|z_o - z_1|/v_o} \qquad (5.40)$$

where u_o and v_o are the correlation lengths in the x and y directions respectively, and N_1 and N_2 are the normalization constants which are chosen to make the terminal characteristics of the medium conform to Nyquist's theorem. Taking Eq. 5.40 as the correlation function for the noise excitation field, $E_s(x,z,\omega)$, one can determine N_1 and

N_2 from Eq. 3.26 in the following manner. For the effective source sheet which has dimensions b, δ, a along the x, y, z axes respectively, where from Fig. 5.1 the $\underline{e}_x$ component of the electric field source is appropriate, the terminal voltage averaged over the δ by a cross-section, $v(t)$, is given by

$$v(t) = \frac{1}{a} \int_{-a/2}^{a/2} \int_{-b/2}^{b/2} e_s(x,z,t)\, dx\, dz \quad . \tag{5.41}$$

Forming the product $v(t)\, v^*(t-\tau)$,

$$v(t)v^*(t-\tau) = \frac{1}{a^2} \int_{-a/2}^{a/2}\int \int_{-b/2}^{b/2}\int e_s(x_o,z_o,t)e_s^*(x_1,z_1,t-\tau)dx_o dx_1 dz_o dz_1 \tag{5.42}$$

and taking the ensemble average over the sample functions, e_s, one obtains

$$\begin{aligned} R_v(\tau) &= \left\langle v(t)\ v^*(t-\tau)\right\rangle_e \\ R_v(\tau) &= \frac{1}{a^2} \int_{-a/2}^{a/2}\int \int_{-b/2}^{b/2}\int RR_e(x_o-x_1,z_o-z_1,\tau)dx_o dx_1 dz_o dz_1 \quad . \end{aligned} \tag{5.43}$$

From Eq. 3.25, the correlation function for the terminal voltage of the resistor of length b and cross-section of δ by a is given by

$$\begin{aligned} R_v(\tau) &= 2\overline{\epsilon}\ R\ \delta(\tau) \\ R_v(\tau) &= \frac{2\overline{\epsilon}\ b\ \delta(\tau)}{\sigma(\delta a)} \quad . \end{aligned} \tag{5.44}$$

Eq. 5.43 is rewritten, below, after the substitution from Eq. 5.40 for

RR_e and from Eq. 5.44 for R_v.

$$\frac{2\bar{\epsilon} b\,\delta(\tau)}{\sigma\,\delta a} = \frac{2\bar{\epsilon}\,\delta(\tau)}{\sigma\,\delta\,a^2} N_1 N_2 \iint_{-a/2}^{a/2} \iint_{-b/2}^{b/2} e^{-\frac{|x_o-x_1|}{u_o}-\frac{|z_o-z_1|}{v_o}} dx_o dx_1 dz_o dz_1 \, . \tag{5.45}$$

Carrying out the indicated integrations and rearranging slightly, one obtains the following result for the normalization constants $N_1 \cdot N_2$

$$N_1 \cdot N_2 = \frac{1}{2u_o\left[1-\frac{u_o}{b}\left(1-e^{-b/u_o}\right)\right]} \cdot \frac{1}{2v_o\left[1-\frac{v_o}{a}\left(1-e^{-a/v_o}\right)\right]} \, . \tag{5.46}$$

Equation 5.46 specifies the normalization constants for the exponential correlation function in Eq. 5.40. The associated mixed correlation-spectral density function is obtained by taking the Fourier transform of Eq. 5.40 with respect to the variable τ. The result is

$$\begin{aligned} RS_e(x_o-x_1, z_o-z_1, \omega) &= \int_{-\infty}^{\infty} RR_e\, e^{-i\omega\tau} d\tau \\ RS_e(x_o-x_1, z_o-z_1, \omega) &= \frac{2\bar{\epsilon}}{\sigma\delta} N_1 N_2\, e^{-\frac{|x_o-x_1|}{u_o}-\frac{|z_o-z_1|}{v_o}} \, . \end{aligned} \tag{5.47}$$

The thermal radiation pattern for the partially-correlated source can now be computed in a straightforward manner. The function RS_e, Eq. 5.47, is substituted into the general formula for the radiation intensity, Eq. 5.30, giving

$$P_{f\Omega} = \frac{\beta_o^2 \bar{\epsilon} \sin^2\theta}{\pi^2 \eta_o \sigma\delta} N_1 N_2$$

$$\times \int_{-a/2}^{a/2}\int_{-a/2}^{a/2}\int_{-b/2}^{b/2}\int_{-b/2}^{b/2} \Phi(z_o,\theta)\,\Phi^*(z_1,\theta)\, e^{-\frac{|x_o-x_1|}{u_o} - \frac{|z_o-z_1|}{v_o}}\, dx_o dx_1 dz_o dz_1 \tag{5.48}$$

where Φ is defined by Eq. 5.29. Integrating Eq. 5.48 with respect to the variables x_o and x_1 and substituting from Eq. 5.46 give

$$P_{f\Omega} = \frac{\beta_o^2 \bar{\epsilon}\, b \sin^2\theta}{\pi^2 \eta_o\, \sigma\delta} N_2 \int_{-a/2}^{a/2}\int_{-a/2}^{a/2} \Phi(z_o,\theta)\Phi^*(z_1,\theta)\, e^{-\frac{|z_o-z_1|}{v_o}}\, dz_o dz_1 \,. \tag{5.49}$$

The integrations with respect to z_o and z_1 are performed by separating the interval of integration as follows:

$$I(\theta) = \int_{-a/2}^{a/2}\int_{-a/2}^{a/2} \Phi(z_o,\theta)\Phi^*(z_1,\theta)\, e^{-\frac{|z_o-z_1|}{v_o}}\, dz_o dz_1$$

$$I(\theta) = \int_{-a/2}^{a/2} dz_1\, \Phi^*(z_1,\theta) e^{-z_1/v_o} \int_{-a/2}^{z_1} dz_o \Phi(z_o,\theta) e^{z_o/v_o}$$
$$+ \int_{-a/2}^{a/2} dz_1 \Phi^*(z_1,\theta) e^{z_1/v_o} \int_{z_1}^{a/2} dz_o \Phi(z_o,\theta) e^{-z_o/v_o} \,. \tag{5.50}$$

The general expression for $\Phi(z_o,\theta)$ is given by Eq. 5.29. In order to simplify the notation and the later computations, it is assumed that the propagation along the slot is lossless, i.e., $\beta_c \rightarrow \beta_o$; and Eq. 5.29 then reduces to

$$\Phi(z_o\Theta) = \frac{2\beta_p^2}{\beta^2 \sin\beta a \sin^2\Theta}\Bigg\{\sin\beta\frac{a}{2}\left[\cos\left(\beta\frac{a}{2}\cos\Theta\right)\cos\beta z_o - \cos(\beta z_o\cos\Theta)\cos\beta\frac{a}{2}\right]$$

$$+ i\cos\beta\frac{a}{2}\left[\sin\left(\beta\frac{a}{2}\cos\Theta\right)\sin\beta z_o - \sin(\beta z_o\cos\Theta)\sin\beta\frac{a}{2}\right]\Bigg\} \qquad (5.51)$$

where the sub-zero notation for the wave number is omitted, i.e., for notational convenience β replaces β_o. Equation 5.50 is integrated using $\Phi(z_o,\Theta)$ from Eq. 5.51, and the result is substituted into Eq. 5.49 to form $P_{f\Omega}$. After a long computation, the following intermediate form is obtained.

$$P_{f\Omega} = \frac{\omega\epsilon_o\bar{\epsilon}\, b\,(\alpha_1^2+\beta_1^2)^2}{\pi^2 \quad \sigma\delta\,\beta^4} \quad \frac{1}{[\sin\beta a \sin\Theta]^2} \quad G(\Theta,\beta a,v_o) \quad . \qquad (5.52)$$

The function G is given by

$$G = \beta a[2v_oN_2][B(1-\cos(\beta a\cos\Theta)\cos\beta a) + A\sin^2\beta a]$$

$$+ \sin\beta a[2v_oN_2]\left[\frac{2(A+B)}{\sin^2\Theta} - B\right][\cos\beta a - \cos(\beta a\cos\Theta)]$$

$$+ 16\beta N_2 v_o^2 e^{-a/2v_o}\left[F_1F_3\sin^2\beta\frac{a}{2} + F_2F_4\cos^2\beta\frac{a}{2}\right] \quad . \qquad (5.53)$$

The remaining symbols are defined below.

$$A = \frac{1}{1+(\beta v_o)^2\cos^2\Theta}$$

$$B = \frac{1}{1+(\beta v_o)^2}$$

$$N_2 = \frac{1}{2v_o\left[1 - \frac{v_o}{a}\left(1-e^{-a/v_o}\right)\right]}$$

$$F_1 = (A-B)\cos\beta\frac{a}{2}\cos(\beta\frac{a}{2}\cos\Theta)+\beta v_0 B\sin\beta\frac{a}{2}\cos(\beta\frac{a}{2}\cos\Theta)$$
$$-\beta v_0 A\cos\Theta\cos\beta\frac{a}{2}\sin(\beta\frac{a}{2}\cos\Theta)$$

$$F_2 = (A-B)\sin\beta\frac{a}{2}\sin(\beta\frac{a}{2}\cos\Theta)-\beta v_0 B\cos\beta\frac{a}{2}\sin(\beta\frac{a}{2}\cos\Theta)$$
$$+\beta v_0 A\cos\Theta\sin\beta\frac{a}{2}\cos(\beta\frac{a}{2}\cos\Theta)$$

$$F_3 = -(A-B)\cos\beta\frac{a}{2}\cos(\beta\frac{a}{2}\cos\Theta)\sinh\frac{a}{2v_0}+\beta v_0 B\sin\beta\frac{a}{2}\cos(\beta\frac{a}{2}\cos\Theta)\cosh\frac{a}{2v_0}$$
$$-\beta v_0 A\cos\Theta\cos\beta\frac{a}{2}\sin(\beta\frac{a}{2}\cos\Theta)\cosh\frac{a}{2v_0}$$

$$F_4 = -(A-B)\sin\beta\frac{a}{2}\sin(\beta\frac{a}{2}\cos\Theta)\cosh\frac{a}{2v_0}-\beta v_0 B\cos\beta\frac{a}{2}\sin(\beta\frac{a}{2}\cos\Theta)\sinh\frac{a}{2v_0}$$
$$+\beta v_0 A\cos\Theta\sin\beta\frac{a}{2}\cos(\beta\frac{a}{2}\cos\Theta)\sinh\frac{a}{2v_0}\,.$$

The expression for G, Eq. 5.53, is exact, but it is unnecessarily complicated if the correlation length v_0 is fairly small. For example, if the ratio v_0/a is small, then the third line of G is much smaller than the first two, and it can be approximated in the following manner. Provided that $v_0/a < 3$, an error of less than 5% is made by the following approximation:

$$\sinh\frac{a}{2v_0} \doteq \cosh\frac{a}{2v_0} \doteq \frac{1}{2}e^{a/2v_0}\quad. \tag{5.54}$$

Substituting Eq. 5.54 into the third line of G and dropping terms which have the exponential coefficient e^{-a/v_0}, one obtains the following approximate form

$$G_3 \doteq \beta v_0\left\{2v_0N_2\right\}\left\{-(A-B)^2\sin^2\beta\frac{a}{2}+(\beta v_0)^2B^2\left[\frac{3}{2}+\frac{1}{2}\cos 2\beta a-2\cos\beta a\cos(\beta a\cos\Theta)\right]\right.$$
$$\left.-2(\beta v_0)^2AB\cos\Theta\sin\beta a\sin(\beta a\cos\Theta)+(\beta v_0)^2A^2\cos^2\Theta\sin^2\beta a\right\}\quad. \tag{5.55}$$

This approximate form for the third line of G considerably simplifies computations since the cumbersome F factors are completely eliminated. In fact, it is clear from Eq. 5.55 that if $\beta v_o \ll 1$, in addition to the prior assumption that $v_o/a < 3$, then the third line of G is completely negligible, i.e., $G_3 \doteq 0$.

Thermal radiation patterns are plotted for $\beta a/\pi = 7.3, 7.5, 9.3,$ and 9.5 in Figs. 5.8, 5.9, 5.10, and 5.11, respectively. In each graph $P_{f\Omega}$ normalized to $[\omega\epsilon_o\bar{\epsilon}\, b(\alpha_1^2+\beta_1^2)^2/\pi^2\, \sigma\delta\beta^4]$ is plotted versus the angle from the normal, $\pi/2-\Theta$, for the following values of the correlation length βv_o : $0, 0.30\pi, 0.60\pi$, and 1.0π. The Eq. 5.55 approximation is used for the third line of G in Eq. 5.53. In these graphs, the ratio of the maximum response to the response in the $\Theta = \pi/2$ or normal direction decreases as the correlation length increases. Interestingly, the relative ripple in the fine structure of these patterns does not change markedly as the correlation length changes. In fact, percentage-wise this ripple increases gradually as the correlation length increases. Ultimately, as the excitation becomes fully coherent, this ripple must increase to 100%, for it is known that complete nulls will be obtained (Sec. 5.6). Comparing the pattern variation as a function of the correlation length, Figs. 5.8 through 5.11, to the pattern variation as a function of the loss factor, Figs. 5.3 through 5.6, it is seen--as should be expected--that quite different changes in form occur.

In Eq. 5.47, as u_o, v_o go to zero, the limiting value of the correlation function is given by Eq. 5.32, i.e., since

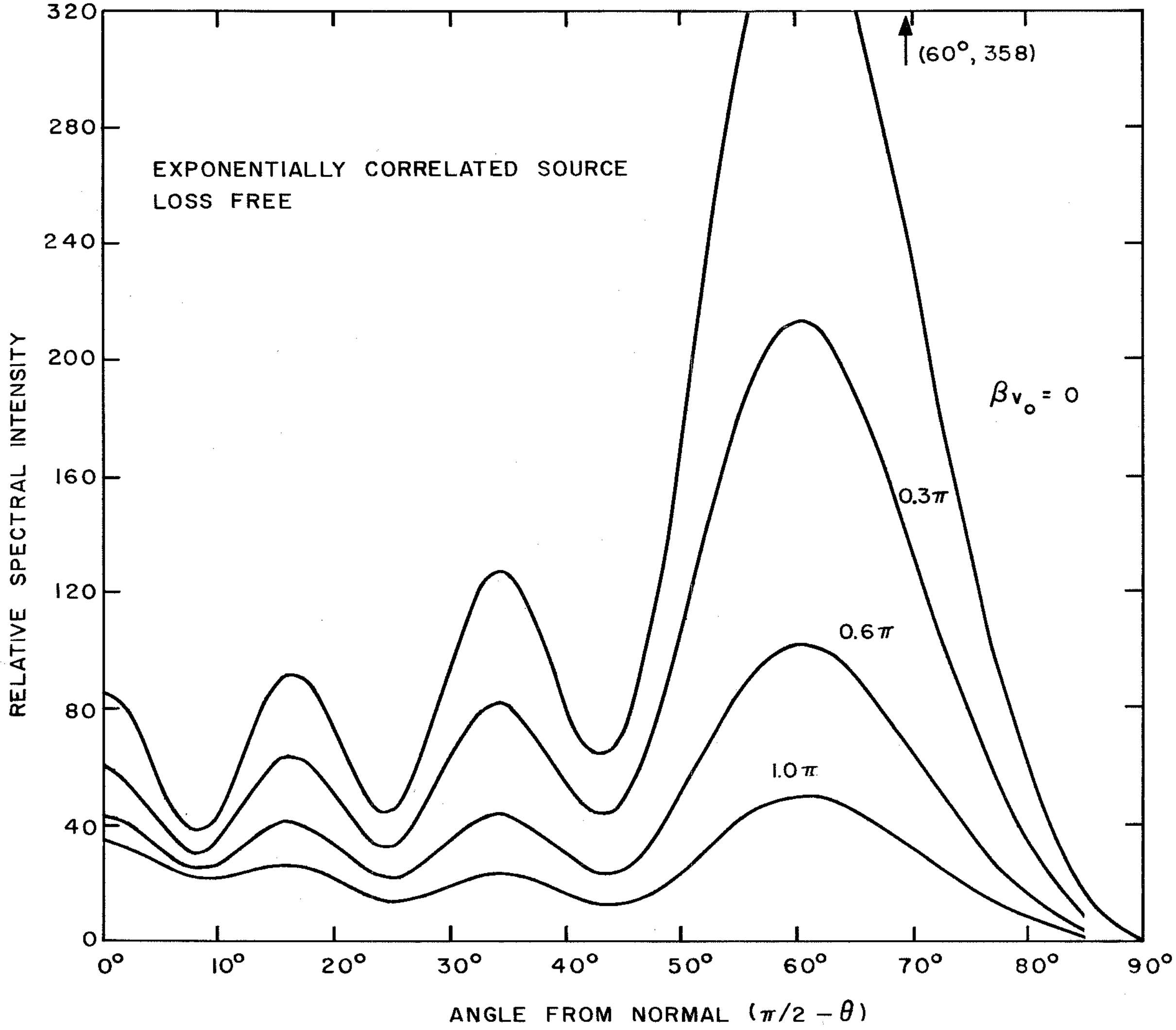

Fig. 5.8 Thermal radiation pattern of thin slot
(Plot of Eqs. 5.52, 53, 55 with $\beta_o a = 7.3\pi$)

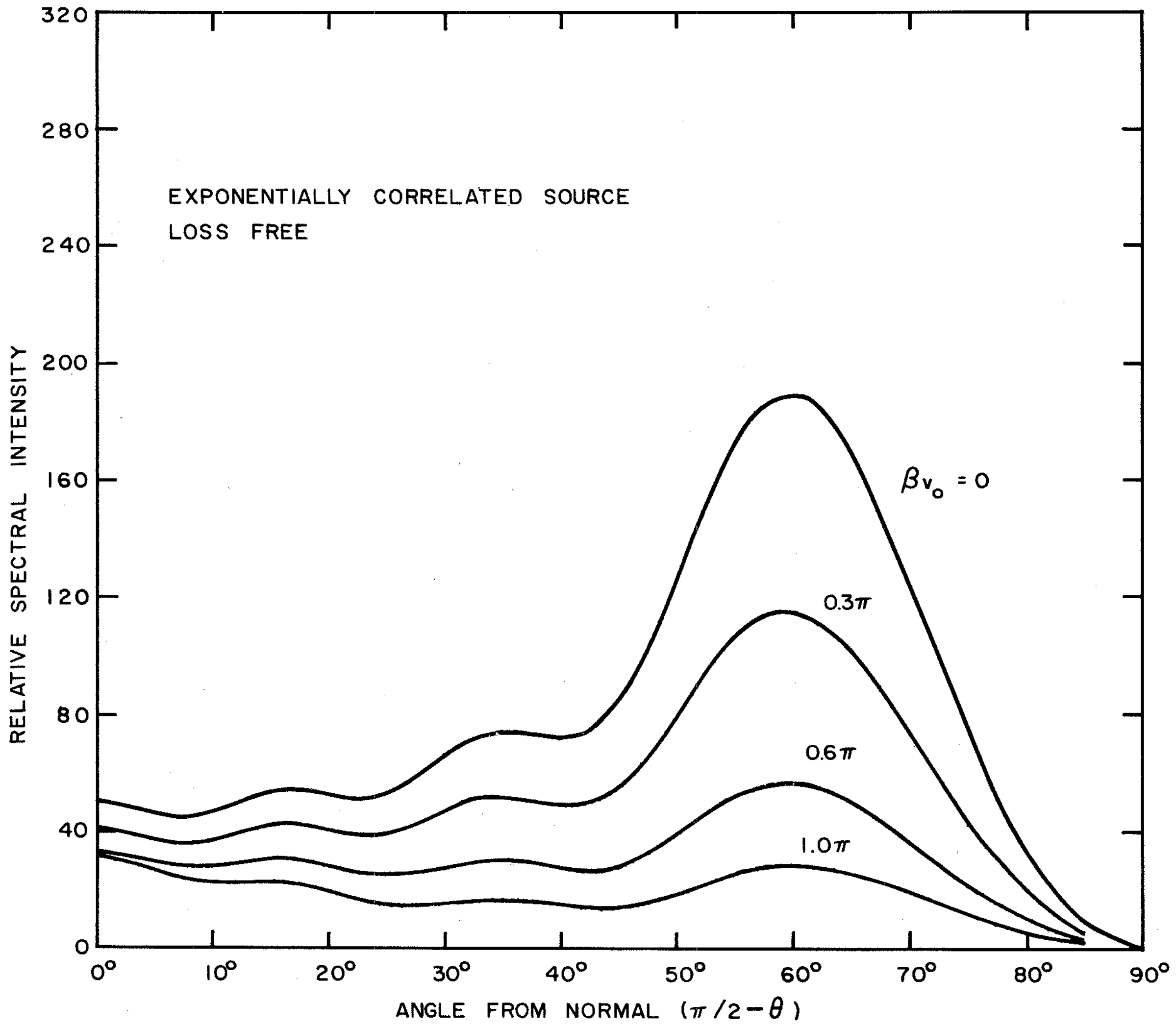

Fig. 5.9. Thermal radiation pattern of thin slot
(Plot of Eqs. 5.52, 53, 55 with $\beta_o a = 7.5\pi$)

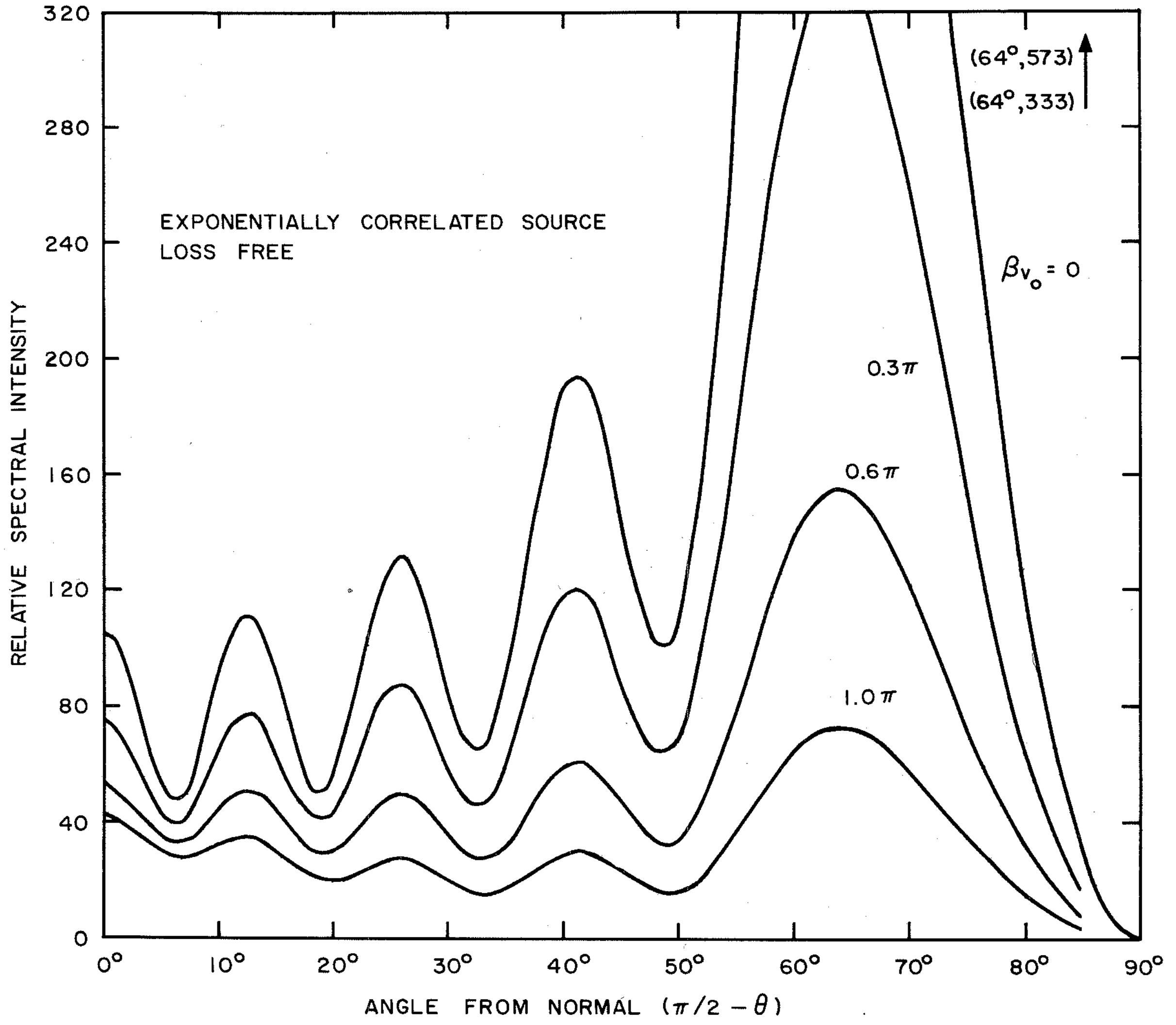

Fig. 5.10. Thermal radiation pattern of thin slot (Plot of Eqs. 5.52, 53, 55 with $\beta_o a = 9.3\pi$)

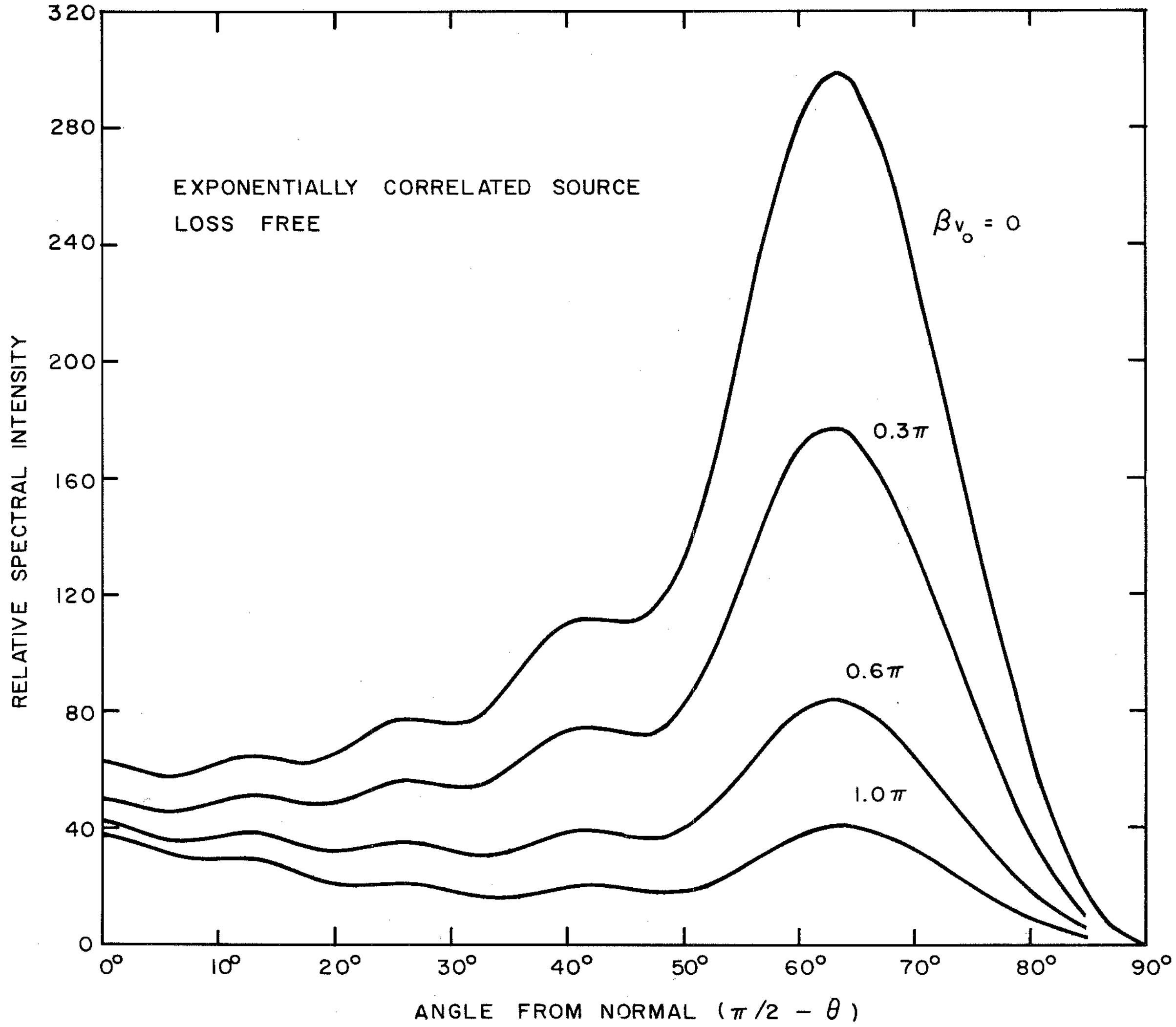

Fig. 5.11. Thermal radiation pattern of thin slot (Plot of Eqs. 5.52, 53, 55 with $\beta_o a = 9.5\pi$)

$$\lim_{u_o,v_o\to 0} N_1N_2\, e^{-\frac{|x_o-x_1|}{u_o}-\frac{|z_o-z_1|}{v_o}} = \delta(x_o-x_1)\delta(z_o-z_1)$$

then RS_e, Eq. 5.47, reduces in the limit to

$$RS_e(x_o-x_1,z_o-z_1,\omega) = \frac{2\overline{\epsilon}}{\sigma\delta}\,\delta(x_o-x_1)\,\delta(z_o-z_1) \tag{5.56}$$

Hence, if the correlation lengths are set equal to zero, then the equation for the pattern in the case of the partially-correlated source should reduce to that for the loss-free, delta-correlated source. The details of this computation follow. For $v_o = 0$, it follows that

$$A = 1$$

$$B = 1$$

$$2v_oN_2 = 1$$

$$G_3 = 0$$

and therefore Eq. 5.53 for G reduces to

$$G\Big|_{v_o=0} = \beta a\left[1+\sin^2\beta a - \cos\beta a\cos(\beta a\cos\Theta)\right] + \sin\beta a\left[\frac{4}{\sin^2\Theta}-1\right]\left[\cos\beta a - \cos(\beta a\cos\Theta)\right] \tag{5.57}$$

and by Eq. 5.52, the radiation pattern is

$$P_{f\Omega} = \frac{\omega\epsilon_o\overline{\epsilon}\,b\,(\alpha_1^2+\beta_1^2)^2}{\pi^2\,\sigma\,\delta\,\beta^4}\;\frac{1}{[\sin\beta a\sin\Theta]^2}\;G\Big|_{v_o=0} \quad . \tag{5.58}$$

The equations above for the limiting case of the partially correlated source are identical to the formula for the radiation pattern for the delta-correlated source case, Eq. 5.37. This is to be expected since the limiting form of the assumed source correlation function is Dirac's delta function. However, the reduction does serve a useful purpose as a partial check on the integration of Eq. 5.50.

5.6 Radiation Pattern for the Spatially-Coherent Source

In this section the thermal radiation pattern is computed for the spatially-coherent source. Spatially-coherent excitation occurs when the slot is illuminated by a plane wave traveling in the positive y direction in Fig. 5.2. The source of these plane waves can be either a remote point source of thermal radiation*, or a remote single frequency oscillator. For the noise source, the correlation function for the aperture electric field is given by

$$RR_e(x_o-x_1,z_o-z_1,\tau) = C_1\ \delta(\tau)$$

and by Eq. 3.13, the mixed correlation function is

$$RS_e(x_o-x_1,z_o-z_1,\omega) = C_1 \quad . \tag{5.59}$$

---

* It is well-known that a system of slits, when illuminated by a remote incoherent point source, will give rise to an interference pattern, i.e., Fresnel and Fraunhofer diffraction. Young was the first to recognize the importance of limiting the spatial extent of the source, and his famous experiments and deductions were the first conclusive demonstration of the wave nature of light.

Alternately, for the coherent or single frequency oscillator, the x-oriented electric-field excitation is of the form

$$e(x,z,t) = e_o \cos \omega_o \left(t - \frac{|y_o|}{c}\right) \tag{5.60}$$

where y_o is the distance to the remote source. Using the defining equation for the correlation function, Eq. 3.11, one can readily obtain the following result

$$RR_e(x_o-x_1,z_o-z_1,\tau) = \left\langle e(x_o,z_o,t_o)e^*(x_1,z_1,t_o-\tau)\right\rangle$$

$$RR_e(x_o-x_1,z_o-z_1,\tau) = \frac{e_o^2}{2} \cos \omega_o \tau \tag{5.61}$$

and by Eq. 3.13, the mixed correlation function is

$$RS_e(x_o-x_1,z_o-z_1,\omega) = \frac{e_o^2}{2} \int_{-\infty}^{\infty} \cos \omega_o \tau \, e^{-i\omega\tau} d\tau$$

$$RS_e(x_o-x_1,z_o-z_1,\omega) = C_2 \left[\delta(f - f_o) + \delta(f + f_o)\right] \tag{5.62}$$

where for convenience C_2 is defined as $C_2 = e_o^2/4$. The thermal radiation pattern for both of these examples of a spatially-coherent source can now be computed by the substitution of Eq. 5.59 or 5.62 into Eq. 5.30. Integrations with respect to x_o and x_1 give

$$P_{f\Omega} = \frac{\beta_o^2 \, b^2 C_3 \sin^2\theta}{2\pi^2 \eta_o} \iint_{-a/2}^{a/2} \Phi(z_o,\theta) \, \Phi^*(z_1,\theta) \, dz_o dz_1 \tag{5.63}$$

where $\Phi(z_o,\theta)$ is given by Eq. 5.29 and C_3 is defined below.

$$\begin{aligned} C_3 &= C_1 && \text{(for noise source)} \\ C_3 &= C_2 \, \delta(f - f_o) && \text{(for coherent oscillator).} \end{aligned} \tag{5.64}$$

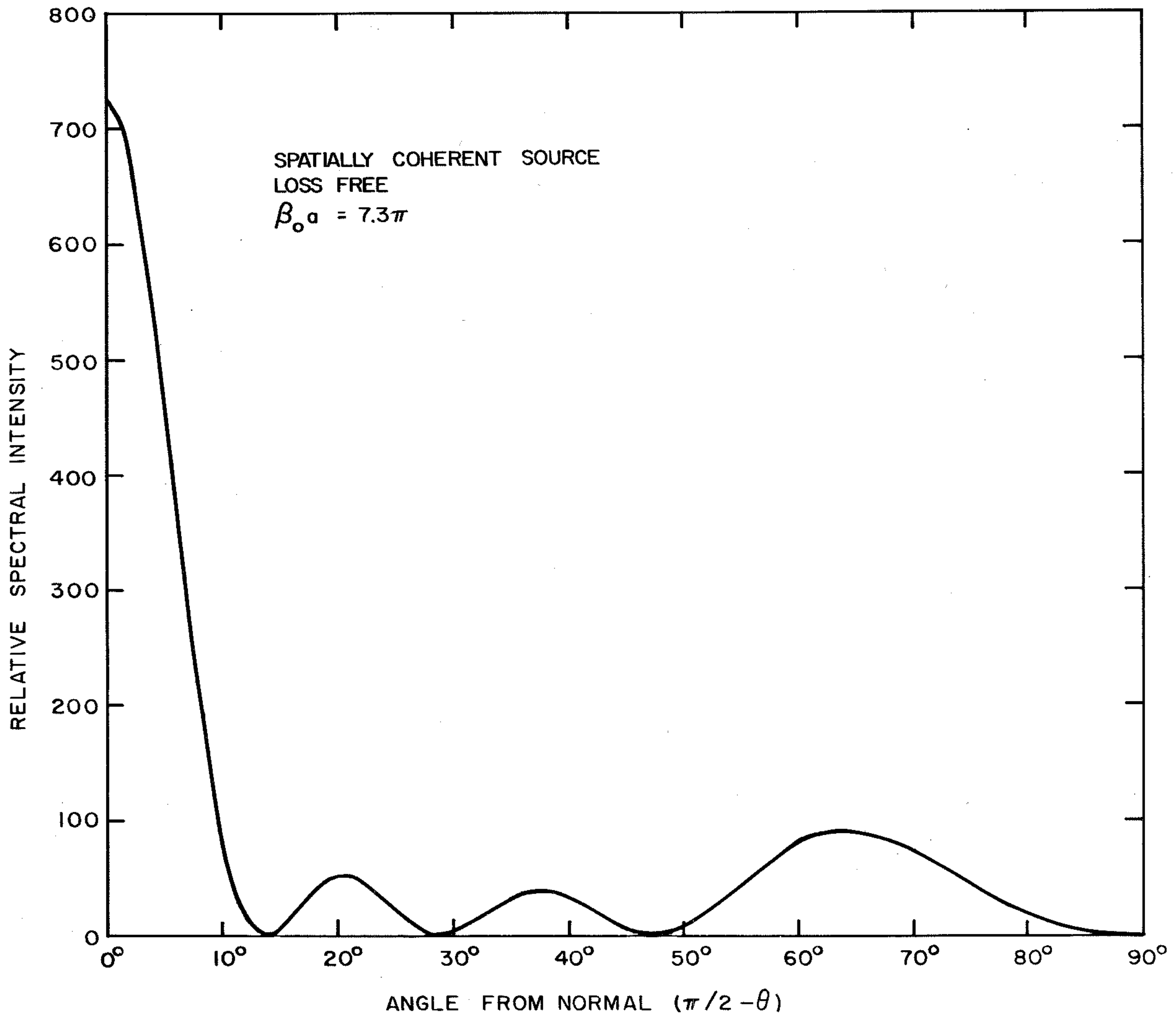

Fig. 5.12. Radiation pattern of coherently excited slot (Plot of Eq. 5.65 with $\beta_o a = 7.3\pi$)

Substituting into Eq. 5.63 for $\Phi(z_o,\Theta)$, setting the wave numbers equal, and integrating, one obtains the following formula for the radiation pattern.

$$P_{f\Omega} = \frac{b^2 C_3}{2\pi^2 \eta_o} \left[\frac{\beta a}{\cos \beta \frac{a}{2} \sin \Theta} \right]^2$$

$$\times \left[\frac{\cos(\beta \frac{a}{2} \cos \Theta) \sin \beta \frac{a}{2}}{\beta \frac{a}{2}} - \frac{\cos \beta \frac{a}{2} \sin(\beta \frac{a}{2} \cos \Theta)}{\beta \frac{a}{2} \cos \Theta} \right]^2 . \qquad (5.65)$$

The radiation pattern for the spatially-coherent excitation is plotted for $\beta a = 7.3\pi$ in Fig. 5.12. The spectral intensity $P_{f\Omega}$ is normalized to $b^2 C_3/(2\pi^2 \eta_o)$. It is interesting to compare this graph to that for the delta-correlated source in Fig. 5.3. For these two cases the relative amplitudes of the maxima are quite different, but the number of the maxima and their approximate positions are the same.

5.7 Experimental Radiation Patterns for the Thin Slot

There are two radiation experiments which would be very interesting to perform in the course of verifying the Leontovich-Rytov distributed noise formula. One of these is the measurement of the thermal radiation pattern of a thin hot wire of high conductivity. The other is the pattern measurement for a thin-slotted aperture in a highly-conducting plane wall of an isothermal enclosure. These experiments are of particular interest theoretically, because they can be treated analytically with considerable precision. Unfortunately, even using the most sensitive, present-day receivers, neither of these experiments is practical. Sample computations are presented in earlier sections to support this assertion as well as to determine the feasibility of alternate experiments which may be considered practical compromises. For example, one such computation leads to the conclusion that pattern measurements even with a lossy wire are not practical, and moreover, high losses smooth the interesting interference structure of the spatial distribution (Secs. 3.5 and 4.1). However, from another computation, the conclusion is drawn that pattern measurements are practical for the case of a thin slot excited by a gaseous discharge (Secs. 4.2 and 4.3). With this experiment in mind, thermal radiation patterns are computed for two different idealized slot excitations. In the first, a spatially-uncorrelated source is assumed with an attenuation factor for propagation along the slot (Sec. 5.4). In the second, an exponentially correlated source is assumed with a zero loss factor for propagation along the slot (Sec. 5.5). In this section, experimental data are presented for comparison to the theoretical results of these two analyses.

5.7.1 Description of Pattern Recorder. From a conceptual point of view, the measurement of a radiation pattern is quite simple. Briefly, a transmitter and a receiver are positioned at some fixed separation. For either antenna, the radiation pattern is simply the received signal as a function of the angular position as the antenna being measured is rotated about its center. However, the measurement of microwave thermal radiation patterns is made difficult in practice because of the extremely low signal levels. As an example, consider the signal return for a typical thin slot. The average signal to noise ratio at the input of a closely coupled low-noise microwave receiver is approximately $5^\circ/(290^\circ \cdot 6) = 1/350$, and the ratio drops to

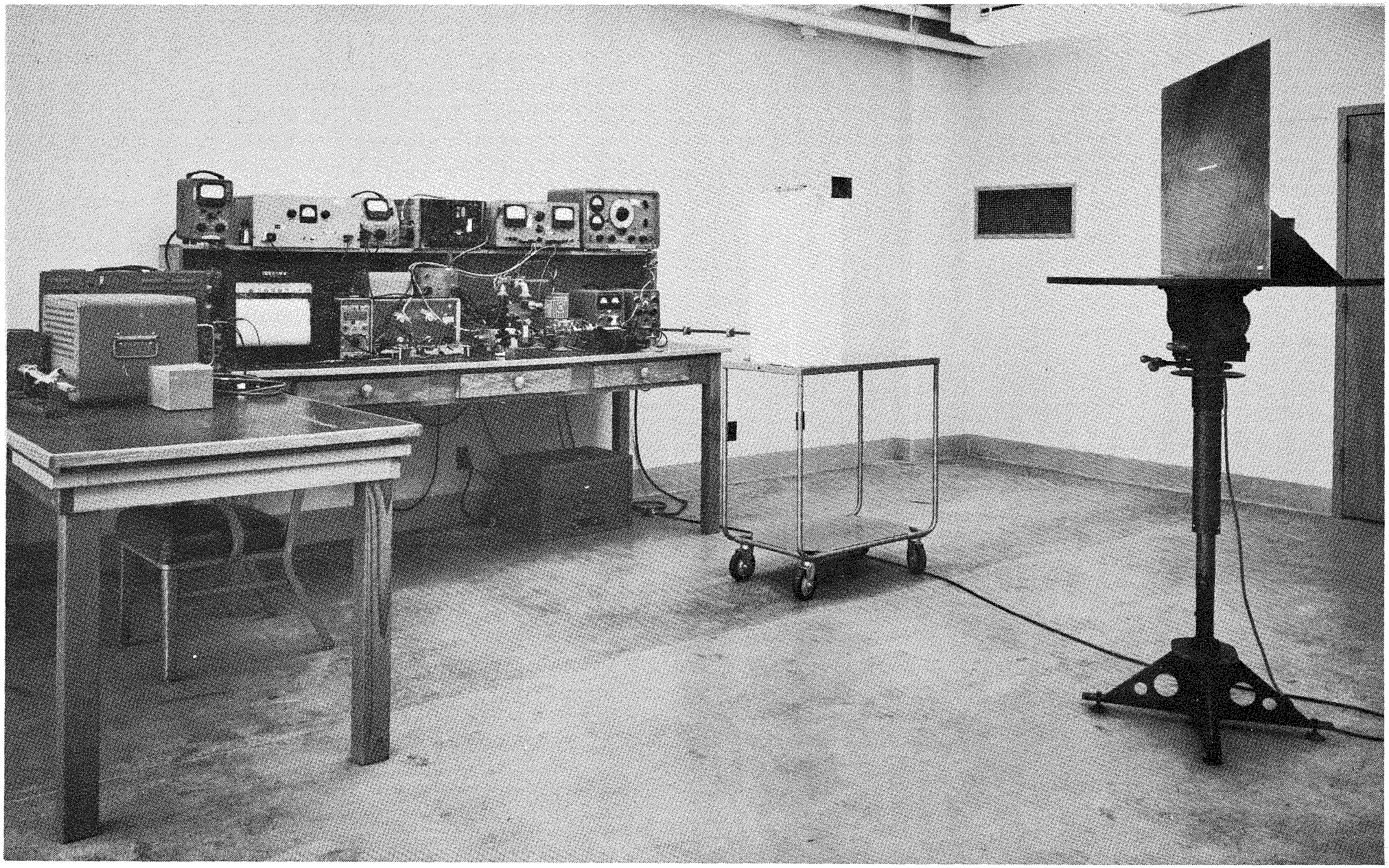

Fig. 5.12P. Laboratory radiometer for pattern measurements

about 1/2000 for a ripple or spatial fluctuation which is 1/5th of the average signal. Therefore, as a practical matter, it is necessary to make fairly careful selections of the slot length, the range, the receiving aperture, and the receiver in order to obtain the maximum signal level that is consistent with the other requirements imposed on a pattern recorder. These matters are discussed in the Appendices in detail. For the receiver, there are discussions of the theory, the design, and the performance in Appendices I, II, and III respectively. The range selection and its relation to the aperture sizes are detailed in Appendix IV, and the performance of the entire pattern recorder is reported in Appendix V. Here, a brief description of the apparatus is sufficient (Fig. 5.12P). The radiator is typically a 4.75 by 0.12-wavelength slot in a 28 by 19-wavelength ground plane. The glow discharge tube is clamped to the metallic ground plane directly behind the thin slot and the entire ground plane assembly is mounted on a large wooden turntable. The receiving aperture is positioned at a 1.50 m range with the electric field polarization perpendicular to the long edge of the radiating slot. The receiver is a narrow-bandwidth, Dicke radiometer (5). This radiometer has a ferrite modulator driven at 1,000 cps, a balanced mixer with Philco type IN263 low-noise crystals, a grounded-cathode grounded-grid preamplifier with Western Electric type 5842 low-noise tubes, an i-f amplifier and detector, a band-pass filter, a 1,000 cps balanced phase-detector with Texas Instruments 2N263 silicon transistors, a d-c amplifier, and a recording potentiometer. Regulated power supplies are used for all d-c voltages; and in turn, these are powered by a primary source of regulated 60 cps-110v power.

5.7.2 Accuracy of Measurements. The pattern recorder shown in Fig. 5.12P is designed with the major emphasis on high sensitivity. Wherever it is necessary, precision is compromised in order to attain increased sensitivity. For example, in the selection of an r-f mixer diode, the sole consideration is sensitivity at low levels, and linearity and long-term stability of the conversion characteristics are completely ignored. This sacrifice of precision is necessary; because even with the emphasis on sensitivity, the microwave thermal radiation levels are very close to the present-day threshold of detection.

The details of the data gathering process are described as a preface to the actual estimation of errors. Suppose two radiation patterns are to be recorded. This requires about six hours of actual experimental time which is utilized as follows: 1 hour warmup time, 1/2 hour for calibration, 2 hours for each pattern, and 1/2 hour for calibration. The two hours required for one complete pattern recording are itemized in more detail in Table 5.2. Due to the fine structure in the radiation pattern, it is necessary to read the signal level at intervals of 2.5°. Due to the long response time of the demodulator circuit, a stabilization interval of 30 sec is required after each change in angular position. Then, a recording time of 40 to 60 sec is used to provide adequate smoothing of the thermal fluctuations. Finally, a tedious zero-level determination is required in order to minimize the errors which are introduced by ambient temperature effects. It is clear from the itemized time requirement that quite large experimental errors can be introduced by slow drifts in the characteristics of the measuring apparatus.

Table 5.2

TIME REQUIRED FOR PATTERN RECORDING

Item	Time
For each data point	
Setting time	30 sec
Integration time	30
Recording time	40-60
Total	110 sec
For each pattern	
Number of signal points	45
Number of zero points	22
Total time (approx.)	2 hours

An estimation of errors was obtained by a study of a special four-hour calibration record and by a comparison of several different calibrations taken over a period of five months. The estimated errors are tabulated below. Certain of the tabulated fluctuations are partially eliminated by the method used in gathering the data. In the table this is indicated by enclosing the estimated error in parenthesis. For example, the zero-level is determined within a few minutes of the signal level reading and at every other angular position of the radiator. This eliminates two potentially large sources of error (the

Table 5.3

ESTIMATES OF EXPERIMENTAL ERROR

Source of Error	Magnitude (rms$^{\circ}$K)
1. Total fluctuation and reflection error	0.3
Thermal fluctuations	0.2
Short-term variation in zero-level	0.1
Long-term variation in zero-level	(0.5)
Positional variation in zero-level	(0.7)
Short-term variation in gain	0.1
Long-term variation in gain	(0.3)
Uncontrolled reflection (Appendix V)	0.17
2. Total calibration error (0.1 db)	20%

0.5 rms$^{\circ}$K and the 0.7 rms$^{\circ}$K entries in Table 5.3). Likewise, by the initial and final calibrations, long-term variations in gain can be detected and an approximate correction applied. It is assumed that the remaining errors are random and independent. Computing their rms value, one obtains a value of 0.3 rms$^{\circ}$K for the total fluctuation and reflection error.

The receiver is calibrated by using an argon noise source and a variable attenuator as a secondary standard (Appendix III). Although these measurements are reproducible to better than 5%, their absolute accuracy is probably no better than 20%. The use of a well-matched, variable temperature termination would permit a more precise calibration; however, this would not lead to any improvement in the measurement of the shape of the thermal radiation pattern.

5.7.3 Experimental Radiation Patterns. Experimental thermal radiation patterns are shown in Figs. 5.13 through 5.17. Patterns are presented for slot lengths of $\beta a/\pi = 7.3$, 7.5, 8.7, 9.3, and 9.5, and for a common slot width of $\beta b/\pi = 0.24$. First, these data are compared to the data taken at optical frequencies. It is seen from Fig. 2.2 that for a slot length of 0.1419 m (corresponding to $\beta a = 8.7\pi$ at 9200 mc/s), the optical radiation pattern is approximately Lambertian. In contrast to this, however, the spatial distribution of the microwave radiation is not even roughly Lambertian. In agreement with the theory, which is presented in this paper, the microwave radiation patterns are quite sensitive to the radian-length of the aperture; they exhibit a pronounced interference structure and a well-defined polarization; and the maximum radiation is not generally in the $\theta = \pi/2$ direction. From this comparison, it is concluded that the classical formulation does not apply, even as a rough approximation, whenever the radiator dimension and the wavelength are of the same order of magnitude.

A more detailed study of these experimental radiation patterns is made in this paragraph. First, by a comparison of the theoretical curves in Figs. 5.3 through 5.6 to the experimental data in Figs. 5.13 to 5.17, it is seen that there is good qualitative agreement between the theory and the experiment. As an empirical result, it is noted that the best fit to the data occurs for an attenuation constant in the range from 3 to 5 db/λ. It is expected from the theory and verified by an experiment (Sec. 4.3) that this attenuation constant is a function of the d-c current in the plasma discharge. There are certain discrepancies, however, between the data and the form of the theoretical result which is represented by Eq. 5.36. Consider, as an example, the results

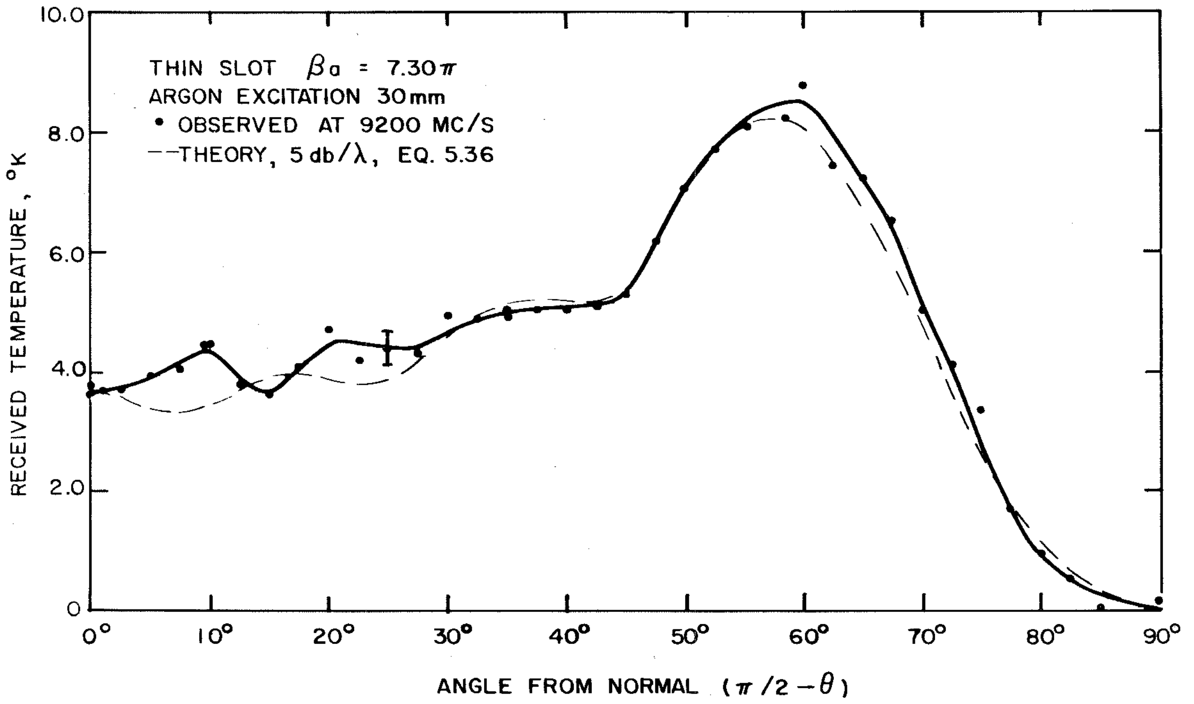

Fig. 5.13. Experimental radiation pattern for thin slot

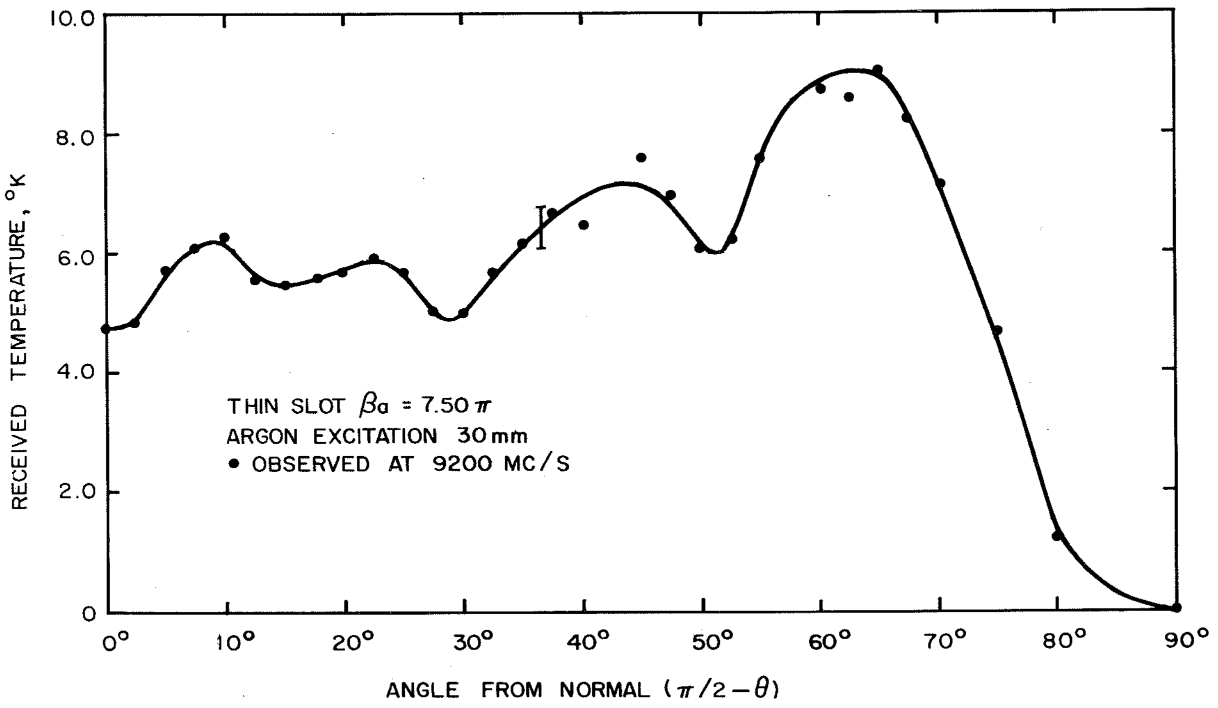

Fig. 5.14. Experimental radiation pattern for thin slot

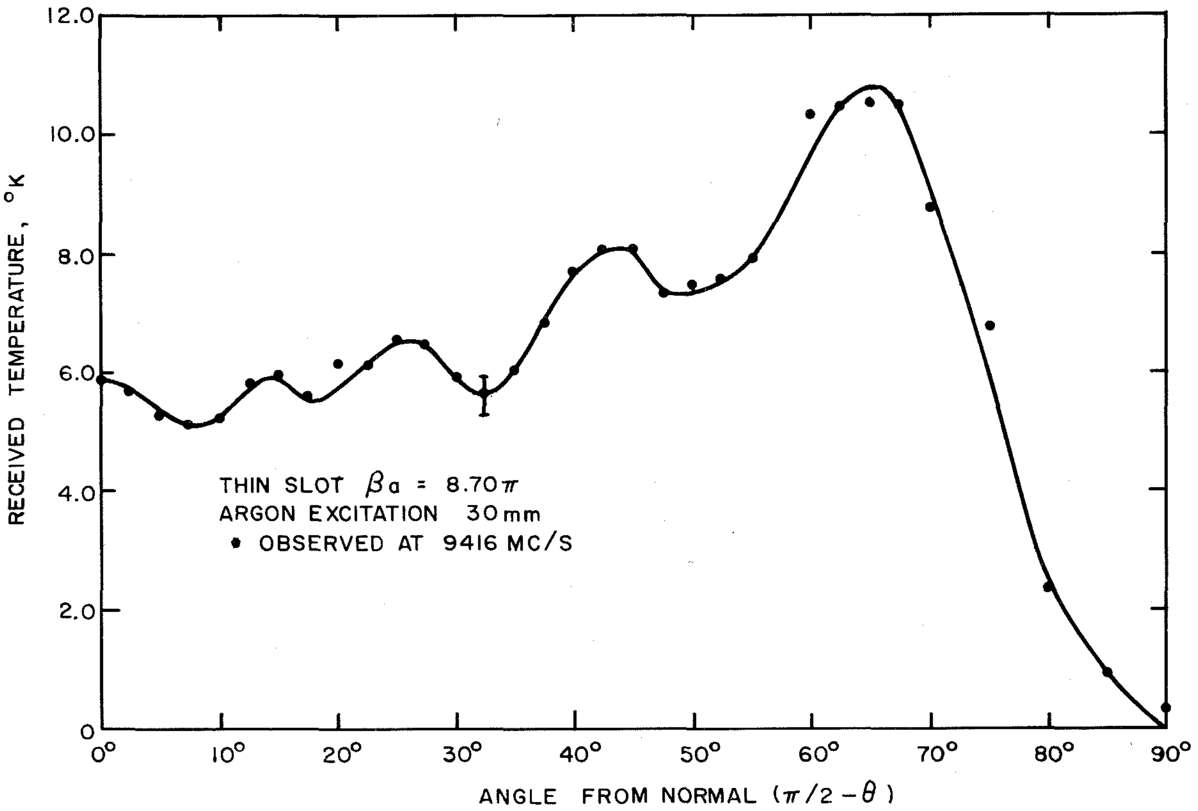

Fig. 5.15. Experimental radiation pattern for thin slot

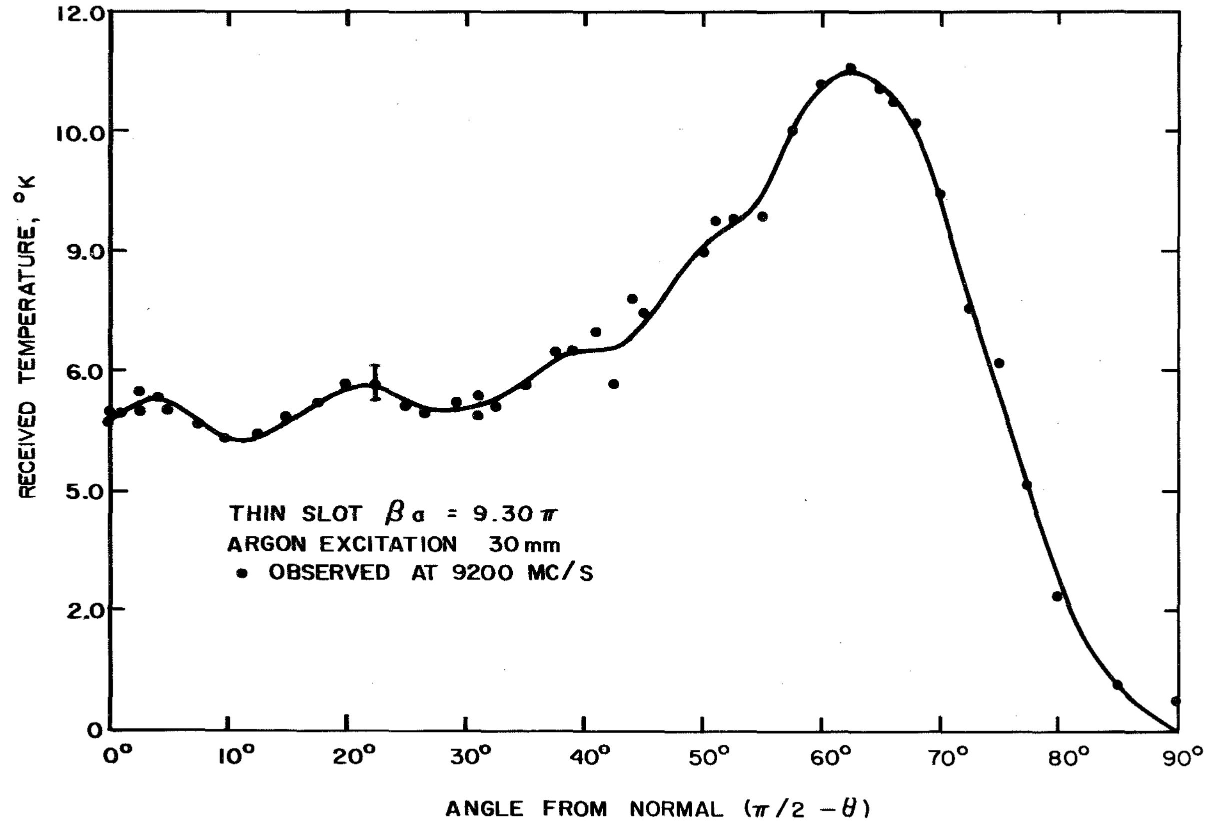

Fig. 5.16. Experimental radiation pattern for thin slot

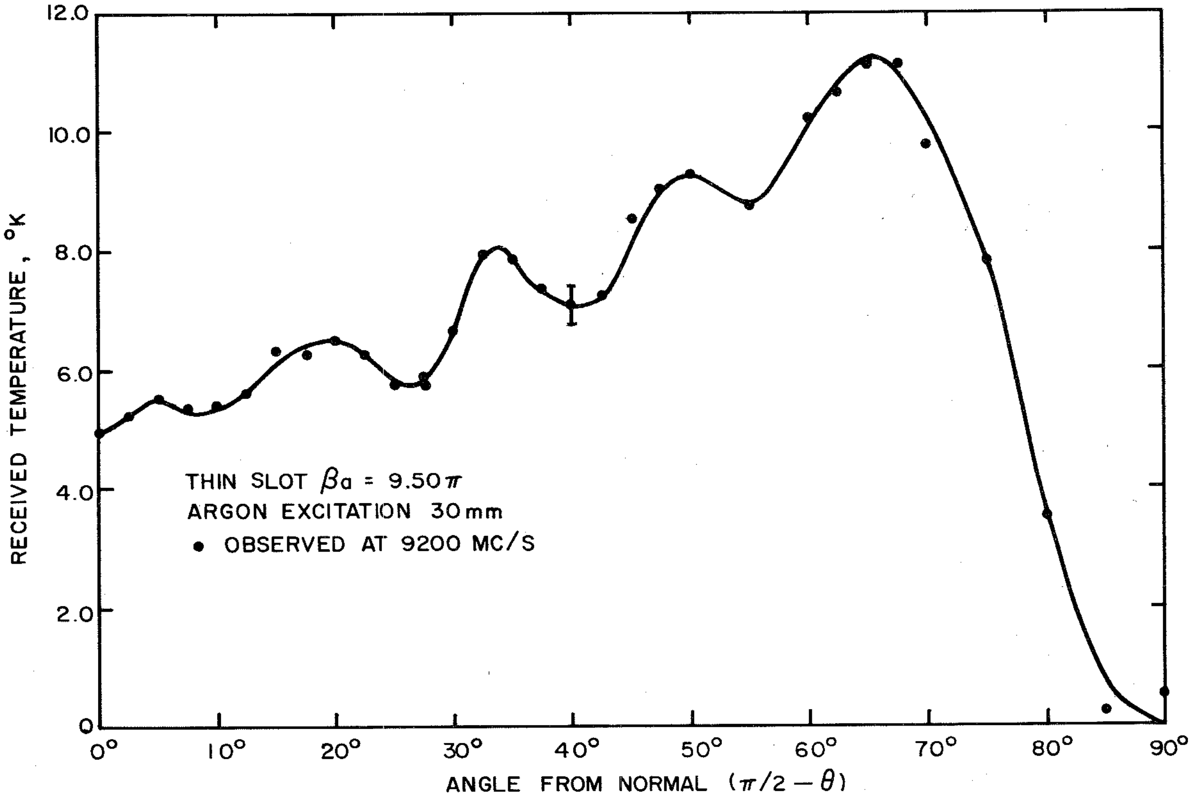

Fig. 5.17. Experimental radiation pattern for thin slot

for the slot with a radian length of 7.3π (see Fig. 5.13). The approximate angles at which the relative maxima occur are given by the theory as $(0^\circ, 16^\circ, 34^\circ, 59^\circ)$ and by the data as $(10^\circ, 21^\circ, 37^\circ, 60^\circ)$. The differences between corresponding angles exceed the experimental error, and there is also a distinct difference between these two curves at angles which are close to the normal. Moreover, it is noticed that for a slot length of 8.2π radians the angles for the relative maxima are given by the theory as $(7^\circ, 22^\circ, 38^\circ, 63^\circ)$. These values are in good agreement with the previously cited observed values. Similar discrepancies also occur in the other experimental data, and in each case the number of interference variations which are observed is slightly larger than the theoretical value. In other words, the effective electrical length of each slot is apparently slightly greater than the physical length. This conclusion can also be drawn by noticing the manner in which the number of interference variations increases with increasing length as shown in Fig. 5.7. The source of this discrepancy is readily traced to the simplifying assumption that the velocity of propagation along the slot is unchanged from the value in free space (Sec. 5.4.1). Although the geometry makes an exact solution difficult, it is known that the effect of the glass walls of the tube is to decrease the phase velocity along the slot while that of the plasma column itself is to increase this velocity. Apparently their combined effect is to slightly decrease the value of the phase velocity from that in free space. The observed discrepancy is described above in terms of an increased effective length; however, for quantitative purposes, one cannot simply assign a new effective length to a given slot and then compute the thermal radiation pattern from Eq. 5.36. The reason for this lies in the fact that the free space wave number enters the analysis as β_o in Eq. 5.18 and the complex wave number enters separately as $\beta_c = \alpha + i\beta$ in Eq. 5.17 for the aperture distribution. For this reason, the separate identities of these two wave numbers are retained in the more general form of the thermal radiation formula given by Eq. 5.35. Therefore, this equation should be used in order to obtain a closer approximation to the experimental patterns. However, further computational results are not presented due to the lack of a suitable theoretical estimate for the modified wave number β. Nonetheless, it is clear that the general equation, Eq. 5.35, which retains both an attenuation constant and a retardation variable, permits an even closer fit to the experimental thermal radiation patterns than that shown in the figures.

VI SUMMARY AND CONCLUSIONS

A combined theoretical and experimental investigation has been made of the spatial distribution of the radiant energy emitted by heated bodies for wavelengths at which the body dimensions and the wavelength are of the same order of magnitude. It is shown that in such cases the radiation pattern has the following characteristics:

1. It exhibits pronounced minima and maxima.
2. It is sensitive to the radian dimensions of the body.
3. It can have a well-defined polarization.
4. It is not, in general, a maximum in the direction for which the radiator subtends the maximum solid angle.

If one wishes to compute, say, a radiation pattern for a transmitting antenna, there are two different analytical approaches. In the first, one considers the antenna as a transmitter of electromagnetic waves and proceeds to the solution either along the lines of the assumed-current-distribution technique, or along those of the more sophisticated boundary-value-problem technique. In the second, one turns to the solution of a related problem in which the given antenna is considered as a receiving antenna. Then, by invoking some form of the reciprocity principle, one arrives at the desired solution. In this paper both of these approaches are used, the receiver method in Sec. 4.1 and the transmitter method in Sec. 5.2 and 5.3. It is worth while to present both of these methods of solution, because they start on quite a different basis and they use different simplifying assumptions; and hence, they result in slightly different approximations to the rigorous solution.

By direct experimentation, it is demonstrated that the thermal radiation pattern does exhibit the above-itemized characteristics when the body dimensions and the wavelength are of the same order of magnitude. In making measurements of a thermal radiation pattern at microwave frequencies it is necessary to have both a very hot source and a very sensitive receiver. In the experiments reported a source temperature of 10,100°K is obtained by using the radiation from the positive column of a d-c discharge in argon, and a receiver sensitivity of 0.3 rms°K is obtained by means of a Dicke radiometer.

The experiments reported in this paper provide a successful demonstration of an interference phenomenon using a source excitation which is incoherent and spatially extended. Newton in expressing his objections to the wave theory of light rested his case, in part, on the failure to observe any interference phenomenon in experiments with just such sources. This may be seen from the following quotation (10):

> "Are not all hypotheses erroneous in which light is supposed to consist in pression or motion propagated through a fluid medium? If light consists only in pression propagated ... it would bend into the shadow. For pression or motion cannot be propagated ... in right lines beyond an obstacle."

Since the later success of Young (1801) with his ingenious scheme to achieve spatial coherence of the aperture illumination, it has been widely assumed that interference effects are not observable using a spatially extended incoherent source. In view of the experiments reported herein, this assumption is not correct. In fact, by direct analogy, it appears to be quite practical now to demonstrate the same interference phenomenon at optical wavelengths using spatially extended incoherent sources.

APPENDIX I - SURVEY OF RADIOMETER THEORY

The problem of detecting the thermal radiation from either a heated wire or a noise excited thin slot is the same detection problem which is encountered in radio astronomy. In these two applications both the signal and the internal receiver noise have essentially the same wide uniform spectral density. Dicke devised a practical method for detecting and measuring such signals even though they are less than 1/1000th of the level of the receiver noise (5). Later improvements in microwave radiometers have been mainly the result of improvements in technology and minor revision rather than the result of fundamental innovations (20),(25),(26). A good understanding of the operation of the radiometer can be gained from the following analysis of a conventional microwave receiver (5). Consider a receiver that consists of an r-f mixer with image rejection, an i-f amplifier of bandwidth α, and a square law diode detector of time constant τ. The overall noise figure of the receiver is F. Both the signal and the receiver noise are assumed to be of the following form. The output amplitude consists of short pulses which have an equal probability of being zero or FT_o. The average number of output pulses per unit time is limited to α. At the input to the final long time constant circuit, the root-mean-square value of the output distribution is $FT_o/2$. Since the detector averages over $\alpha\tau$ samples, by the law of large numbers, the expected value of the root-mean-square deviation is given by $FT_o/[2(\alpha\tau)^{1/2}]$. This is the "fundamental fluctuation" in the output of the receiver. For a small change in the input temperature, the signal to noise ratio is unity when this change, ΔT_o, satisfies the following equation.

$$\frac{\Delta T_o}{T_o} \doteq \frac{F}{2(\alpha\tau)^{1/2}}$$

$$\frac{\Delta T_o}{T_o} \propto \frac{F}{(\alpha\tau)^{1/2}} \quad . \qquad \text{(A-1.1)}$$

The same functional variation is also obtained for the case of a linear detector. Although the analysis above is not precise, it demonstrates in a very clear manner how the threshold of detection can be improved by increasing the product of the amplifier bandwidth and the detector time constant.

Consider the model of the Dicke radiometer shown in Fig. A-1.1. Briefly, it consists of a modulator driven at a frequency f_o, an amplifier of bandwidth α centered at a frequency f_1, a square law detector, a band-pass filter of bandwidth γ at a frequency of f_o, a synchronous phase detector driven at f_o, and a low-pass filter of bandwidth β. The operation of this receiver is summarized in the spectral density diagrams shown in Fig. A-1.2. The input signal, denoted by $\overline{\epsilon}_a \doteq kT_a$, is amplitude-modulated at a frequency f_o which ranges characteristically from 10 to 10,000 cps. The receiver noise $\overline{\epsilon}_n$ is assumed to be introduced just after the modulation process, i.e., at point (1) in Fig. A-1.1. These spectral densities are shown as P_{f1}. That portion of the input spectral density which is shown shadowed is amplified and detected. At point (2) the spectral density, P_{f2} has a delta-function component at a frequency $f = 0$ which corresponds to the rms value of the signal plus noise and another at $f = f_o$ which corresponds to the modulated signal above. Now, the detected signal is filtered and amplified, synchronously detected, and

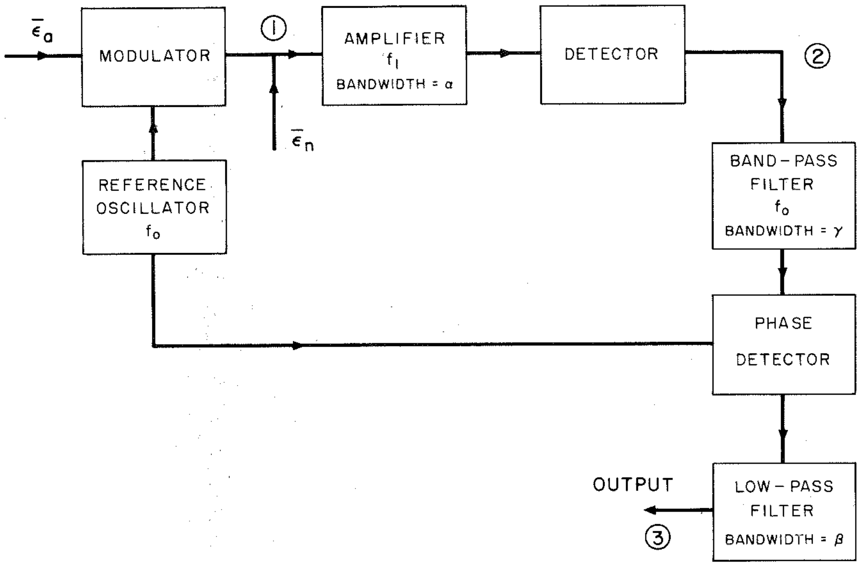

Fig. A-1.1 Model of the Dicke Radiometer [after Goldstein (27)]

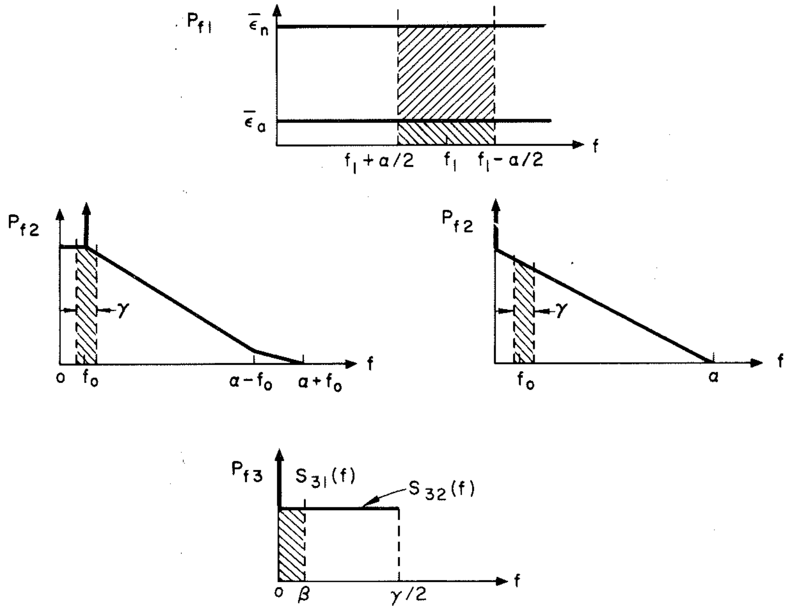

Fig. A-1.2. Components of the spectral density finally, it is filtered again. At point (3) the spectral density, P_{f3}, consists of a delta-function signal component, S_{31}, and a fluctuation term, S_{32}. Goldstein has shown that these output spectral densities are given by (27)

$$S_{31} = \frac{C}{16} \,\overline{\epsilon}_a^2\, \delta(f) \qquad \text{(A-1.2)}$$

and

$$S_{32} = \frac{C}{\alpha}\left[2\overline{\epsilon}_n^2 + \frac{3}{2}\,\overline{\epsilon}_a\overline{\epsilon}_n + \frac{17}{32}\,\overline{\epsilon}_a^2\right], \quad 0 < f < \frac{\gamma}{2} \qquad \text{(A-1.3)}$$

in which C is a gain constant for the system. The output signal power is given by

$$S = \int_0^{\beta} S_{31}\, df$$

$$S = \frac{C}{16}\,\overline{\epsilon}_a^2 \quad . \qquad \text{(A-1.4)}$$

In this receiver, the entire fluctuation power constitutes noise. Hence, the noise output power is given by

$$N = \int_0^{\beta} S_{32}\, df$$

$$N = \frac{C\beta}{\alpha}\left[2\overline{\epsilon}_n^2 + \frac{3}{2}\,\overline{\epsilon}_a\overline{\epsilon}_n + \frac{17}{32}\,\overline{\epsilon}_a^2\right] \quad . \qquad \text{(A-1.5)}$$

By Eqs. A-1.4 and 1.5, the output signal to noise ratio is

$$\frac{S}{N} = \frac{1}{32}\left(\frac{\overline{\epsilon}_a}{\overline{\epsilon}_n}\right)^2 \frac{\alpha}{\beta}\; \frac{1}{\left[1 + \frac{3}{4}\frac{\overline{\epsilon}_a}{\overline{\epsilon}_n} + \frac{17}{64}\left(\frac{\overline{\epsilon}_a}{\overline{\epsilon}_n}\right)^2\right]} \quad . \qquad \text{(A-1.6)}$$

For an output signal to noise ratio of unity, assuming that the input signal level is much less than the input noise level, i.e., assuming $\bar{\epsilon}_a \ll \bar{\epsilon}_n$, the minimum detectable signal is given by

$$\left(\frac{\bar{\epsilon}_a}{\bar{\epsilon}_n}\right)_{min} \doteq 5.6 \sqrt{\frac{\beta}{\alpha}} \quad . \qquad \text{(A-1.7)}$$

Now, a numerical computation is presented using the design values for the radiometer which is described in Appendices II and III. The effective amplification bandwidth is (2)(8) = 16 mc/s; the measured overall noise figure is $F = 5$ (7db); and the integration time is $\tau = 1/\beta = 30$s. Therefore by Eq. A-1.7, the approximate value for the minimum detectable temperature is $(5.6)(5)(290)/(23 \cdot 10^{+3}) = 0.35$ rms°K. The measured value of this fluctuation is 0.2 rms°K, Table 5.3.

APPENDIX II - DESCRIPTION OF RADIOMETER RECORDER

A microwave radiometer was designed for the specific purpose of measuring thermal radiation patterns. While the details of this design would carry us too far afield, it is a matter of some interest to trace through a brief description of the final equipment. A block diagram of the receiver is shown in Fig. A-2.1, and the sub-assemblies are described below.

2.1 Antenna

The antenna is a microwave horn of dimensions $L_a = 11.10$ cm, $L_b = 8.04$ cm and a throat length of 17.2 cm, Fig. A-4.2. The measured absolute power gain is 72 at 9200 mc/s, and the effective solid angle subtended at a 1.50 m range is 2.70×10^{-3} steradian.

2.2 Modulator

A ferrite modulator is used which has fairly uniform performance characteristics from 8500 to 9600 kmc/s. The insertion loss is less than 0.4 db and the maximum attenuation is in excess of 25 db. The input and output flanges have a relative rotation of 45°. The driving coil is 68 turns of 27 AWG, self-resonant at 7 mc/s. A sinusoidal current of 0.70 a-rms from a 10 ohm source produces approximately 100% modulation of the r-f carrier.

2.3 Isolator

Two permanent-magnet ferrite isolators are used to prevent the local oscillator leakage and the crystal noise from being modulated. The measured forward insertion loss is 0.9 db and the reverse insertion loss is approximately 40 db. The Kearfott Co. type W-177-2K isolator is used.

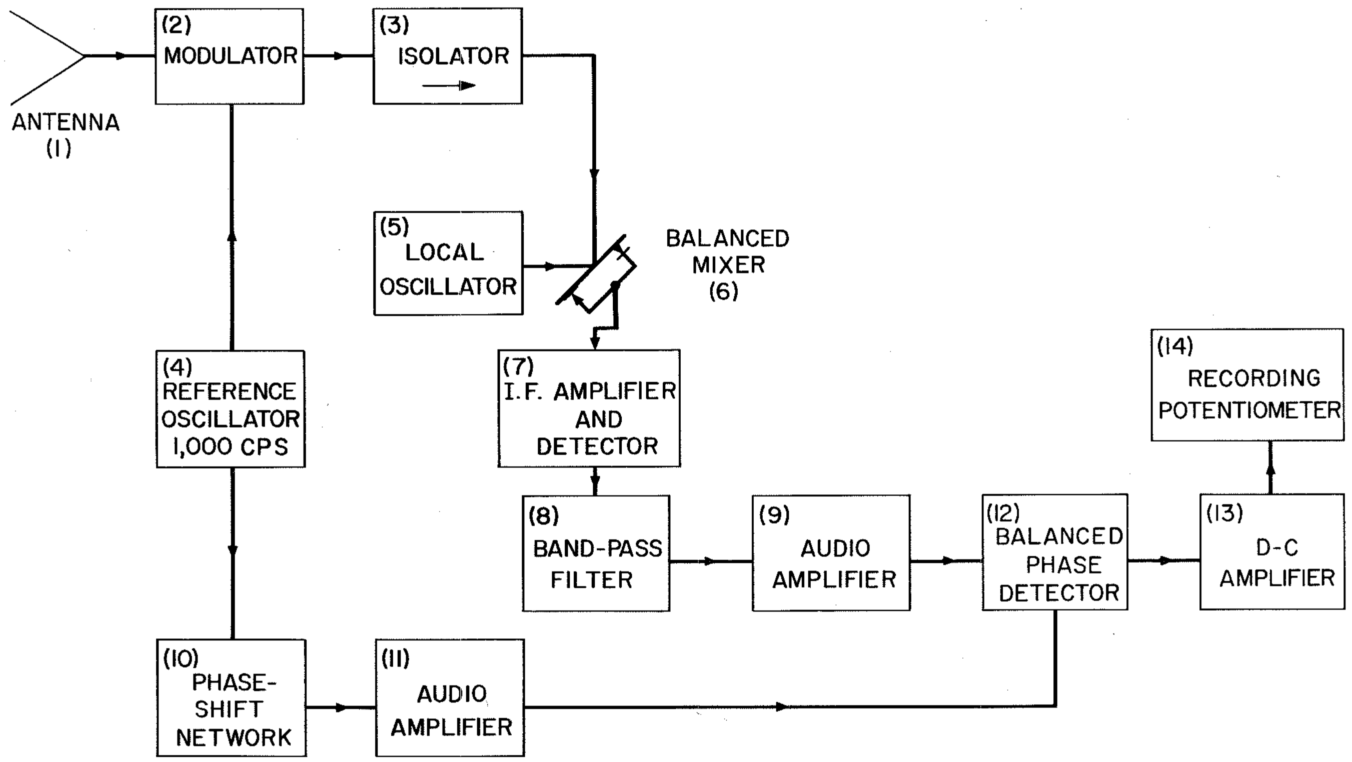

Fig. A-2.1. Descriptive diagram of radiometer for pattern measurements

2.4 Reference Oscillator

The reference oscillator supplies 30 v-rms at an impedance level of 600Ω and a frequency of 1,000 cps. The Hewlett-Packard type 205AG audio signal generator is used.

2.5 Local Oscillator

A reflex klystron is used to supply r-f power to the mixer. The frequency is manually adjusted by the setting of a bias voltage which, in turn, governs the heating rate of a temperature sensitive cavity. A Raytheon type 6116 klystron is used.

2.6 Balanced Mixer

The balanced mixer consists of a magic-tee waveguide component and a pair of crystals with a very low noise figure. The Philco type 1N263 crystal is used.

2.7 I-F Amplifier and Detector

The i-f amplifier has a bandwidth of 8mc/s centered at 30 mc/s. A noise figure of 1.19 (1.4 db) is achieved with a grounded-cathode grounded grid input cascade which uses the Western Electric type 5842 tubes. The detector level is approximately -1.0 v-dc. The effective time constant in the agc circuit is approximately 10 ms.

2.8 Band-Pass Filter

The band-pass filter is centered at a frequency of 1000 cps; it is down 3db at 750 and 1,300 cps; and it falls at 24 db/octave outside of the pass-band. The Krohn-Hite type 330-M filter is used.

2.9 Audio Amplifier

The Hewlett Packard type 450A audio amplifier is used to provide 40 db of audio gain with high stability.

2.10 Phase Shift Network

A simple L-R-C phase shift network is used to permit slight adjustments in the phase of the reference voltage which is coupled to the balanced phase detector. This adjustment is used to peak the final output signal.

2.11 Audio Amplifier

This audio amplifier provides isolation and 20db of audio amplification. The Hewlett Packard type 450A amplifier is used.

2.12 Balanced Phase Dectector

The balanced phase detector uses two Texas Instruments type 2N263 transistors in a degenerative common emitter configuration. The conversion slope is approximately 45 mv-dc output for 10 mv-rms input.

2.13 D.C. Amplifier

A time constant of 30 sec at the input of the d-c amplifier is used to fix the integration time for this radiometer. The d-c amplifier is provided to isolate the relatively high impedance of the RC time constant from the low input impedance of the recording potentiometer. A Kay Lab type 110A amplifier is used.

2.14 Recording Potentiometer

The recording potentiometer has a full-scale deflection sensitivity of 20 mv, and the paper rate is one inch per minute. A Brown Electronik Potentiometer is used.

APPENDIX III - SENSITIVITY OF THE LABORATORY RADIOMETER

In Fig. A-3.1, a calibration curve is shown for the laboratory radiometer which is described in Appendix II. The steps are labeled in degrees Kelvin corresponding to the change in the noise temperature of a well-matched source which replaces the antenna element during calibration tests. The source used consists of a calibrated r-f attenuator and an argon noise tube. The change in the source temperature, say, from T_1 to T_2 caused by a change in the attenuator from A_1 to A_2 is given by an application of Kirchhoff's law as follows:

$$T_{1,2} = T_a \frac{1}{A_{1,2}} + T_o\left(1 - \frac{1}{A_{1,2}}\right) \qquad \text{(A-3.1)}$$

$$T_2 - T_1 = (T_a - T_o)\left(\frac{1}{A_2} - \frac{1}{A_1}\right) \qquad \text{(A-3.2)}$$

For the argon source $T_a = 10{,}072$ and therefore the temperature difference is given by

$$T_2 - T_1 = 9780\left(\frac{1}{A_2} - \frac{1}{A_1}\right) \qquad \text{(A-3.3)}$$

in which the attenuation A is related to the decibel attenuation by $|\text{db attenuation}| = 10 \log_{10} A$.

The final radiometer unit is a stable reliable microwave receiver. A comparison of the calibration records taken over a period of several months shows a variation of only ± 8% with virtually no maintenance. A tabulation of the magnitudes of various fluctuations is given in Sec. 5.7.2.

The final radiometer unit shows a variation in sensitivity of less than ± 6% over the range of frequencies from 8900 to 9600 kmc/s. There

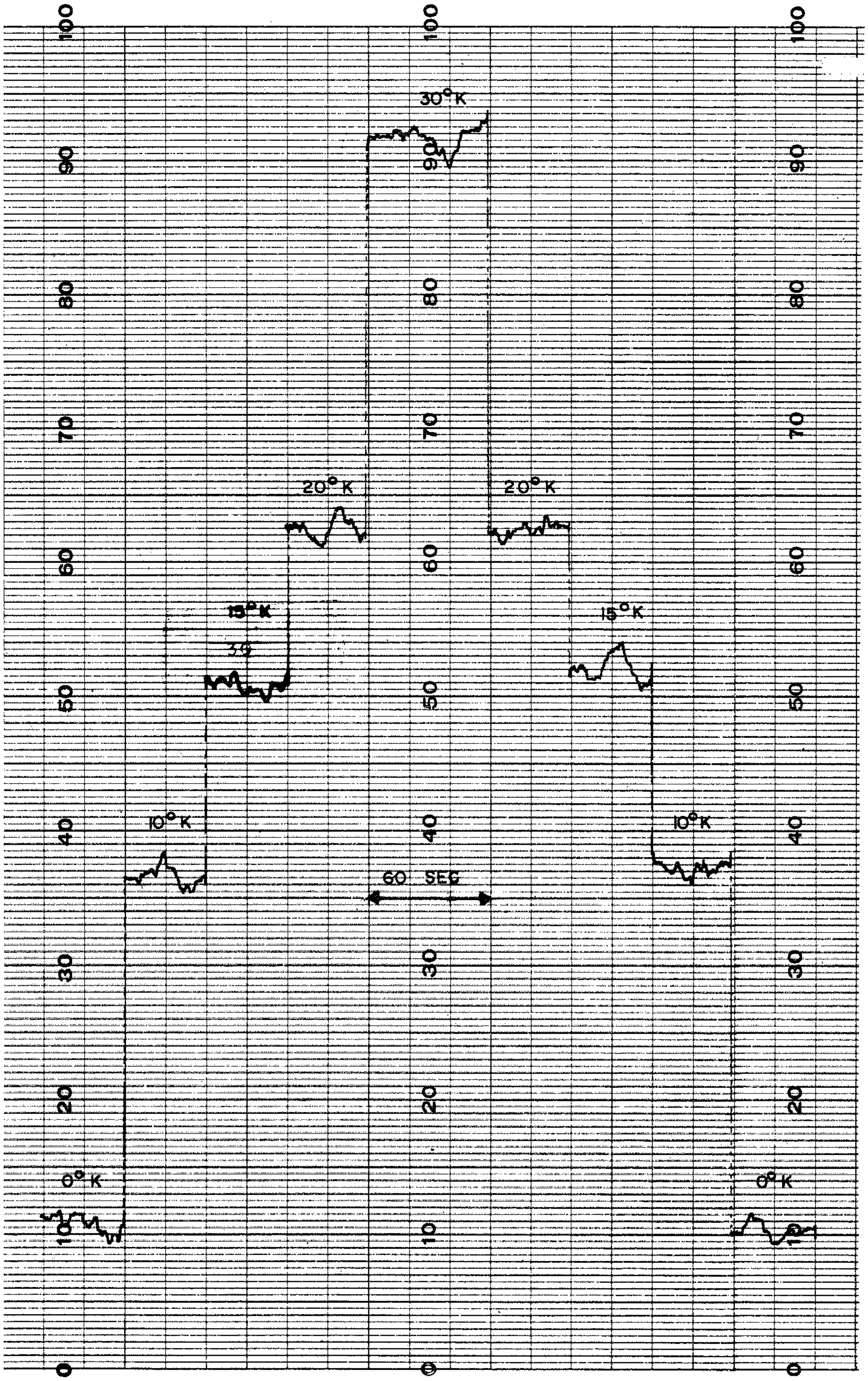

Fig. A-3.1. Calibration record

is no particular effort made in this design to attain a wide band of operating frequencies and the above-stated range is by no means an upper limit.

APPENDIX IV - ANTENNA RANGE CONSIDERATIONS

The selection of a convenient distance or range for Fraunhofer pattern measurements is generally a compromise between pattern accuracy and signal level, with the primary consideration usually being one of pattern accuracy. However, due to the very low levels of signal strength in this experiment, the primary consideration is necessarily one of signal level. Alternatives to the measurement of the Fraunhofer pattern in the Fraunhofer region are described in the literature (28), but they were not considered advantageous for this experiment.

First, various criteria which appear in the literature are reviewed (29). The transition to the Fraunhofer region occurs for $\Delta < \lambda/2$; this fixes a lower limit on the range given by $R_f > L_1^2/4\lambda$ (Fig. A-4.1). Now, as Δ decreases from the half wavelength value, the differential contributions in signal from the aperture become more nearly in phase, and the received signal level rises approaching the Fraunhofer level as $\Delta \to 0$. For a typical case, Silver shows power measurements of 1%, 6%, and 20% accuracy, corresponding to ranges which are given by $R = 2L_1^2/\lambda$, L_1^2/λ, and $L_1^2/2\lambda$, respectively. Finally, it is important to limit the amount of smoothing or smearing in the measurement of the radiation pattern. Since important pattern variations can occur for angular spacings of the order of $\phi = \lambda/L_1$ (this is the approximate central peak to null spacing for an in-phase array), an arbitrary limit is placed on the span of L_2, as follows.

$$\frac{L_2}{R} < \frac{1}{2}\frac{\lambda}{L_1} \rightarrow R > \frac{2L_1L_2}{\lambda} \quad . \qquad \text{(A-4.1)}$$

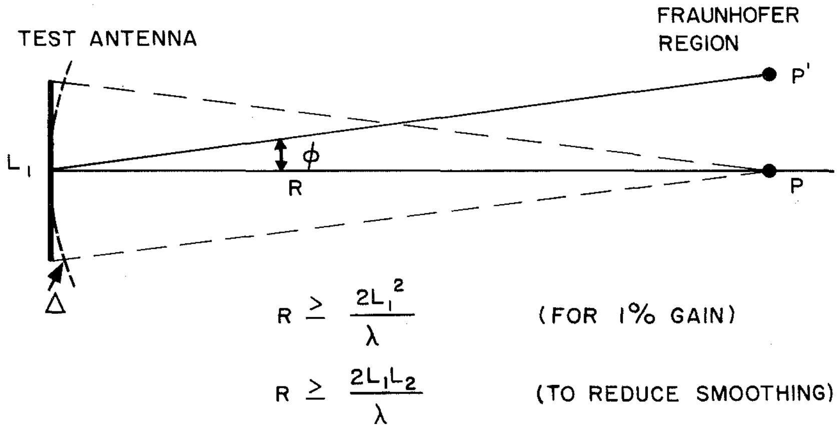

Fig. A-4.1. Pattern range criteria

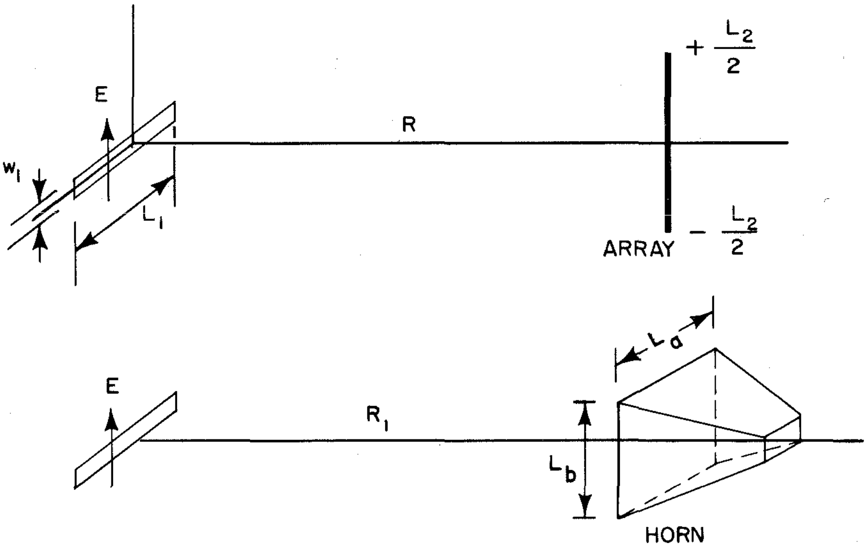

Fig. A-4.2. Comparison of receiver antennas

Limiting the smoothing of pattern variations is quite important in this experiment, since in general, the nulls to be observed are not very pronounced. The selection $R \sim 2L_1L_2/\lambda$ is made on this basis. From above, this fixes the ultimate accuracy of uncorrected power measurements to approximately 1%. However, probable errors due to other factors degrade this value.

The propagation losses for three cases of interest are computed in the following three paragraphs. First, consider the case in which the pattern of a sinusoidally-excited slot is to be measured using a high-gain linear array for the receiver (Fig. A-4.2). The ratio of the power received, p_r, to the power transmitted, p_t, is given by

$$\frac{p_r}{p_t} = \frac{G_1A_2}{4\pi R^2} \quad . \tag{A-4.2}$$

The maximum gain of the slot for sinusoidal excitation is of the order of the gain for a full-wave dipole, i.e., $G_1 \doteq 2.41$ (3.82 db); and the effective area of the receiving array is given by (18)

$$A_2 = \frac{L_2\lambda}{2\pi} \quad . \tag{A-4.3}$$

Thus, for this case, the range requirements are

$R > 2L_1^2/\lambda$ (based on power accuracy) (A-4.4)

$R > 2L_1w_2/\lambda$ (based on smoothing) (A-4.5)

$R > 2L_2w_1/\lambda$ (based on alignment stability) . (A-4.6)

Since $w_1, w_2 \ll \lambda$, Eq. A-4.4 establishes R. Clearly, Eq. A-4.6 is satisfied for L_2 as large as $L_2 = R/2$ (Although the estimate of A_2 given above is too high for this ratio of L_2/R, it will be used.) Substitution of these values into Eq. A-4.2 gives

$$\frac{p_r}{p_t} \doteq \frac{1}{131} \left(\frac{\lambda}{L_1}\right)^2 \qquad \text{(A-4.7)}$$

and assigning the value $L_1 = 4.5\lambda$ gives the following power ratio.

$$\frac{p_r}{p_t} \doteq \frac{1}{2700} \quad . \qquad \text{(A-4.8)}$$

Now, replace the receiving array by a horn of dimensions L_a, L_b flared in both planes, Fig. A-4.2. The controlling range requirement is

$$R = \frac{2L_1L_a}{\lambda} \qquad \text{(based on smoothing)} \quad . \qquad \text{(A-4.9)}$$

Since $G_1 \doteq 2.41$ and $A_2 = \alpha_e L_a L_b$, the expression for the power ratio reduces to

$$\frac{p_r}{p_t} = \frac{\alpha_e}{20.8} \frac{\lambda^2 L_b}{L_1^2 L_a} \quad . \qquad \text{(A-4.10)}$$

The efficiency factor α_e depends on the horn dimensions. For a horn of great length (or with a lens), the efficiency is $8/\pi^2$, i.e., $\alpha_e = 0.81$; and for a short horn of optimum dimensions, flared in both planes $L_b/L_a = 0.81$ and $\alpha_e = 0.50$ (18). Therefore, with careful design, a special horn-lens system could be devised for which

$$\frac{p_r}{p_t} \doteq \frac{0.81}{20.8} \left(\frac{\lambda}{L_1}\right) \qquad \text{(A-4.11)}$$

assuming that a practical maximum for L_b is $L_b = R/2$. Thus for $L_1 = 4.5\lambda$, the highest practicable value for the power ratio is $p_r/p_t = 1/116$.

For a short horn of optimum dimensions, the power ratio, Eq. A-4.10, reduces to

$$\frac{p_r}{p_t} \doteq \frac{1}{51.5} \left(\frac{\lambda}{L_1}\right)^2 \quad . \qquad \text{(A-4.12)}$$

Thus for $L_1 = 4.5\lambda$, the propagation loss at the minimum range is given by

$$\frac{p_r}{p_t} \doteq \frac{1}{1040} \quad . \qquad \text{(A-4.13)}$$

The following conclusions are drawn from the above computations. The horn is clearly superior as a receiving antenna in this application. Eq. A-4.12 demonstrates an interesting fact, i.e., the propagation loss is not a function of the (H-plane) gain of the receiving antenna under the close-coupling condition of Eq. A-4.9. Improvement results if the L_b/L_a ratio is increased, provided one is willing to incorporate a sophisticated horn-lens system. In this latter case, assuming an idealized upper limit for L_b, i.e., $L_b = R/2$, leads to an improvement over that in Eq. A-4.12 which is given by Eq. A-4.11. For the example considered, the maximum improvement is approximately tenfold.

APPENDIX V - ACCURACY OF PATTERN MEASUREMENTS

In this appendix, a comparison is made between a pattern recorded using an automatic recorder and an outdoor range, and a pattern recorded using the radiometer and an indoor range, Fig. 5.12P. From our point of view the former measurement represents a precision standard against which the radiometer range may be judged.

An E-plane radiation pattern for a metallic horn, $L_a = 19.9$ cm, $L_b = 15.3$ cm, and a throat of 27 cm, is shown in Fig. A-5.1. This pattern represents a precision measurement taken on a range at the Hughes Aircraft Company, Culver City, California. The antenna to be measured is used as a receiving antenna, positioned at approximately 250 m from a milliwatt-level microwave transmitter. The measured absolute gain of the horn described is 138. Therefore, the efficiency factor is computed as follows: $\alpha_e = G\lambda^2/(4\pi L_a L_b) = 0.38$. As an interesting sidelight, the measured absolute gain can be compared to the theoretical value. For $\lambda = 3.26$ cm ($f = 9200$ mc/s), using Schelkunoff's formulas (30), the gain is found to be $G = \frac{\pi}{32}(42)(35) = 144$. The agreement to within four percent between the measured and computed values is good.

A comparison E-plane radiation pattern for the horn described above is shown in Fig. A-5.2. This pattern was taken using the radiometer receiver and the range shown in Fig. 5.12P. The antenna being measured is used as the transmitter, replacing the slotted ground plane shown in the figure. The source of the transmitter power is an argon discharge tube*. It is important to emphasize that by coupling the

---

*This tube is described in Sec. 4.2.

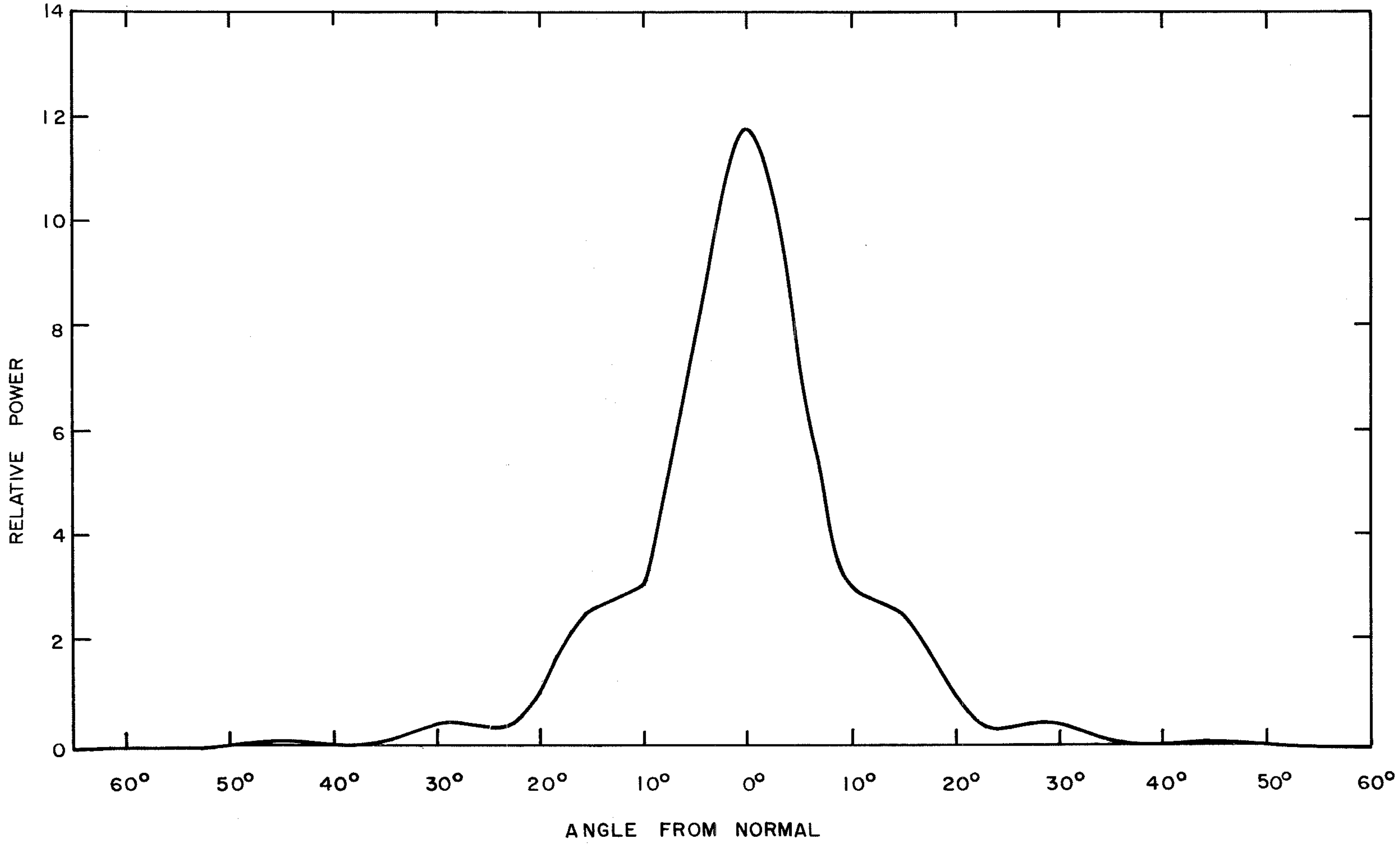

Fig. A-5.1. Radiation pattern at 250. m with c-w excitation

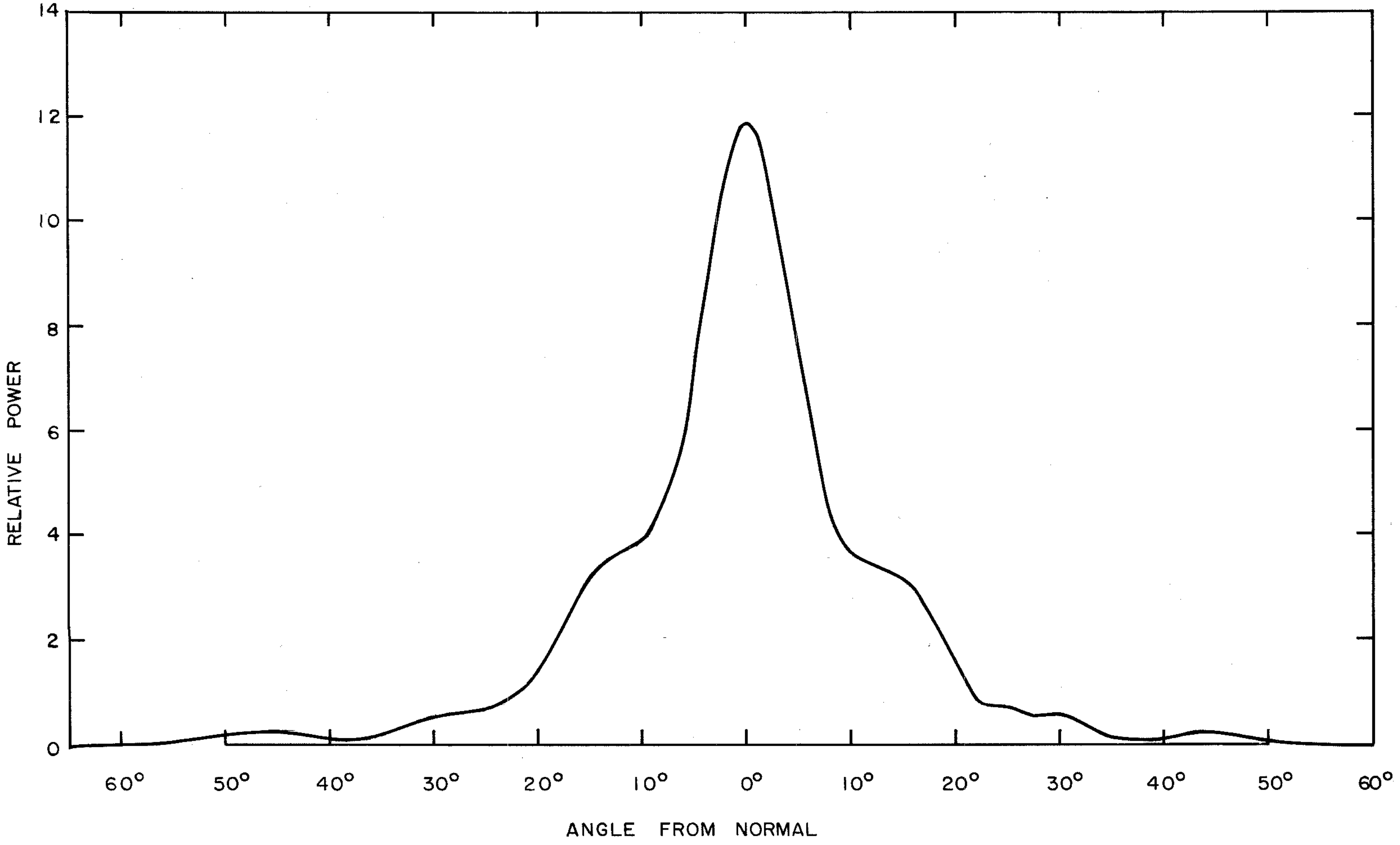

Fig. A-5.2. Indoor radiation pattern at 1.5 m using radiometer pattern recorder noise power from the discharge tube to the horn via a waveguide, spatial coherence of the aperture illumination is assured for each spectral component of the noise continuum, and hence for each component the radiation pattern is theoretically identical to that obtained using a c-w oscillator. This is, of course, in marked contrast to the pattern which is obtained from a rectangular aperture which is incoherently illuminated in the space-time domain. The patterns, Figs. A-5.1 and A-5.2, agree quite well considering that there are vast differences between the two methods of measurement. The maximum relative deviation is 4%, and the major deviation consists of a filling-in of the "indoor pattern" at the lower signal levels. This is reasonable physically, being due probably to multiple reflections from the walls of the room.

The receiver horn used in conjunction with the radiometer was also calibrated on the 250 m range. The dimensions of this horn are $L_a = 11.10$ cm, $L_b = 8.04$ cm, with a throat of 17.2 cm. For $\lambda = 3.26$ cm, the measured absolute gain is 72 and the computed gain is $G = \frac{\pi}{32}(31.7)(22.6) = 70$. The agreement between measured and computed values is quite satisfactory in this case, too. The effective solid angle for this horn at the 1.50 m range is given by

$$\Omega = \frac{G\lambda^2}{4\pi R^2}$$

$\approx 3^\circ$ across ○

$$\Omega = 2.70 \times 10^{-3} \text{ steradian} . \qquad \text{(A-5.1)}$$

From this pattern comparison experiment, it is concluded that a maximum relative error of approximately 4% can be introduced by multiple reflections from the walls of the room. This percentage is computed based on the peak value of the radiation.

APPENDIX VI - INPUT IMPEDANCE COMPUTATION

The parameter z_{in}, which appears in Eq. 4.26, is the input impedance of a linear antenna of length 2ℓ which is driven at the mid-point. Suitable approximate formulas for the computation of z_{in} are summarized in Eqs. A-6.1 to A-6.5 below (18). The input impedance z_{in}, is given by

$$z_{in} = z_o \frac{z \sin \beta\ell - iz_o \cos \beta\ell}{z_o \sin \beta\ell - iz_o \cos \beta\ell} \qquad \text{(A-6.1)}$$

in which the impedance factor z is given by

$$z = R + iX \qquad \text{(A-6.2)}$$

$$R = 30\,[2\,\text{Cin}\,2\beta\ell + (\text{Si}\,4\beta\ell - 2\,\text{Si}\,2\beta\ell)\sin 2\beta\ell + (2\,\text{Cin}\,2\beta\ell - \text{Cin}\,4\beta\ell)\cos 2\beta\ell] \qquad \text{(A-6.3)}$$

$$X = 30\,[2\,\text{Si}\,2\beta\ell + (2\,\text{Si}\,2\beta\ell - \text{Si}\,4\beta\ell)\cos 2\beta\ell + (2\,\text{Cin}\,2\beta\ell - \text{Cin}\,4\beta\ell - 2\,\text{Cin}\,\beta\ell + 2\ln 2)\sin 2\beta\ell] \qquad \text{(A-6.4)}$$

and the characteristic impedance, z_o, is given by

$$z_o = 120\,[\ln \frac{1}{\beta a} + 0.116 + \text{Ci}\,\beta\ell] \quad . \qquad \text{(A-6.5)}$$

Extensive compilations and graphs appear in the literature for z_{in} computed for the following range of variables: $0 < \beta\ell < 2\pi$ and $100 < \ell/a < 100{,}000$. However, these compilations are not useful here since the central interest is for relatively long antennas, i.e., $\beta\ell >> 1$. In this range, the above formulas are readily simplified for computation by the use of the asymptotic forms in Sec. 2 of Jahnke and Emde. For $\beta\ell >> 1$, Eqs. A-6.3 through A-6.5 can be reduced to the following formulas.

$$R = 30\left[\ln 4 + (0.577 + \ln \beta\ell)(2 + \cos 2\beta\ell) - \left(\frac{\pi}{2} + \frac{3}{4\beta\ell}\right)\sin 2\beta\ell\right] \qquad \text{(A-6.6)}$$

$$X = 30\left[\frac{\pi}{2}(2 + \cos 2\beta\ell) - (-0.810 + \ln \beta\ell)\sin 2\beta\ell\right.$$
$$\left. - \frac{1}{\beta\ell}\left(1 + \frac{3}{4}\cos 2\beta\ell - 2\sin \beta\ell \sin 2\beta\ell\right)\right] \qquad \text{(A-6.7)}$$

$$z_o = 120\left[\ln \frac{1}{\beta a} + 0.116 + \frac{\sin \beta\ell}{\beta\ell}\right] \quad . \qquad \text{(A-6.8)}$$

A numerical value is tabulated for the case $2\beta\ell = 9.5\pi$. It is interesting to compare these values of $|z_{in}|$ to those of $|z_r|$ where z_r, the simple reactive approximation to the input impedance is given by (18) as

$$z_r = -iz_o \cot \beta\ell \quad . \qquad \text{(A-6.9)}$$

Table A-6.1

INPUT IMPEDANCE FOR A RADIAN LENGTH OF 9.5π

$2\beta\ell$	R	X	λ/a	z_o	$\lvert z_{in}\rvert$	$\lvert z_r\rvert$
9.5π	287	146	10	76	93	76
			100	352	463	352
			1000	629	928	629

REFERENCES

(1) Nyquist, H., "Thermal Agitation of Electric Charge in Conductors", Phys. Rev. (1928), 32, 110-113.

(2) Johnson, J. B., "Thermal Agitation of Electricity in Conductors", Phys. Rev. (1928), 32, 97-109.

(3) Mumford, W. W., "A Broad-Band Microwave Noise Source", B.S.T.J.,(1949) 28, pp. 608-618.

(4) Parzen, P. and L. Goldstein, "Current Fluctuations in D.C. Gas Discharge Plasma", Jour. Appl. Phys. 79, 190, (1950).

(5) Dicke, R. H., "The Measurement of Thermal Radiation at Microwave Frequencies", Rev. Sci. Instr. 17, (1946), 268-275.

(6) Leontovich, M.A., and S. M. Rytov, Zhur. Exp. Teor. Fiz. 23, (1952), 246.

(7) Rytov, S. M., Theory of Electric Fluctuations and Thermal Radiation, Akad. Nauk Press, Moscow, (1953)

(8) Levin, M.L., and S. M. Rytov, "Thermal Radiation from a Thin Rectilinear Antenna", Jour. Tech. Phys. 25, (1955) No. 2, 323-332.

(9) Spiller, E., "Departure from the Cosine Law of Emission in the Case of Incandescent Tungsten", Zeits. f. Physik 72 (1931), pp. 215-217.

(10) Richtmyer, F. K., E. H. Kennard, and T. Lauritsen, Introduction to Modern Physics, Fifth Ed., McGraw-Hill Book Company, New York 1955, Ch. 4.

(11) Drude, P., The Theory of Optics, Longmans, Green and Co., New York 1901, Ch. IV part II, and Ch. I,II part III.

(12) Forsythe, W. E., Measurement of Radiant Energy, McGraw-Hill Book Co., New York 1937, p.11 and pp.20-21.

(13) König, W., Handbuch der Physik, XX, Springer, Berlin, 1928, 240-252.

(14) Ditchburn, R. W., Light, Interscience Publishers, Inc., New York 1953 Ch. XV.

(15) Dwight, H. B., Tables of Integrals, The Macmillan Co., 1947.

(16) Davenport, W. B., and W. L. Root, Random Signals and Noise, McGraw-Hill Book Co., New York, 1958, 45-75 and 87-111.

(17) Rytov, S. M., "Theory of Thermal Noise", Radiotekhnika 10, (1955), 3-13 in Nos. 2 and 3.

(18) Schelkunoff, S. A., and H. T. Friis, Antennas, Theory and Practice, John Wiley and Sons, Inc., 1952, 243, 267, 294-8, 301, 414-444, 601.

(19) Weber, J., "Scattering of Electromagnetic Waves by Wires and Plates", Proc. I.R.E. 43 (1955), 82-89.

(20) Pawsey, J. L. and R. N. Bracewell, Radio Astronomy, Oxford Univ. Press, London, 1955, 22.

(21) Easley, M. A., and W. W. Mumford, "Electron Temperature vs. Noise Temperature in Low Pressure Mercury-Argon Discharges", Jour. Appl. Phys. 22 (1951), 846-847.

(22) von Engel, A., Ionized Gases, Oxford Univ. Press, London, 1955, p.215.

(23) Smythe, W. R., Static and Dynamic Electricity, Second Ed., McGraw-Hill Book Co., New York, 1950.

(24) Kraus, J. D., Antennas, McGraw-Hill Book Co., New York, 1950, Ch. 13.

(25) Strum, P. D., "Considerations in High-Sensitivity Microwave Radiometry", Proc. I.R.E. 46 (1958), 43-53.

(26) Drake, F. D. and H. I. Ewen, "A Broad-Band Source Comparison Radiometer for Advanced Research in Radio Astronomy", Proc. I.R.E. 46 (1958), 53-60.

(27) Goldstein, S. J., "A Comparison of Two Radiometer Circuits", Proc. I.R.E. 43 (1955), 1663-1666.

(28) Bickmore, R. W., "Fraunhofer Pattern Measurement in the Fresnel Region", Canadian Jour. of Phys. 35 (1957), 1299-1308.

(29) Silver, S., Microwave Antenna Theory and Design , McGraw-Hill Book Co., New York 1949, 199, 574-578.

(30) Schelkunoff, S. A., Electromagnetic Waves, D. Van Nostrand Co., Inc., New York, (1943) 363,365.